

Assessment of exposure for LTE mobile terminals in a
heterogeneous usage

Vasco Manuel Simões de Oliveira

Thesis to obtain the degree of Master in
Electrical and Computer Engineering

Supervisor: Prof. Luís Manuel de Jesus Sousa Correia

Examination Committee

Chairperson: Prof. José Eduardo Charters Ribeiro da Cunha Sanguino

Supervisor: Prof. Luís Manuel de Jesus Sousa Correia

Member of Committee: Prof. Custódio José de Oliveira Peixeiro

February 2015

To Sílvia, my family and friends

Acknowledgements

After more than one year of constant work, the production of this thesis was only possible with the support of the people I love, and that were always by my side during all the hours that were spent developing this thesis.

First, I would like to thank to Professor Luís M. Correia for giving me the opportunity to write this thesis and for the constant knowledge and experience sharing that were of extreme importance throughout this work.

To all GROW members for the clarifications, in particular to Carla Oliveira and Michal Maćkowiak, who were essential to the development of my thesis with all their help and advices.

To all my friends, to whom I am very grateful for their friendship, understanding, and support, which kept me going in the hardest times.

In special, to my parents and my sister who always supported me with enormous patience, understanding and unconditional love, and to whom I owe everything that I am today, and all that I achieved. Their efforts and daily sacrifices for giving me the possibility to have a great education and to complete my academic degree were always present in my mind, as the thesis was being produced.

Last, but definitely not least, to Sílvia, the one I love, who was always by my side unconditionally, even on the long and tiring nights, supporting me and always helping me to achieve my goals. In order to her, I dedicate this work and all the effort put into it, which would have not been possible to accomplish without her presence, tenderness and love.

Abstract

The main purpose of this thesis was to study and analyse radiation exposure to an LTE signal from a mobile terminal, amidst other cellular and wireless technologies. This purpose was achieved by designing and modelling the antenna used on the prototype known as *Google Glass*, the mobile device chosen for the case study, and implementing this model on the *CST MWS* software, an EMF simulator. A complete voxel model and a 3D *Glass* model were provided for this work. These models were initially assessed separately, with the final evaluation consisting of all elements put together. The main analysis were made on electric field's strength, interference and penetration, as well as maximum SAR for 1 W of power, and the limit of feeding power, in accordance with the regulations imposed on SAR values. Also, an analysis was made on the dimensions of the antenna in use. Results show this device can indeed carry cellular capabilities, and not only the current Wi-Fi and Bluetooth modules, although it needs to be calibrated to use a limit of 106.3 mW in the 1.8 GHz band and 97.1 mW in the 2.6 GHz one. This could limit the use of the prototype, with the desired connection quality, to only urban areas, with high coverage capacity and increased number of pico-cells, in order to minimise distance to the BS.

Keywords

Radiation Exposure, LTE, SAR, CST, Google Glass, Voxel.

Resumo

O principal objetivo desta tese foi estudar e analisar a exposição à radiação causado por um sinal LTE a partir de um terminal móvel, entre outras tecnologias celulares e sem fios. Este objectivo foi alcançado através da concepção e modelo da antena utilizada no protótipo conhecido como *Google Glass*, o dispositivo móvel escolhido para o caso de estudo, implementando este modelo no software *CST MWS*, um simulador de campos electromagnéticos. Para este trabalho foram também fornecidos um modelo voxel completo e um modelo 3D do *Glass*. Os modelos foram inicialmente avaliados separadamente, enquanto que a avaliação final foi realizada com todos os elementos juntos. As principais análises feitas foram relativas à intensidade, interferência e penetração do campo elétrico, bem como o máximo de SAR para 1 W de potência, e o limite da potência de alimentação, isto de acordo com as normas impostas aos valores de SAR. Além disso, foi feita uma análise às dimensões da antena em uso. Os resultados mostram que este dispositivo pode de facto utilizar capacidades celulares, e não apenas os módulos Wi-Fi e Bluetooth actuais, embora precise de ser calibrado para um limite de 106,3 mW na banda de 1,8 GHz e 97,1 mW na banda de 2,6 GHz. Isto poderia limitar a utilização do protótipo, devido à qualidade da ligação desejada, apenas para as áreas urbanas com elevada capacidade de cobertura e elevado número de pico-células, a fim de minimizar a distância para a BS.

Palavras-chave

Exposição a radiação, LTE, SAR, CST, Google Glass, Voxel.

Table of Contents

Acknowledgements	iii
Abstract.....	v
Resumo	vi
Table of Contents.....	vii
List of Figures	ix
List of Tables.....	xi
List of Acronyms	xii
List of Symbols.....	xiv
List of Software	xvi
1 Introduction	1
1.1 Overview and Motivation	2
1.2 Structure.....	5
2 Fundamental Concepts	7
2.1 Radio Interface	8
2.1.1 GSM.....	8
2.1.2 UMTS.....	9
2.1.3 LTE	11
2.2 Human body characterisation and modelling.....	14
2.2.1 Dielectric properties	14
2.2.2 Modelling	15
2.3 Electromagnetic Radiation Exposure.....	17
2.4 Field regions	20
2.5 State of the Art.....	22
3 Modeling and Simulation	25
3.1 CST Simulator	26

3.2	Terminals and Antennas.....	29
3.3	Modelling of Antenna	32
3.4	Modelling of <i>Glass</i>	36
3.5	Modelling of Voxel Head.....	40
3.6	Mesh Cell and Simulation Load	43
4	Result Analysis.....	46
4.1	Scenario description	47
4.2	Radiation Pattern and Electric Field	48
4.3	SAR evaluation.....	51
4.4	Power evaluation	54
4.5	Antenna Length	56
5	Conclusions.....	62
Annex A.	LTE Frequency Bands	68
Annex B.	Dielectric Properties of Main Body Tissues	72
Annex C.	Materials Used in Simulations.....	75
Annex D.	Additional information on modelling	79
Annex E.	Additional results	82

List of Figures

Figure 2.1 - Comparison between the transmission in OFDMA and SC-FDMA (adapted from [Agil09]).	12
Figure 2.2 - LTE DL physical resource based on OFDMA (extracted from [Eric11]).	13
Figure 2.3 - High-resolution whole-body Japanese human voxel model (extracted from [Ito07]).	16
Figure 2.4 - Field regions of an antenna (extracted from [Ba05]).	20
Figure 2.5 - Typical changes of antenna amplitude pattern from the reactive near field to far field (extracted from [RWY95]).	22
Figure 3.1 - FIT spatial discretisation scheme (adapted from [CST14]).	27
Figure 3.2 - Representation of the discretisation of Maxwell's integral equations (extracted from [CST14]).	28
Figure 3.3 - Leap Frog scheme of CST Transient Solver (extracted from [CST14]).	30
Figure 3.4 - Geometric approach for determination of E or H on point P (Extracted from [ChCa01]).	31
Figure 3.5 - <i>Google Glass</i> antenna, with reference ruler in inches (extracted from [FCC14]).	33
Figure 3.6 - Antenna model created on <i>CST MWS</i> .	35
Figure 3.7 - S_{11} parameter for the antenna in vacuum.	35
Figure 3.8 - Electric field over the distance of the antenna in vacuum.	36
Figure 3.9 - Front cut plane of antenna's radiation pattern in vacuum, for different frequency bands.	36
Figure 3.10 - Lateral cut plane of antenna's radiation pattern in vacuum, for different frequency bands.	37
Figure 3.11 - Original <i>Glass</i> before being moulded to fit the voxel model, with reference ruler in inches (extracted from [FCC14a]).	38
Figure 3.12 - Top view of <i>Glass</i> model used in <i>CST</i> .	38
Figure 3.13 - Front view of <i>Glass</i> model used in <i>CST</i> .	38
Figure 3.14 - Schematic for side and bottom view of the <i>Glass</i> , with the antenna's location and dimensions (extracted from FCC14a).	39
Figure 3.15 - Side view of <i>Glass</i> prototype showing the location of the antenna, with reference ruler in inches (extracted from [FCC14b]).	39
Figure 3.16 - Cut plane of side view of <i>Glass</i> , showing the location of the antenna on <i>CST</i> .	39
Figure 3.17 - Electric field over the distance of the antenna equipped within the <i>Glass</i> .	40
Figure 3.18 - Different perspectives of the <i>Glass</i> with axis and coordinates represented.	40
Figure 3.19 - Top cut plane of radiation pattern from antenna inside the <i>Glass</i> model.	41
Figure 3.20 - Front cut plane of radiation pattern from antenna inside the <i>Glass</i> model.	41
Figure 3.21 - Different perspectives of the Voxel model used in simulations.	42
Figure 3.22 - In order, top, side and front perspectives of the voxel model used in <i>CST</i> .	42
Figure 3.23 - Front cut plane of the radiation pattern from incident plane wave on the voxel model.	43
Figure 3.24 - Top cut plane of the radiation pattern from incident plane wave on the voxel model.	44
Figure 3.25 - Top, side and front perspectives of the model with its coordinates' axis.	43
Figure 3.26 - Perspective with probes (red dots) and side view of the antenna with mesh cell	

visible.	45
Figure 3.27 – Top and side view of the voxel model with respective mesh cell visible.....	45
Figure 4.1 - Voxel model, together with the model of <i>Glass</i> and the antenna.	48
Figure 4.2 - Cut planes used for the simulations, with port visible as a red arrow.	48
Figure 4.3 – Evolution of electric field over distance towards the centre of the head, amplified for further distances.	50
Figure 4.4 – Top cut plane of the radiated pattern while in the <i>Glass</i> and on the voxel	51
Figure 4.5 – Front cut plane of the radiated pattern while in the <i>Glass</i> and on the voxel.....	51
Figure 4.6 – 3D side view of the SAR range and amplitude on the voxel model.	53
Figure 4.7 – 2D front cut plane view of the SAR range and amplitude on the voxel model.....	53
Figure 4.8 - 2D top cut plane view of the SAR range and amplitude on the voxel model.....	54
Figure 4.9 – 3D side view of the SAR range and amplitude on the voxel model.	55
Figure 4.10 – 2D front cut plane view of the SAR range and amplitude on the voxel model.....	56
Figure 4.11 - 2D top cut plane view of the SAR range and amplitude on the voxel model.....	56
Figure 4.12 – Reflection coefficient for 1.8 GHz and 2.6 GHz designed antennas in vacuum. ...	58
Figure 4.13 – Top cut plane on radiation pattern of 1.8 GHz designed antenna.	59
Figure 4.14 – Top cut plane on radiation pattern of 2.6 GHz designed antenna.	59
Figure 4.15 – Front cut plane on radiation pattern of 1.8 GHz designed antenna.	60
Figure 4.16 – Front cut plane on radiation pattern of 2.6 GHz designed antenna.	60
Figure 4.17 – 3D side view of the SAR range and amplitude on the voxel model for 1.8 GHz antenna.	61
Figure 4.18 – 3D side view of the SAR range and amplitude on the voxel model for 2.6 GHz antenna	61
Figure A.1 – Conductivity of the most important body tissues (extracted from [Lo10]).....	71
Figure A.2 – Relative permittivity of the most important body tissues (extracted from [Lo10])... 71	
Figure A.3 – Penetration depths of the most important body tissues (extracted from [Lo10])....	72
Figure A.4 – 3D perspective of antenna in vacuum.....	78
Figure A.5 – Side view of 3D perspective of antenna in vacuum, with main lobes visible.....	78
Figure A.6 – 3D perspectives of antenna in <i>Glass</i> for each frequency band, with scale in linear units.....	78
Figure A.7 – Top view of 3D perspective of radiation pattern from original antenna.....	81
Figure A.8 – Front view of 3D perspective of radiation pattern from original antenna.....	81
Figure A.9 – Evolution of E-field over distance of antenna designed for 1.8 GHz, amplified for greater distances.....	82
Figure A.10 – Evolution of E-field over distance of antenna designed for 2.6 GHz, amplified for greater distances.....	83
Figure A.11 – Top cut plane for maximum SAR reading on antenna designed for 1.8 GHz	84
Figure A.12 – Front cut plane for maximum SAR reading on antenna designed for 1.8 GHz... 84	
Figure A.13 – Top cut plane for maximum allowed power on antenna designed for 1.8 GHz... 85	
Figure A.14 – Front cut plane for maximum allowed power on antenna designed for 1.8 GHz. 85	
Figure A.15 – Top cut plane for maximum SAR reading on antenna designed for 2.6 GHz.....	86
Figure A.16 – Front cut plane for maximum SAR reading on antenna designed for 2.6 GHz....	86
Figure A.17 – Top cut plane for maximum allowed power on antenna designed for 2.6.....	87
Figure A.18 – Front cut plane for maximum allowed power on antenna designed for 2.6.....	87

List of Tables

Table 2.1 - MT's power level according to power level number sent by the BS (extracted from [RE14]).	9
Table 2.2 - Electrical properties of the body tissues at the different frequency bands [ITIS14].	15
Table 2.3 - Reference and alternate methodologies established by the EN 50383 standard (extracted from [CENE13]).	18
Table 2.4 - Reference values for general public exposure [ICNI09]	20
Table 3.1 - Dimensions of the elements composing the model of the antenna in <i>CST</i> .	34
Table 3.2 - Boundary between near field and far field for modeled antenna, at different frequencies.	34
Table 3.3 - Dimensions of the voxel model in <i>CST</i> .	43
Table 4.1 - The different technologies and their main frequencies bands for the desired scenario.	49
Table 4.2 - SAR results from <i>CST</i> , simulating <i>Glass</i> 's evaluation by the FCC.	52
Table 4.3 - Peak SAR readings on the voxel model at different frequencies for 1 W of power.	54
Table 4.4 - Maximum power permitted at different frequencies to achieve the limit of 2 W/Kg.	55
Table 4.5 - Comparison of different antenna's lengths among different frequencies, between theoretical and real/simulated values.	57
Table 4.6 - Peak SAR readings on the voxel model at different frequencies for 1 W of power.	58
Table 4.7 - Maximum power permitted at different frequencies to achieve the limit of 2 W/Kg.	58
Table A.1 - E-UTRA frequency bands [3GPP13b] and [HoTo11].	67
Table A.2 - FDD Frequency bands' usage by world's region (adapted from [HoTo11]).	68
Table A.3 - Results from ANACOM auction for frequency bands (adapted from [ANAC14]).	69
Table A.4 - Physical properties of the used materials.	74
Table A.5 - Linear values correspondent to amplitudes of main lobes, on radiation pattern charts from Chapter 3.	79
Table A.6 - Linear values correspondent to amplitudes of main lobes, on radiation pattern charts from Chapter 4.	88
Table A.7 - RF output power measurement in dBm of <i>Glass</i> 's SAR report (extracted from [FCC14c]).	88

List of Acronyms

1G	First-Generation mobile systems
2G	Second-generation mobile systems
3G	Third-generation mobile systems
3GPP	Third-generation Partnership Project
4G	Fourth-generation mobile systems
ACI	Adjacent Channel Interference
ACLR	Adjacent Channel Leakage Power Ratio
A-MPR	Additional Maximum Power Reduction
ANACOM	Autoridade Nacional de Comunicações
ARFCN	Absolute Radio Frequency Channel Numbers
BLER	Block Error Ratio
BS	Base Station
CNS	Central Nervous System
CP	Cyclic Prefix
CT	Computer Tomography
DL	Downlink
DNA	Deoxyribonucleic Acid
DS-CDMA	Direct-Sequence Code Division Multiple Access
EM	Electromagnetic
EMF	Electromagnetic field
E-UTRA	Evolved UMTS Radio Access
ETSI	European Telecommunications Standards Institute
FCC	Federal Communications Commission
FDD	Frequency Division Duplex
FDMA	Frequency Division Multiple Access
FIT	Finite Integration Technique
GPRS	General Packet Radio Service
GSM	Global System for Mobile Communications
IARC	International Agency for Research on Cancer
ICNIRP	International Commission on Non-Ionising Radiation Protection
ILPC	Inner Loop Power Control
ISI	Inter-Symbol Interference
LTE	Long Term Evolution
LW	Lines per Wavelength

MIMO	Multiple Input Multiple Output
MLRL	Mesh Line Ratio Limit
MOP	Maximum Output Power
MPR	Maximum Power Reduction
MRI	Magnetic Resonance Imaging
MT	Mobile Terminal
OFDMA	Orthogonal Frequency Division Multiple Access
OpLPC	Open Loop Power Control
OuLPC	Outer Loop Power Control
OVSF	Orthogonal Variable Spreading Factor
PC	Power Control
QoS	Quality of Service
RB	Resource Blocks
RFR	Radio Frequency Radiation
RNC	Radio Network Controller
RRC	Radio Resource Control
SAR	Specific Absorption Rate
SC	Scrambling Code
SC-FDMA	Single Access Frequency Division Multiple Access
SDCCH	Standalone Dedicated Control Channels
SF	Spread Factor
SIR	Signal-to-Interference Ratio
SIR_{est}	Estimated Signal-to-Interference Ratio
SIR_{Target}	Target Signal-to-Interference Ratio
SMS	Short Message Service
SNR	Signal-to-Noise Ratio
TCH	Traffic Channels
TDD	Time Division Duplex
TDMA	Time Division Multiple Access
TPC	Transmit Power Control
UE	User Equipment
UL	Uplink
UMTS	Universal Mobile Telecommunications Systems
WCDMA	Wideband Code Division Multiple Access
WHO	World Health Organisation

List of Symbols

$\langle \vec{S} \rangle$	Average radiated power
\emptyset	Angle of rotation between two antennas
B	Electrical length per meter of wavelength
γ	Propagation constant in the medium
ε	Permittivity
ε_0	Permittivity in free space
θ	Angle between zenith's axis of antenna and point of observation
λ	Wavelength
ρ	Volume density
σ	Electrical conductivity
σ_0	Electrical conductivity in free space
σ_l	Ionic conductivity
ω	Angular frequency
δ	Polarisation loss factor
τ	Mean relaxation time
A	Surface vector bounded by the closed contour ∂A ;
b	Magnetic facet flux
B	Magnetic field induction vector
C	Discrete curl operator
C'	Dual discrete curl operator
d	Dielectric facet flux
D	Maximum antenna size (while calculating each region's range)
D_i	Electric displacement vector
e	Electric grid voltage
E	Electric field intensity
E_i	Electric field at frequency i
$E_{ref,i}$	Electrical field reference at frequency i
h	Magnetic grid voltage
H	Magnetic field intensity
H_{ei}	Height of voxel model
H_j	Magnetic field at frequency j
$H_{ref,j}$	Magnetic field reference at frequency j
I	Wire current in amps

I_0	Maximum possible current
J	Current density vector
J_s	Surface current density
j_s	Surface current density flux matrix
L	Length of voxel model
M	Mass
M_μ	Permeability matrix
M_ϵ	Permittivity matrix
$M_{\pi c}$	Conductivity matrix
P_{rad}	Total radiated power
R	Distance to antenna
R_1	Range of reactive near-field
R_2	Range of radiating near-field
S	Directional energy flux density
SAR	Specific Absorption Rate
s	Infinitesimal vector element of the closed contour ∂A
S_d	Discrete divergence operator
S'_d	Dual discrete divergence operator
t	Time
W	Width of voxel model
Z'	Intrusive impedance of the medium

List of Software

Microsoft PowerPoint 2010 ©	Graphical presentation editor
Microsoft Excel 2010 ©	Calculation and graphical chart editor
Microsoft Word 2010 ©	Text editor
SolidWorks 3D CAD ©	3D model designer and editor
CST MICROWAVE STUDIO ©	3D EM simulator for high frequencies

Chapter 1

Introduction

This chapter gives a brief overview of the work. Before establishing work targets and original contributions, the scope is brought up in Section 1.1, then, the structure of the work is described in Section 1.2.

1.1 Overview and Motivation

The need for communication, to be connected and for mobility has always been inherent to our modern society. From the combination of these factors, solutions started to arise for wireless systems in order to build bidirectional communications and also to access information anytime and anywhere. Although industry was conscious about this reality, mobile communication networks only experienced a large increase on the number of users after the introduction of second-generation (2G) systems. The fast development of this sector was accomplished by the constant evolution of products and standards, always with close attention to the emerging trends and the growing needs of the customers. The unpopularity of the first generation (1G) systems was mainly due to its high price of Mobile Terminals (MT), the lack of true mobility and also the use of different technologies in different countries. Nowadays, the cellular technology is an indispensable tool to the business world for the fast and global communications, for the general public as an interface for personal/social interaction with other users, and also as an access point for entertainment contents.

The implementation of 2G systems allowed the revolution from analogue to digital transmission, providing the necessary spectral efficiency according to the expectations of operators. The European Telecommunications Standards Institute (ETSI) was responsible for developing the 2G cellular standard, which was adopted around the world as Global System for Mobile communications (GSM) [Moli11]. The publication and presentation of this technology occurred in the early 90s, and was initially planned to provide voice communications and other services of low rate at 14.4 kbps, such as the popular Short Message Service (SMS) [HoTo11]. The development of GSM extension, acknowledged as 2.5G, was concluded in 1995, unveiling the introduction of General Packet Radio Service (GPRS) and the more efficient modulation of Enhanced Data rates for GSM Evolution (EDGE). Although the introduction of these upgrades managed to increase the packet data transfer rates at the time, data-handling capabilities were still very limited [Moli11].

Under the light of the upgrades achieved in GSM, and the need to provide even greater bit-rates for many services, third generation (3G) mobile systems were designed with this objective in mind, enabling high-quality images and video to be transmitted and received, and also providing access to the Web with higher data rates, following the growing popularity of the Internet at the time [Hoto07]. One of the 3G systems, and the most used one, is the Universal Mobile Telecommunication System (UMTS) presented by the 3rd Generation Partnership Project (3GPP) in 1999, at the time using its first version known as Release 99. Despite a theoretical and announced bit rate up to 2 Mbps, initially UMTS was only able to provide a data rate up to 384 kbps for the Downlink (DL) and Uplink (UL). In 2002, the 3GPP launched Release 5, an important upgrade able to overcome Release 99, introducing the High Speed Downlink Packet Access (HSDPA). This release was deployed on top of already existing networks, thus minimising hardware and equipment upgrade, managing to reach a peak data rate of 14.4 Mbps. For UL packet-data improvements, Release 6 was announced, also known as High Speed Uplink Packet Access (HSUPA), with data rates up to 5.7 Mbps [HoTo06]. The combination of HSDPA and HSUPA technologies are referred to as High-Speed Packet Access (HSPA), with attractive features for Voice

over IP (VoIP) and other packet-based applications that require low latency, where its main bottleneck resides in the maximum simultaneous user capacity the operators need to provide.

Fast forwarding to 2004, 3GPP started to develop the fourth generation (4G) system, called Long Term Evolution (LTE), in parallel with solutions for HSPA evolution (Release 7 and 8), since it was predicted that the spectral efficiencies and data rates of 3G technology would not meet the demand of future applications. Indeed, mobile data traffic has increased exponentially in the last years, and is even expected to increase 30 times between 2011 and 2016 [Vile12]. LTE specifications suggest an overall change in both the core network and the radio interface, supporting new features in order to increase the network's performance and capability, such as Multiple Input Multiple Output (MIMO) antenna technology. This new standard provides peak data rates of 100 Mbps in DL and 50 Mbps in UL with a 20 MHz spectrum allocation for each of DL and UL. Release 10 admits theoretical data rates up to 1 Gbps, known as LTE-Advanced [Moli11].

Even though this evolution and development of technology is mainly oriented at the general public's needs and the public market's desires, and even though the use of these mobile devices continues to rise (both in number of users and in time spent per user), this same public is the one who more and more raises concerns about the potential health risks caused by radiation from mobile communication systems. This growth is also accompanied by the increase of terminals and Base Stations (BS) antennas, which are installed in increasingly smaller cells, and thus closer to the general public eyesight, alerting people to their existence.

Although all technologies have inherent protocols and algorithms for power control (both for BSs and MTs), which have as main objective keeping power at the minimum needed to deliver the desired quality of service, not always the ideal conditions are met, which can lead to a large increase in the output power of the MTs' antenna, raising the exposure to radiation for nearby individuals and entities. This happens especially in rural areas or zones where the concentration of BS is sparser. Although these algorithms have improved along with the upgrade of the technologies in use, and despite the latest releases have less output power usage for the antenna than the early ones, in these zones the MT has to increase (sometimes in great magnitude) the output power, since the distance to the BS becomes wider than in urban zones, where the MT does not need to struggle to have the desired connection's quality. The peak output power a modern mobile phone can generate is 1 W for GSM [FOPH14], 250 mW for UMTS [3GPP11] and 200 mW for LTE [3GPP09], although the output power rarely reaches the peak of a given technology. For example, a mobile device using LTE, while idle, will only transmit at 0.1 mW.

The concern and investigation of the impact of electromagnetic (EM) radiation on living tissues started long before the appearance of modern mobile communications systems, with the military radar systems in World War II and the emergence of the first high-voltage lines. The study regarding different areas, such as physics, biology, medicine and engineering, have always been and still are crucial to establish the limits of the electromagnetic field (EMF) strength, at which may cause adverse effects to health. Several international organisations and entities were responsible for the advances in this area, working on recommendations for radiation exposure limits from the quantification of the thermal effects [OICa02].

However this topic continues to generate a great deal of controversy regarding the non-thermal effects of EM radiation. Over the past years, studies with contradictory results were published, where many deficiencies were found in these works, as regards the number of insufficient samples, results that are not replicated in real environments or even the period the tissue was exposed to the radiation in study [ICNI98], [COST00], [WHO02], [ICNI11]. Regarding the current regulatory entities that control the directives over the radiation exposure, the International Commission on Non-Ionising Radiation Protection (ICNIRP) has jurisdiction over Europe, while in the United States of America it is the Federal Communications Commission (FCC) the organisation who legislates this topic. As for the maximum SAR (Specific Absorption Rate) value associated to a certain device, ICNIRP has defined 2.00 W/Kg over 10 g of tissue [ICNI09] while the FCC has defined 1.60 W/Kg over 1 g of tissue [FCC13].

However, even with the increasing concern over radiation exposure, and the increment of devices in use, there are currently only a handful of European countries that take measures to protect their citizens, by informing them and enforcing mandatory warning labels on the packaging of mobile apparatuses. In France, for example, it is forbidden for children under 15 years of age to use GSM and the European Council has also passed the resolution wherein they advise a complete restriction of mobile phones and wireless internet in schools [Hu11].

In 2012, *Google* unveiled a new project called *Glass*, bringing to the world a new type of smart device. The prototype, like its name announces clearly, consists on a pair of augmented reality glasses composed by two types of incorporated wireless technologies: Wi-Fi 802.11b/g at [2412, 2462] MHz and Bluetooth low energy at [2402, 2480] MHz [FCC13]. And even though no cellular technology is present, it still emits non-ionising radiation thanks to these wireless components. *Google* never released an official statement on why the cellular module was never implemented on the prototype.

Although the majority of the studies on this topic evaluate and analyse typical mobile phones or even smart phones, *Glass* represents a fundamentally new type of wireless device. Unlike mobile phones, which are used next to the head only when making phone calls, *Google Glass* is designed to be worn on the user's head in the same position for longer periods, even for an entire day. The novel way in which *Google Glass* is used brings two unique risk concerns with regard to its radiation exposure. First, as stated before, cumulative exposure over time plays a very important role in evaluating the health risks of wireless radiation, and secondly, the position and location of the antenna over the entire usage time never changes, meaning the radiated zone is constantly the same, increasing the risk of damage to the tissue and brain in the vicinity of the antenna.

This work has the objective to analyse if cellular technologies (especially LTE) can be implemented into this new device, although potentially harmful due to the nature of its usage method, and if so, if it can be feasible due to the output power, SAR limit and interference from the *Glass* module and interference from the user and its influence on the radiated wave. In order to achieve the desired results, the chosen simulating software is *CST Microwave Studio*. By putting together the model of the antenna designed and both the *Glass* and voxel model acquired, it is possible to get a full analysis of the interaction of all components together.

1.2 Structure

The thesis is structured into 5 main chapters, followed by a series of annexes. The present one gives the overview and the starting point that motivates the investigation on high frequency radiation exposure.

In Chapter 2, the systems' backgrounds are presented. GSM, UMTS and LTE architectures, respective radio interfaces, power control and transmitting power aspects are addressed, with special emphasis on the last two. Multiple access techniques of these systems are also analysed, in order to understand how they work, thus making the simulations as realistic as possible. This chapter also includes a brief overview on radiation exposure, description of the models usually used for this type of simulations, the different field regions and finally the state of the art, which covers the main work and analysis of exposure to radiation to date.

Chapter 3 presents the models proposed to evaluate the performance and radiation exposure of the systems described. The software used for the simulations is initially depicted, explaining how it works, the algorithms used and the entire process needed to get the results desired. Next, the model of the antenna created within the simulator, along with the voxel and *Glass* model used in order to assess the main topic of the work are also described and explained to detail, from the dimensions of each component, to their physical properties.

In Chapter 4, the scenarios in which the simulations were performed is described, followed by the main results that were obtained for the different frequency bands of each technology in analysis. Results for the different exposure on each frequency, along with their configurations and presented separately for all systems.

This work closes with Chapter 5, where the main conclusions of the work are drawn, and suggestions for future researches are pointed out.

Finally, a set of annexes concludes the present document with supplementary information, when there is a need for the global comprehension of the described problem.

Chapter 2

Fundamental Concepts

This chapter provides an overview of the main ideas applied in this thesis. In Section 2.1, the GSM, UMTS and LTE architectures are presented, focussing on the aspects of radio interface. Section 2.2 covers the aspects of human body characterisation and modelling, followed by 2.3 in which electromagnetic exposure is analysed. Finally, in section 2.4, the state of the art concerning the scope of the work is presented.

2.1 Radio Interface

2.1.1 GSM

Global Systems for Mobile Communications (GSM) uses Frequency Division Duplex (FDD) as a channel separation method, the assigned bands being [890, 915] MHz for UL and [935, 960] MHz for DL for GSM-900, and for GSM-1800, the ranges are [1710, 1785] MHz for UL and [1805, 1880] MHz for DL [Moli11].

GSM also employs a combination of Frequency Division Multiple Access (FDMA) with Time Division Multiple Access (TDMA), in which the frequency bands are divided into carriers spaced by 200 kHz each, being numbered consecutively by the ARFCNs (Absolute Radio Frequency Channel Numbers). Each carrier has 8 timeslots, and therefore it allows up to 8 users to share it. One timeslot has a duration of 576.92 μ s, meaning it has the equivalent of 156.25 bits. The group of the 8 timeslots, the frame, has a duration of 4.615 ms [Moli11].

GSM radio interface channels are divided and classified as radio, physical and logical (transporting a specific kind of system information), being traffic channels (TCH) and Standalone Dedicated Control Channels (SDCCH) part of the last group. The TCH carries all the voice and data between the BS and the MTs. In order to increase the capacity of a cell, these can be converted between full-rate and half-rate traffic channels, where two users can share the same timeslot, using it alternately. Regarding GPRS, different coding schemes are used, leading to different transmission rates. In theory, a maximum data rate of 171.2 kbps can be achieved while aggregating all of the 8 timeslots.

Concerning maximum output power of the BS Transmitter, the GSM standard defines 8 classes. This value is measured at the input of the BS Subsystem Transmission combiner. Depending on the type of cell, power ranges are: [34, 58] dBm for macro-cell, [9, 32] dBm for micro-cell and [13, 23] dBm for pico-cell [Corr13]. The typical value for an MT's maximum output power is in [22, 39] dBm [Corr13]. Though these are the maximum values for each device in GSM, a lower value is usually used. This happens due to the fact that GSM performs a power control in both the BS and the MT, so that the power used is only the necessary for a desired quality during the transmission.

As seen in [3GPP14], power control (PC) refers to the strategies or techniques required to adjust the transmitted power in order to regulate the transmitted power to achieve a desired signal strength. There are various aspects and variables that are taken into account regarding PC in GSM, but the main ones are: the distance between MT and BS (an MT far away from a BS requires a stronger transmitted signal than one closer) and the desired QoS (if the speech quality is better than necessary for one MT, the signal strength for that specific MT is decreased). The decrease of power implies that the system is improved, since there is a reduction in interference, the user will experience a decrease in battery consumption when transmitting to the BS and finally the value of emitted radiation will also be lower. Power control is used both in UL and DL, and the principle is equal for both. So, in short, the BS controls the power output of the MT, keeping the GSM power level sufficient to maintain a good signal to noise ratio, while not too high to reduce interference, overloading, and also to preserve the battery life. A table

of GSM power levels is defined (represented in Table 2.1), and the BS controls the power of the MT by sending a GSM "power level" number; the MT then adjusts its power accordingly. In virtually all cases, the increment (or decrease) between the different power level numbers is done in 2 dB steps. The accuracy required for GSM power control is relatively stringent. At the maximum power levels it is typically required to be controlled within a 2 dB margin, whereas this relaxes to 5 dB at the lower levels.

Table 2.1 - MT's power level according to power level number sent by the BS (extracted from [RE14]).

Power level number	GSM-900 peak output power [dBm]	GSM-1800 peak output power [dBm]
0	39	30
1	39	28
2	39	26
3	37	24
4	35	22
5	33	20
6	31	18
7	29	16
8	27	14
9	25	12
10	23	10
11	21	8
12	19	6
13	17	4
14	15	2
15	13	0
16	11	0
17	9	0
18	7	0
19-28	5	0
29	5	36
30	5	34
31	5	32

2.1.2 UMTS

Universal Mobile Telecommunications Systems (UMTS) uses Wideband Code Division Multiple Access (WCDMA) as its main air interface technology, which is a wideband Direct-Sequence Code Division Multiple Access (DS-SS) system that spreads the spectrum of the transmitted signal of user data by a chips sequence derived from CDMA spreading codes. These codes are orthogonal to each other to

reduce interference among users, though the trade-off is the decrease of quality with the increase of users. This happens due to the limited orthogonal code numbers that can be implemented and also due to the influence of signal propagation and interference between users.

UMTS currently only operates in FDD. It has a chip rate of 3.84 Mcps, which leads to a channel bandwidth of 4.4 MHz, where the carrier spacing can be selected on a 200 kHz grid between approximately 4.4 and 5 MHz. The band currently occupied is [1920, 1980] MHz for UL and [2110, 2170] MHz for DL [Hoto11]. UMTS has typical values for the MT nominal maximum output power ranging in [21, 33] dBm [Corr13].

Regarding spreading and multiple access, WCDMA uses channelisation and scrambling respectively. Channelisation uses Orthogonal Variable Spreading Factor (OVSF) to extend the transmission bandwidth and therefore changing the Spread Factor (SF), maintaining the orthogonality in between codes. Scrambling is applied on top of spreading, being mainly used to differentiate the transmitted signals, i.e., in DL it distinguishes the sectors of the cell, and in UL it separates MTs from each other. The Scrambling Code (SC) can be categorised as short (based on the extended S(2) family) or long (10 ms code based on Gold family). Although long codes are used both by UL and DL, only UL uses short codes.

Concerning power control, this aspects varies from one release to another. According to [GuGu03] and [Bern], UMTS (unlike GSM) has a greater need to combat the near-far problem. A User Equipment (UE) close to the Node-B transmitting at the same power as another at the cell edge, will potentially block out the latter. In order to maintain reliable links to all UEs, the received power at the Node-B should be about the same. This means that propagation path loss between the UE and the Node-B should be taken into account. In an ideal environment, this alone would be sufficient, but real environments are not ideal. Channel conditions vary, in the short and long terms. Recognising all these, one can relate easily to the three main power control mechanism in UMTS: Open Loop Power Control (OpLPC), Inner Loop Power Control (ILPC) and Outer Loop Power Control (OuLPC).

OpLPC is the ability of the UE transmitter to set its output power to a specific value and relates directly to the path loss. It is used for setting initial UL and DL transmission powers when a UE is accessing the network and, as the name suggests, this control has no feedback. The open loop power control tolerance is ± 9 dB (normal conditions) or ± 12 dB (extreme conditions).

ILPC in the UL is the ability of the UE transmitter to adjust its output power in accordance with one or more Transmit Power Control (TPC) commands received in the DL, in order to keep the received UL Signal-to-Interference Ratio (SIR) at a given SIR target (SIR_{target}). The UE transmitter is capable of changing the output power with a step size of 1, 2 and 3 dB, in the slot immediately after the TPC command can be derived. The serving cells estimate the SIR (SIR_{est}) of the received UL, generate the TPC commands and transmit the commands once per slot according to the following rule: if $SIR_{est} > SIR_{target}$ then the TPC command to transmit is "0", while if $SIR_{est} < SIR_{target}$ then the TPC command to transmit is "1". Upon reception of one or more TPC commands in a slot, the UE derives a single TPC command for each slot, combining multiple TPC commands if more than one is received in a slot. It happens at a rate of 1500 Hz to combat fast fading. This control is within the UE and the Node-

B. While outer loop control is set at Radio Resource Control (RRC) level and executed at Layer 1, fast power control happens at Layer 1 in order to meet the BLER target set by outer loop control. The effect of this control is that even in a fading channel, the received power is maintained constant so as to achieve the Block Error Ratio (BLER) target.

Finally OuLPC is used to maintain the quality of communication at the level of bearer service quality requirement, while using as low power as possible. It happens at a rate of 1500 Hz to combat fast fading. The UL OuLPC is responsible for setting a target SIR in the Node B for each individual UL ILPC. This target SIR is updated for each UE according to the estimated UL quality (Block Error Ratio, Bit Error Ratio) for each RRC connection. The DL outer loop power control is the ability of the UE receiver to converge to required link quality set by the Radio Network Controller (RNC) in DL. If the received SIR is less than this target, transmit power needs to be increased. Otherwise, it needs to be decreased. In practice, DL target quality is in terms of transport channel BLER. The BLER can be related to a target SIR. If the received SIR is less than the target, BLER is likely to be not met. Alternatively, if the BLER is more than the target, transmit power has to be increased. This control is in the UE and the RNC.

2.1.3 LTE

When addressing the radio interface of Long Term Evolution (LTE), there are many aspects that need to be covered, such as resource allocation, modulation schemes, data and control channels, frequency bands, multiple access techniques and generic output power. This section covers these topics based mainly on [3GPP13a] and [HoTo11].

The operating frequency bands allocated for the Evolved UMTS Radio Access (E-UTRA) have been in constant change since the 3GPP Release 8 initially defined 17 operating bands for FDD and 8 for TDD, the two duplexing techniques used in LTE. Later, in LTE Release 11, E-UTRA was set to operate in 39 frequency bands, with 27 assigned to FDD and 12 to TDD. The available spectrum issued and auctioned by the National Communications Authority (ANACOM) included the bands of 450, 800, 900, 1800, 2100 and 2600 MHz, although the operators in Portugal only chose the bands of 800, 1800 and 2600 MHz for LTE. A more detailed table regarding this topic is shown in Annex A.

In LTE, DL is based on Orthogonal Frequency Division Multiple Access (OFDMA) and UL on Single Access Frequency Division Multiple Access (SC-FDMA). While OFDMA modulates the signal into a multitude of mutual orthogonal narrowband subcarriers with steps of 15 kHz that can be shared among multiple users (mitigating the Adjacent Channel Interference (ACI)), in SC-FDMA the information is modulated into just one carrier. LTE also uses Cyclic Prefix (CP) in both multiple access techniques to avoid Inter-Symbol Interference (ISI) by copying the last part of the symbol to the beginning, so it becomes periodic and large enough to ensure that it exceeds the delay spread. In order to have a better understanding of the main differences between the two schemes, Figure 2.1 presents an example comparing OFDMA and SC-FDMA.

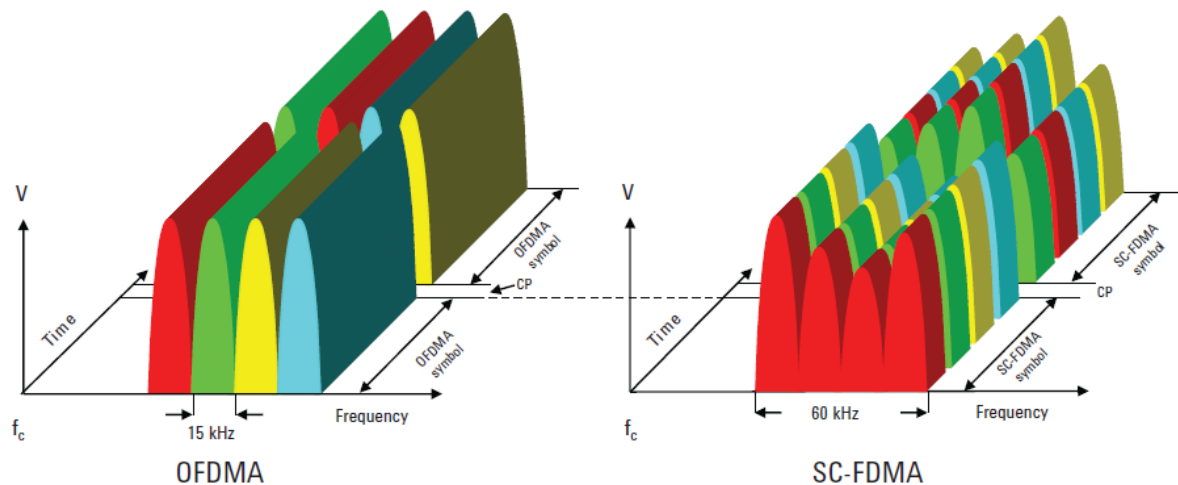


Figure 2.1 - Comparison between the transmission in OFDMA and SC-FDMA (adapted from [Agil09]).

The reason for using different techniques in UL and DL are the benefits and the positive aspects of each. While SC-FDMA optimises range and power consumption, OFDMA minimises receiver complexity, enables frequency domain scheduling with flexibility in resource allocation and has good compatibility with advanced receiver and antenna technologies. Although OFDMA's transmission allows users to be allocated to any of the sub-carriers, thus enabling frequency domain diversity, it also creates one limitation: the allocation should not be done on a single sub-carrier basis due to the resulting overhead. This allocation of sub-carriers is done in groups of 12, corresponding to a Resource Block (RB) resulting in a 180 kHz minimum bandwidth (due to the 15 kHz step) in both DL and UL, Figure 2.2.

Another fundamental enhancement included in LTE radio interface specifications is the use of multiple antenna techniques. They were introduced to achieve improved system performance, both in capacity and coverage, as well as in service provisioning, for instance, providing higher user data rates. Multiple Input Multiple Output (MIMO) is the most common technique, where multiple antennas are used simultaneously for transmission and reception over the radio channel. Besides MIMO, there are three additional types of transmission schemes, which are SISO, MISO and SIMO. Each of these schemes allows to take advantage from different types of diversity gains, namely, spatial multiplexing and transmit diversity.

MIMO introduces some important functions:

- Spatial multiplexing, where two or more antennas transmit signals, with different data streams, separated at the receiver and then processed, increasing the peak data rate by a factor of two or more, depending on the configuration.
- Pre-coding of the signals transmitted from the different antennas in order to maximise the Signal to Noise Ratio (SNR) in the receiver.
- Transmit diversity, which corresponds to a transmission of the same signal through multiple antennas in order to exploit the gains from independent fading between the antennas.

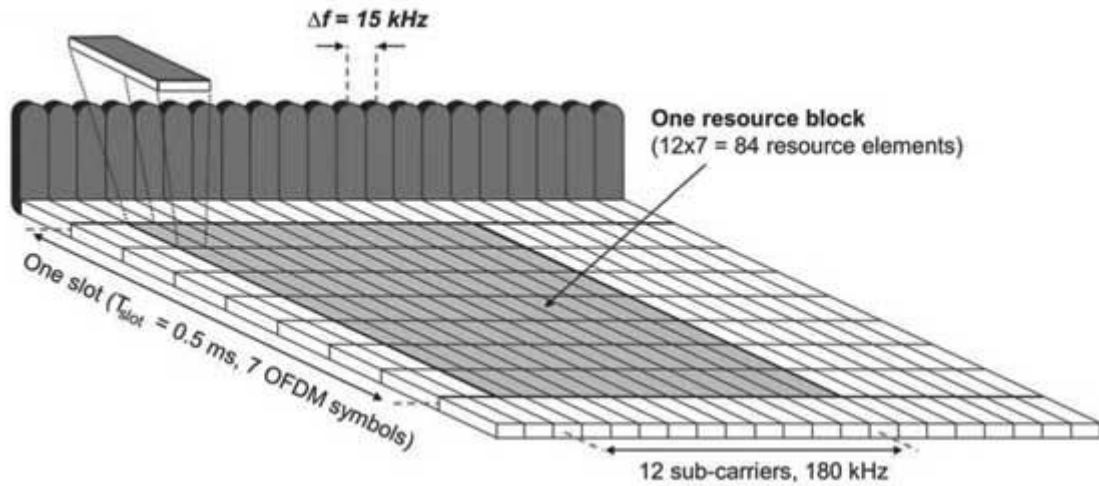


Figure 2.2 - LTE DL physical resource based on OFDMA (extracted from [Eric11]).

Finally regarding output power, perhaps the most important aspect of LTE for this work, power control is only specified for UL, thus balancing the need for sufficient transmitted energy to satisfy the required QoS, against the need to minimise interference on other users of the system and to maximise the battery life of the UE.

The metrics evaluated under the transmit power category include Maximum Output Power (MOP), Maximum Power Reduction (MPR), and UE Additional Maximum Power Reduction (A-MPR). For the LTE UL, output power is not a simple metric with a single maximum value for each UE power class. In actual use, a UE cannot transmit excess power because it has the potential to interfere with other UEs and adjacent systems. MOP defines the maximum transmitted power in the channel bandwidth for all transmission bandwidths, and as stated before, LTE measures transmission bandwidth in units of resource blocks.

MPR is a power reduction value used to control the Adjacent Channel Leakage Power Ratio (ACLR) associated with the various modulation schemes and the transmission bandwidth. An adjacent channel may be either another E-UTRA channel or an UTRA channel. Different ACLR specifications apply to either scenario. When the situation warrants it, the LTE network can indicate to the UE that additional spectral emission control is necessary. A-MPR is not power control but power reduction due to specific regulatory or deployment constraints.

The specification indicates that the application of A-MPR should be the exception rather than the rule with the admonishment that additional spectrum emission requirements should only be used in a restricted set of transmission bandwidth configurations and deployment scenarios. A set of network signalled values is based on the E-UTRA band, the channel bandwidth, and the number of resource blocks in use.

Taking Power Class 3 as an example, since it has been defined for all applicable 3GPP frequency bands and is the most common mobile phone class, the specified output power range is $[-40, 23] \text{ dBm}$. Using power control, the UE must be able to set its output power accurately across this range. When commanded to the minimum power control value, the UE must transmit at or below the specified

-40 dBm. Excess minimum output power, like excess maximum power, can adversely influence the coverage area and performance of other UEs accessing the system. As the circuitry that drives the UE is always active, residual output power is present when the transmitter is not actively sending data. The residual power transmitted during off periods must be less or equal to -50 dBm.

2.2 Human body characterisation and modelling

2.2.1 Dielectric properties

The dielectric properties of a biological tissue are a measure of the interaction of electromagnetic radiation with its constituents at the cellular and molecular level. Its analysis and study are all fairly recent, starting only on the second half of the last century and culminating so far in [Ga96], considered to be the best database regarding this topic to this day. Although [Ga96] only realises testing *in vitro*, recent researches have shown that the results *in vivo* are very approximate [GaPH05] and do not need correction.

The main features of the dielectric spectrum of a biological tissue are as follows: the dielectric properties of tissues are highly frequency and temperature dependent, and their dielectric spectrum consists of three main regions known as α , β and γ dispersions, respectively referred to as occurring at low, intermediate and high frequencies in the frequency range from units of hertz to gigahertz. This work only addresses the γ dispersion, since LTE ranges from 800 MHz to 2600 MHz in Portugal, which is the case in study.

The γ dispersion is due to the polarisation and relaxation of the water molecules, this being the main reason for different test results in different ages (variation of water in tissues). High water content tissue exhibits γ dispersion similar to that of pure water when the presence of organic matter is taken into consideration. The frequency dependence of the complex permittivity in the γ dispersion region may be expressed as:

$$\varepsilon(\omega) = \varepsilon_{\infty} + \frac{\varepsilon_s - \varepsilon_{\infty}}{1 + (j\omega\tau)^{1-\alpha}} + \frac{\sigma_l}{j\omega\varepsilon_0} \quad (2.1)$$

where:

- ε_{∞} : permittivity in the THz frequency range,
- σ_l : ionic conductivity,
- τ : mean relaxation time

As seen in [Ga96], this is the well-known Cole-Cole expression in which ε_{∞} is the permittivity at field frequencies where $\omega\tau \gg 1$, and ε_s the permittivity at $\omega\tau \ll 1$, α is parameter describing some broadening of the dispersion and σ_l is the conductivity due to ionic drift and to the lower frequency polarisation mechanisms. The value of the distribution parameter α is zero for pure water, but ≥ 0 for

most tissues and negligible body fluids. In tissue, the mean relaxation time τ is generally longer than the corresponding value for pure water, indicating a restriction in the rotational ability of at least some of the tissue water molecules due to the organic environment.

Another thing to be mentioned is the dielectric boundary conditions, since the environments under study is air and various body tissues. Suppose an interface between two different dielectric regions, each one with a respective permittivity ϵ' and ϵ'' . The magnitude for the electric field is different for each region, and in order to relate those fields it is necessary to assure the dielectric boundary conditions.

Both E and H fields can be decomposed in terms of tangential and normal components taking as reference the boundary between the dielectrics. It is important to refer that boundary conditions just give information about the relation between the vector fields only in the dielectrics interface.

Table 2.2 - Electrical properties of the body tissues at the different frequency bands [ITIS14].

Frequency [MHz]	Relative Permittivity ϵ_r			Conductivity σ [S/m]		
	800	1800	2600	800	1800	2600
Skin (Dry)	42.0	38.9	37.8	0.834	1.180	1.540
Skin (Wet)	46.5	43.8	42.6	0.808	1.232	1.684
Fat	11.4	11.0	10.8	0.102	0.190	0.288
Muscle	55.3	53.5	52.5	0.910	1.340	1.840
Cerebellum	50.2	46.1	44.5	0.122	1.710	2.200
Skull	12.6	11.8	11.3	0.132	0.275	0.424

The values for relative permittivity and conductivity for the main human tissues regarding mobile communications, at the LTE's operating frequencies in Portugal, are shown in Table 2.2. A more detailed table and chart is shown in Annex B.

2.2.2 Modelling

The evaluation of the MT antenna's performance is difficult, because it is almost impossible to make any antenna measurements in a real operating scenario. For this reason, simulation models and physical models (phantoms) are extremely important to predict the behaviour of the antenna and the whole system performance. Phantoms can vary from complete bodies in a specific position or just a part of it, such as a head, a torso, an arm and any other part that is required depending on the objective of the research. This section covers these topics based mainly on the works of [GePaSo10], [Lo10] and [Ma13].

In measurements, the most widespread solution is the use of body tissue simulating liquids that fill a container with a regular or an anatomical shape (liquid phantom). The antenna is then sunk into the liquid and measurements are carried out. The main advantage of this method is that it is easy and practical to implement. Recently, more authors have been working on the use of tissue simulating gels trying to obtain a multi-layered structure (semisolid). Others have carried out measurements with real tissues, whether that is animal or human tissue (*in vitro* and *in vivo*).

Semisolid (gel) phantoms possess a coagulant in order to self-shaping and eliminate phantoms' outer shell. A gel phantom was developed, being composed by water, TX-150 (polyamide resin), sodium chloride and polyethylene powder. These last two components are responsible for the control of conductivity and relative permittivity, respectively. These types of phantoms are mainly used to simulate organs with a high percentage of water, such as brain and muscle. This type of phantom has in its constitution another substance, polyacrylamide, which is a very toxic material, requiring special care. The great advantage of this substance is the fact that it simulates equally materials with a high and low percentage of water, however, it degrades over time due to water loss and/or fungi growth.

Liquid phantoms are the oldest phantom types. These phantoms are used in SAR studies, measuring in a very accurate way the distribution of the electric fields inside the phantom with a probe (for further information see Section 2.3). This type of phantom also has a very narrow band in which dielectric properties are equal to human tissues, besides that, it is difficult to handle the container in the test environment and the container dielectric characteristics are also difficult to set. Despite these inconvenient, it has the advantage of being easy to fabricate.

In digital simulations, as seen in Figure 2.3, the option that is simplest and fastest (but less accurate) is the one that uses a single layer structure, equivalent to measurements made with tissue simulating liquids. Other options are the use of multi-layered structures, with finite or infinite dimensions, or the use of 3D anatomical models. These realistic anatomical models offer more accurate results, but the computational requirements are higher, although the costs become lower.

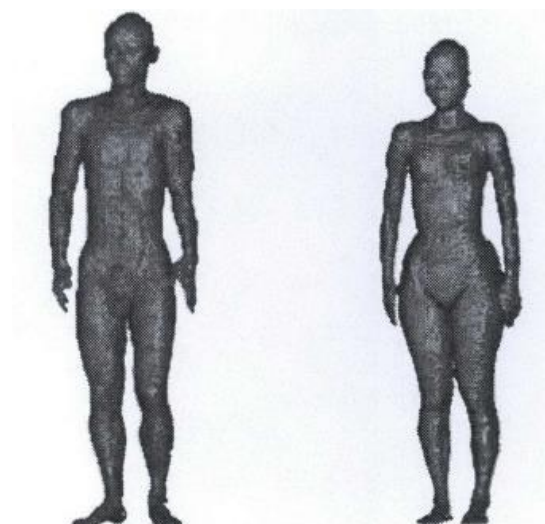


Figure 2.3 - High-resolution whole-body Japanese human voxel model (extracted from [Ito07]).

In these type of simulations, a number of realistic heterogeneous body models are currently used for

electromagnetic field simulations, consisting of large datasets obtained from Magnetic Resonance Imaging (MRI), Computer Tomography (CT), and anatomical images. Data are represented by voxel images of thin slices of the body, and each voxel corresponds to a particular type of the body tissue. In general, heterogeneous body models provide the highest accuracy. Although this is one of the best options, when it comes to simulate a real human body, the two major issues are the difficulty in obtaining useful images and handling the large amount of data created from these images. CT scans give the human body a large dose of ionising radiation – something the computational phantom was designed to circumvent in the first place. MRI images take a long time to process. Furthermore, most scans of a single subject cover only a small portion of the body, whereas a full scan series is needed for useful data. Handling this large amount of data is also difficult. While the more recent computers have hard drives large enough to store the data, the memory requirements for processing the images to the desired voxel size are often too steep.

2.3 Electromagnetic Radiation Exposure

Absorption of Radio Frequency Radiation (RFR) depends on many factors, including frequency, power density, user distance from the radiating source and also user orientation towards it. Other factors may include the size, shape, mineral and water content of an organism. Children may absorb energy differently than adults because of differences in their anatomies and tissue composition. Similarly to these differences, the same can be presumed for proximity to BSs and MTs and the difference in exposure to each of them. Under most circumstances, exposure is lower from BSs than from MTs, due to the difference of distance from the source. The MT is (most commonly) placed directly against the head during its use, whereas the distance to a BS is much larger, and thus exposure is lower.

The term used to describe the absorption of RF by the body is SAR, which is the rate of energy that is actually absorbed by a unit of tissue. SAR is generally expressed in watts per kilogram (W/kg) of tissue. SAR measurements are averaged either over the whole body, or over a small volume of tissue, typically between 1 g and 10 g of tissue. SAR is used to quantify energy absorption of fields typically between 100 kHz and 10 GHz, and encompasses RF from devices such as mobile phones up through diagnostic MRI, and since mobile communications use the RF band (non-ionising radiation), that is the portion of the Electromagnetic (EM) spectrum analysed in this work.

Two potential types of biological effects are associated to RF: thermal and non-thermal ones. Regarding the non-thermal effects, the publication of the International Commission on Non-Ionising Radiation Protection (ICNIRP) guidelines for limiting exposure to EM fields, [ICNIRP], refers that the works presented in the relevant literature on human potential health effects associated with EM exposure are inconclusive. These studies provided no evidence of adverse effects, since the results are based on a small number of samples, and due to the inability to reproduce satisfactory results of the in-vitro experiments obtained in laboratory.

Concerning thermal effects, these consist of the increase of tissue temperature resulting from the absorption of energy of the radiated field. Tissue heating is the most widely accepted mechanism of microwave radiation with biological systems. The effect can result from elevations of tissue temperature induced by RF energy deposited or absorbed in biological systems through local, partial-body or whole-body exposures. The bulk properties of complex permittivity and electrical conductivity cause the electric fields and currents induced to be absorbed and dissipated in cells and tissues of the human body. For a single pulse or brief application of RF energy, exposure duration may not be long enough for significant conductive or convective heat transfer to contribute to tissue temperature rise. In this case, the time rate of rise in temperature is proportional to SAR. For longer exposure durations, RF energy-induced temperature rise depends on the animal or tissue target, their thermal regulatory behaviour and active compensation process. For local or partial body exposures, if the amount of RF absorbed energy is excessive, rapid temperature rise and local tissue damage can occur. Under moderate conditions, a temperature rise on the order of 1°C in humans and laboratory animals can result in a SAR input of 4 W/kg, which belongs to the normal range of human thermoregulatory capacity.

SAR can be measured in a single point or considering a certain volume. The standard values of SAR are measured for 1 g of tissue or 10 g of tissue, 10 g being the most common choice. In more detail, SAR is defined as the time derivative of the incremental energy (dW) absorbed by or dissipated in an incremental mass (dm) contained in a volume element (dV) of a given density (ρ). An equivalent method is to take a temperature measurement.

Table 2.3 - Reference and alternate methodologies established by EN 50383 standard (extracted from [CENE13]).

	Reactive near-field region	Radiating near-field region	Far-field region
Reference	SAR evaluation	SAR evaluation	E-field or H-field calculation
First alternative	E-field or H-field measurement	E-field or H-field measurement	E-field or H-field measurement
Second alternative	-	E-field or H-field calculation	-

SAR is proportional to the temperature increase ΔT , when the effects of thermal conduction, convection and radiation are negligible, in the time interval Δt . So, one has SAR as being defined by [KSMVK13]:

$$SAR = -\frac{d}{dt} \frac{dW}{dm} = \frac{d}{dt} \frac{dW}{\rho(dV)} \quad (2.2)$$

although the most common expression can be written as:

$$SAR = \frac{\sigma}{2\rho} E^2 \quad (2.3)$$

with E as the induced electric field in V/m, ρ the density of the tissue in kg/m³ and σ the conductivity of the tissue in S/m. The same can also be evaluated using the Poynting vector theorem for sinusoidal

varying electromagnetic fields:

$$SAR = -\frac{\omega \varepsilon_0}{2\rho} - |E_i|^2 = \frac{\varepsilon}{2\rho} - |E_i|^2 \quad (2.4)$$

where $|E_i|^2$ is the peak value of the internal electric field.

Different worldwide entities, like ICNIRP, have established guidelines to limit electromagnetic exposure, in order to provide protection against adverse health effects. These guidelines need to be taken into account when assessing exposure to radiation in public accessible areas, i.e., there are reference levels that have to be compared with the measured values of physical quantities. If the measured values comply with the reference levels, compliance with basic restrictions (SAR) is ensured; otherwise, a more detailed analysis is necessary to assess compliance. In situations of simultaneous exposure, and taking the frequency band under study into consideration, the following requirement for the electric field and magnetic field levels should be applied [ICNI98]:

$$\sum_{i>800 \text{ MHz}}^{2600 \text{ MHz}} \left(\frac{E_{i[\text{V/m}]}}{E_{ref,i[\text{V/m}]}} \right)^2 \leq 1 \quad (2.5)$$

$$\sum_{j>800 \text{ MHz}}^{2600 \text{ MHz}} \left(\frac{H_{j[\text{A/m}]}}{H_{ref,j[\text{A/m}]}} \right)^2 \leq 1 \quad (2.6)$$

with:

- E_i : Electric field strength at frequency i ;
- $E_{ref,i}$: Electric field reference level at frequency i ;
- H_j : Magnetic field strength at frequency j ;
- $H_{ref,j}$: Magnetic field reference level at frequency j ;

Most European countries, such as Portugal, adopted the exposure thresholds established by the European Union Recommendation based on ICNIRP guidelines [ICNI09]. These guidelines have been developed from immediate health effects, hence long-term effects are poorly assessed. These short-term effects are stimulation of peripheral nerves or muscles, shocks and burns indirectly induced in metal objects exposed to radiation, and elevated tissue temperature due to absorption of energy of the electromagnetic field (EMF) exposure. The recommendation presents a basic restriction for particular areas of the body and for the whole body, and maximum permissible exposure values, which are the limits derived from the basic restrictions.

For the frequency ranges of interest in this work, reference thresholds for general public are presented in Table 2.7 in accordance with ICNIRP guidelines. Basic restrictions were applied to reference thresholds for occupational exposure with the objective of obtaining reference thresholds for exposure of the general public. For the analysed frequencies, the electric field E , magnetic field intensity H , magnetic induction B and the directional energy flux density S values are evaluated over the entire body, and these values must be measured, averaged over any 6 minutes period.

Table 2.4 - Reference values for general public exposure [ICNI09]

Frequency range [GHz]	E [V/m]	H [A/m]	B_m [μ T]	S [W/m ²]
[0.4, 2.0]	$1.375 \times f_{[MHz]}^{1/2}$	$0.0037 \times f_{[MHz]}^{1/2}$	$0.0046 \times f_{[MHz]}^{1/2}$	$f_{[MHz]}/200$
[2.0, 300.0]	61	0.16	0.20	10

2.4 Field regions

This section covers the fundamental concepts and differences between near and far field, while going into more detail regarding near field, since that is the main region of the work at hand. It also covers an overview of the transition zone between both regions.

At close proximity to an antenna, the characteristics of electromagnetic fields are unpredictable and the electric field E can dominate at a location, while the magnetic field H can dominate just a few centimetres either way. Predictions are very difficult in this region and boundary regions have been defined to categorise the behaviour/characteristic of EM fields as a function of distance from the radiator. As shown in Figure 2.4, where D is the maximum size of the antenna and R_1 and R_2 represent respectively the range of the reactive and radiating near-fields, the space surrounding an antenna is divided into field regions defined as: near-field region (reactive/evanescent near-field), radiating (Fresnel) near-field, transition zone (intermediate-field region) and the far-field (Fraunhofer) region.

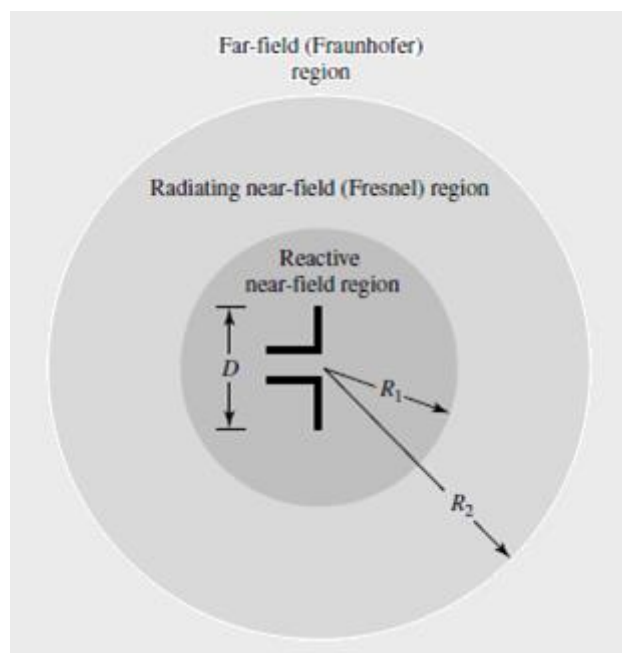


Figure 2.4 - Field regions of an antenna (extracted from [Ba05])

These regions are so designated to identify the field structure in each. Although no abrupt changes in the field configurations are noted as the boundaries are crossed, there are distinct differences among them. The boundaries separating these regions are not unique, although various criteria have been established and are commonly used to identify the regions.

The reactive near-field region is defined as the portion of the near-field region immediately surrounding the antenna, wherein the reactive field predominates. For most antennas, the outer boundary of this region is commonly taken to exist at a distance R_1 from the antenna surface. This distance is given by:

$$R_1 < 0.62\sqrt{D^3/\lambda} \quad (2.7)$$

with:

- λ : wavelength;
- D : largest dimension of the antenna.

For a very short dipole, or equivalent radiator, the outer boundary is commonly taken to exist at a distance $\lambda/2\pi$ from the antenna surface, according to [Ba05].

The radiating near-field (Fresnel) region is defined as the region of the field of an antenna between the reactive near-field region and the far-field region wherein radiation fields predominate and wherein the angular field distribution is dependent upon the distance from the antenna. If the antenna has a maximum dimension that is not large compared to the wavelength, this region may not exist (which may be the case in this work). The inner boundary is taken to be the distance R_1 and the outer boundary the distance R_2 given by:

$$R_2 < 2D^2/\lambda \quad (2.8)$$

In this region the field pattern is, in general, a function of the radial distance and the radial field component may be appreciable [Ba05].

According to [Ag11], for an antenna that is electrically small compared to the wavelength, the transition is considered to exist at distances anywhere between 0.1λ and λ from the antenna, essentially between the radiating near-field and the far-field regions. This region is comprised of a combination of the characteristics found in both the near- and the far-fields, but the far-field characteristics are becoming more evident moving outwards. This region is delimited by $[0.5D^2/\lambda ; 2D^2/\lambda]$ and is assumed to be the region in which the far-field starts.

The most useful region for simple calculations is the far-field region. This region is far enough from the antenna to neglect its size and shape, and it can be assumed that the electromagnetic wave is purely a radiating plane wave (electric and magnetic fields are in phase and perpendicular to each other and to the direction of propagation), which greatly simplifies the modelling of the problems. The far-field patterns of certain antennas, such as multibeam reflector antennas, are sensitive to variations in phase over their apertures; for these antennas, $2D^2/\lambda$ may be inadequate, [RWY95]. In this region, the field components are essentially transverse and the angular distribution is independent of the radial distance

where the measurements are made, and the field strength can be described by simple expressions, Figure 2.5.

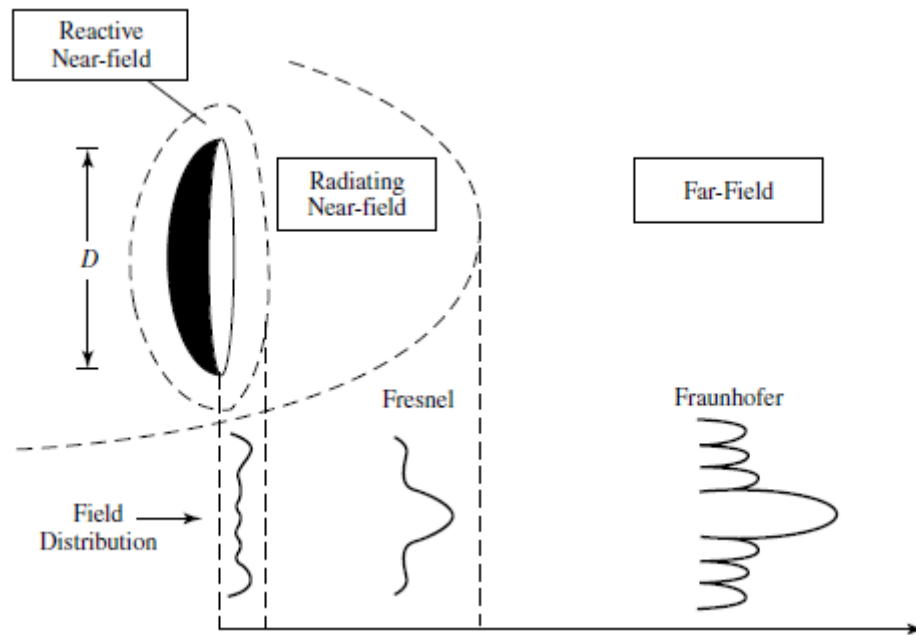


Figure 2.5 - Typical changes of antenna amplitude pattern from the reactive near field to far field (extracted from [RWY95]).

2.5 State of the Art

A brief overview of the state of the art is presented in this section, in order to show what has been done in this field up to now, thus, emphasising the importance of this work.

Wireless technologies are omnipresent today and MTs (the most common being mobile phones) are one of the prodigious output of this technology. Although the familiarisation with and dependency of MTs is growing at an alarming pace, the biological effects due to the exposure of radiation have become a subject of intense debate. The present evidence on the devices' radiation exposure is based on scientific research and public policy initiatives to give an overview of what is known of biological effects that occur at RF/EMFs exposure. The conflict in conclusions is mainly due to the difficulty in controlling the affecting parameters. Furthermore, the work done so far consists, in its majority, of short term measures and evaluations. Even official reports, such as the ones delivered by the entities that establish guidelines (FCC in the United States of America and ICNIRP in Europe), [FCC13] and [ICNI09], acknowledge this fact somehow.

A study published in 2007 [Ha07] examined the incidence of malignant brain tumours among thousands of individuals. This study is among the first epidemiological studies using such a large number of subjects over an extended evaluation period. In this work, it is stated that not only does mobile phone

use increases the risk of forming malignant brain tumours, but that the risk increases with latency time (in other words, how much time has passed since the mobile phone exposure) and cumulative use. And although no consensus on the topic has been reached, in May 31st, 2011 the World Health Organisation (WHO) decided to identify RF EMF as a Class 2B Carcinogen [WHO11].

According to [TGSW10], “The averaged local exposure in the head induced by the mobile phone is considerably higher than that of the far field sources such as base stations and broadcasts sources. For example, the spatial peak SAR value in the brain during usage of a mobile phone can reach 1 W/kg which is more than five orders of magnitude larger than the corresponding value in a person exposed to an incident field of 1 V/m (corresponds $\sim 1 \mu\text{W/kg}$), for whole body averaged SAR levels of about 10 $\mu\text{W/kg}$, approximately corresponding to $>0,5 \text{ V/m}$ incident plane wave exposure. Estimating the cumulative exposure, about 30 min of mobile phone use corresponds to 1 day exposure from far field source at an incident level of 1–2 V/m.”

Although the *Interphone study*, coordinated by the International Agency for Research on Cancer (IARC), shows no risk for users with an average 2 to 2.5 hours mobile phone use a month, it shows a 40% increase risk in brain tumour glioma for intensive mobile phone users – defined in the study as 1640 hours or more cumulative mobile phone use, or 30-minute daily use over a 10-year period of time [Ca10].

A 2011 pooled analysis by Swedish researchers indicates a dose response that the risk of brain tumours (both glioma and astrocytoma) increased significantly for every 100 hours of cumulative exposure [HaCa09]. Other reported cumulative biological effects from exposure include effects on the Central Nervous System (CNS) and DNA damage [LaBuPo98]. Since *Glass* is designed to be worn on the user's head all day long, the potential cumulative exposure time from its use is expected to be much longer than from ordinary mobile phones, and therefore the potential health risk for this new device could be much higher than other mobile devices. Also, the laterality of mobile phone use, whether it is used primarily on one side of the head (ipsilateral use) or on both sides (contralateral use), also plays an important role in evaluating the risk of brain tumours. [Ca10] shows that among intensive users, ipsilateral ones had a nearly doubled risk of glioma (compared to 40% increase for all) and tumours were more likely to occur on the side of the head most used for calling. The higher risk for ipsilateral exposure was also confirmed in other epidemiological studies – [Ha07], [HaCa09] and [KTKH09].

Since wireless energy absorption in brain tissue is non-uniform, specific points are more irradiated in certain areas of the brain close to the transmitting antenna. These “hotspots” are most problematic when it comes to the health risk of wireless systems radiation. Besides the duration, *Glass* is designed to be worn in the same position all the time, and the same part of the brain in close vicinity to *Glass*'s transmitting antenna is subject to the highest localised exposure all the time. As a result, the long-term ipsilateral exposure could give *Google Glass* users a much higher risk of brain damage than mobile phone users.

As a body-worn, microwave-emitting device, *Glass* is required to undergo measures and tests regarding its SAR values, before being released to the general public. As for the maximum SAR value associated with a certain device, ICNIRP has defined 2 W/kg [ICNI09] and the FCC has defined 1.60 W/Kg [FCC13]. The first reports delivered by Google to the FCC showed that *Glass* has a maximum SAR of 1.10 W/Kg,

but later, after improving the antenna of the device, the maximum SAR value increased to 1.42 W/Kg [Ba13]. Although these values make it theoretically safe for use, according to the current regulations, the continuous and prolonged use of the device at such close range to the head of the user has to be taken into consideration. As stated before, the report delivered with the assessment of *Glass*'s SAR value was made with an exposure of 6 minutes long and 1.42 W/Kg is the peak value, that is, no information is given regarding the SAR value over time.

In conclusion, and although an LTE (or similar) antenna is needed in the device, this prototype makes an ideal test device for the current work, since it will allow for a prolonged, continuous and adjacent exposure to radiation, which is the main purpose of the work at hand.

Chapter 3

Modelling and Simulation

This chapter provides the problem description, an overview of the simulation tools used, and the chosen scenario.

3.1 CST Simulator

CST Studio Suite 2011 [CST14] is the numerical model simulation tool chosen to simulate the interaction of electromagnetic fields with physical objects and the surrounding environment. Among the many features this software presents, only the *CST Microwave Studio* is used since it is the most adequate module to simulate 3D electromagnetic high frequency waves. It also has the ability to import human voxel models, creation and use of realistic antennas, calculation of 3D radiation patterns, s-parameters, time signals and SAR readings.

CST is based on the Finite Integration Technique (FIT) as the numerical method for its simulations. This method performs a spatial discretisation scheme applicable to various electromagnetic problems ranging from static field calculations to high frequency applications in time or frequency domain. Unlike most numerical methods, FIT discretises the integral form of Maxwell's equations [FI08].

To solve these equations numerically, a finite calculation domain must first be defined, enclosing the considered application problem. Creating a suitable mesh system splits this domain up into many small orthogonal elements (grid cells) in hexahedral shape. Maxwell's equations are formulated for each side of the cells, as seen on Figure 3.1. For the complete discretisation of Maxwell's equations in each single cell facet, two dual grid systems are required, the primary grid \mathbf{G} and the secondary dual one, \mathbf{G}' . The primary grid contains the electric grid voltages e and the magnetic facet fluxes b , while the secondary dual one allocates the dielectric facet fluxes d and the magnetic grid voltages d .

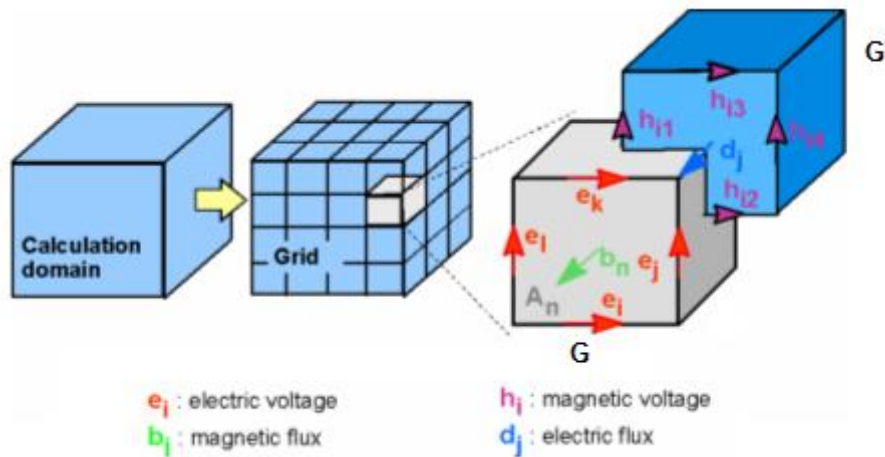


Figure 3.1 - FIT spatial discretisation scheme (adapted from [CST14]).

This course of action, for all existing cell sides, condense the calculation rule in a matrix formulation, introducing the topological matrix \mathbf{C} as the discrete correspondent of the analytical curl operator as shown in Figure 3.2.

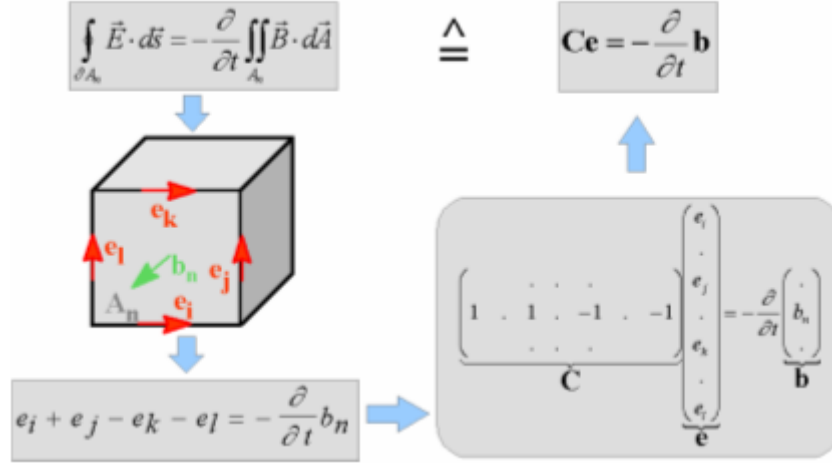


Figure 3.2 - Representation of the discretisation of Maxwell's integral equations (extracted from [CST14]).

For the cell complex pair $\{\mathbf{G}, \mathbf{G}^*\}$, the complete set of discretised matrix Maxwell's Grid Equations is given by:

$$\mathbf{C}\mathbf{e} = -\frac{d}{dt}\mathbf{b} \quad (3.1)$$

$$\mathbf{C}'_h \mathbf{d} = -\frac{d}{dt}\mathbf{h} + \mathbf{j}_c \quad (3.2)$$

$$\mathbf{S}'_d \mathbf{q} = \mathbf{0} \quad (3.3)$$

$$\mathbf{S}_b \mathbf{0} = \mathbf{0} \quad (3.4)$$

where:

- \mathbf{C} : discrete curl operator;
- \mathbf{C}' : dual discrete curl operator;
- \mathbf{S}_d : discrete divergence operator;
- \mathbf{S}'_d : dual discrete divergence operator;
- \mathbf{b} : magnetic flux;
- \mathbf{d} : electric flux;
- \mathbf{j} : electric flux density;
- \mathbf{h} : magnetic voltage;
- \mathbf{e} : electric voltage;
- \mathbf{q} : electric charge;

The second discrete differential operator is the divergence one, which describes the non-existence of magnetic charges within a cell volume. The evaluation of the surface integral yields a sum of six magnetic facet fluxes with different orientations, that when expanded to the whole cell complex creates the discrete divergence matrix \mathbf{S} . This matrix depends only on the grid topology, just as the discrete curl-matrix \mathbf{C} .

By analogy, the discretisation of Ampère's law is performed by summing up the magnetic grid voltages in order to obtain the displacement current and the conductive current through the considered cell facet. Finally, Gauss' law can be discretised for the dual grid cells, resulting in matrix equations featuring the topological grid operators \mathbf{C}' for the dual discrete curl and \mathbf{S}' for the dual discrete divergence.

The matrix equations for the electromagnetic integral quantities obtained by FIT ensure a positive stability and convergence behaviour in the numerical implementation, as the intrinsic properties of Maxwell's equations with respect to charge and energy conservation are kept. In order to complete the solution of the electromagnetic field problem on the discrete grid space, the material relations in matrix form are required:

$$\begin{aligned} D_i &= \varepsilon E & d &= M_\varepsilon e \\ B &= \mu H & \Rightarrow \quad b &= M_\mu h \\ J &= \sigma_c E + J_S & j_c &= M_{\sigma_c} e + j_S \end{aligned} \tag{3.5}$$

where:

- M_ε : permittivity matrix;
- M_μ : permeability matrix;
- J : current density;
- J_S : surface current density;
- M_{σ_c} : conductivity matrix;
- j_S : surface current density flux matrix.

It is worth noting that this last point introduces the numerical inaccuracy in the FIT method, as when defining the relations between voltages and fluxes, the integral values have to be approximated within the grid edges and cell areas. Thus, the resulting coefficients depend on the averaged material parameters, as well as on the spatial resolution of the grid. Moreover, the mesh grid can add dispersion to the model, which gets worse when the differences between two neighbouring mesh step sizes become larger. The smallest dispersion occurs in an equidistant mesh. In order to avoid these effects, the mesh generator may be forced to insert additional mesh lines that decrease the differences of mesh lengths. The accuracy of the results depends on the way the structure is discretised, being improved for very fine mesh grids, when the mesh size gets so small that the discrete lengths become differentials. However, the finer the mesh is, the larger the number of mesh cells is. With this, there is a larger number of unknowns to be solved, extending the need of memory and simulation time. The CST mesh generator determines the important features of the structure under analysis and automatically creates the mesh grid, representing the structure and the fields equally well. However, some parameters can be controlled by the user, as the Lines per Wavelength (LW) or the Mesh Line Ratio Limit (MLRL).

Not only the absolute number of mesh cells used is relevant, but also the distance between two mesh lines, which is decisive to define the mesh setting. The MLRL parameter sets the ratio limit between the highest and the smallest distances between mesh lines, forcing the algorithm not to overcome an absolute ratio. Thus, unacceptable calculation times derived from very close mesh lines in high accuracy

simulations are avoided. The MLRL setting strongly influences simulations, as the smallest distance existing in a mesh directly impacts on the width of the time steps usable in the simulation. The smaller the smallest distance, the smaller the time step and the longer it takes to simulate.

The simulation time is not only dependent on the number of unknowns, but also on the properties of the solver. Three solver types are available at CST: transient, frequency domain and eigenmode. From these, only the transient solver is used in this work. The transient solver allows the simulation of the problem in a wide frequency range, in a single computation run, providing the s-parameters in the desired frequency range and the electromagnetic field patterns at various frequencies. The fields are calculated step by step, through time, according to the “Leap Frog” updating scheme, Figure 3.3.

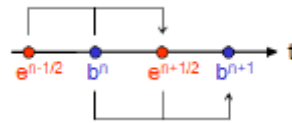


Figure 3.3 - Leap Frog scheme of CST Transient Solver (extracted from [CST14]).

The “Leap Frog” scheme remains stable if the step width for the integration does not overcome a maximum usable time step, which is directly related to the minimum mesh step width used in the discretisation of the structure. The denser the chosen grid, the smaller the usable time step width. Hence, a high mesh resolution of a small detail inside a given structure probably sets the global time step, and therefore the total simulation time.

Finally, for the simulation to be successful, a geometrical model of the problem under study has to be created together with the appropriate power sources (ports) and boundary conditions. The solver can only be started if at least one port is defined. In case of multiple ports, these ports may be stimulated differently: all ports stimulated sequentially, only one single port stimulated, some selected ports stimulated sequentially, or with some selected (or all) ports stimulated simultaneously.

3.2 Terminals and Antennas

This section covers the main aspects regarding terminals and antennas that radiate RF, namely mobile phones, while also going into more detail about the antenna used in the prototype of *Google Glass*. Therefore, only the denominated electrically small antennas are analysed, specifically the $\lambda/4$ monopole whip antenna. The information in this section is mainly based on [Ba05], [KhAzls14], [Kib13], [Wei03] and [Mai11].

The radiation pattern of an antennas shows its directional characteristics, which can usually be distorted by nearby obstacles, though by using a small antenna (in terms of wavelength) the directivity is minimised. Typically, these types of antennas have directivities less than 3 dB, meaning they radiate almost equally in all directions.

Since the main obstacle present in this work is human tissue, the subject of exposure and SAR values gain relevance, and the way it is measured depends on the different possible radiation field the tissue is subject to. Since the antenna in use for this work is a $\lambda/4$ monopole antenna with a maximum length of D , the equations for the limitations of each radiation field are given as:

- Reactive near-field: $[0, 0.62\sqrt{D^3/\lambda}]$
- Radiating near-field: $[0.62\sqrt{D^3/\lambda}, 2D^2/\lambda]$
- Far-field: from $R > 2D^2/\lambda$

Also depending on these radiation fields, the electric and magnetic fields intensity will vary. While in both near fields this intensity is highly irregular and very hard to measure or calculate, in the far field these values become more stable and easier to calculate. This also makes a more accurate and easier reading of the SAR values.

The radiating near-field region is the zone of interest for EMF estimation in areas closer to the antenna, since the reactive near-field region has very reduced dimensions. Thus, for a monopole antenna, the equations for this field are given as:

$$E_{\theta[V/m]} = \frac{Il\beta^3}{4\pi\omega\epsilon_0} \left[\frac{j}{\beta r} + \frac{1}{(\beta r)^2} + \frac{-j}{(\beta r)^3} \right] \sin(\theta) e^{-j\beta r} \quad (3.6)$$

$$H_{\phi[A/m]} = \frac{Il\beta^2}{4\pi} \left[\frac{-j}{j\beta r} + \frac{1}{(\beta r)^2} \right] \sin(\theta) e^{-j\beta r} \quad (3.7)$$

where:

- l : length of the monopole antenna
- I : wire current
- ϵ_0 : permittivity of free space
- r : distance to the antenna
- ω : angular frequency
- θ : angle between the zenith's wire axis and the observation point.

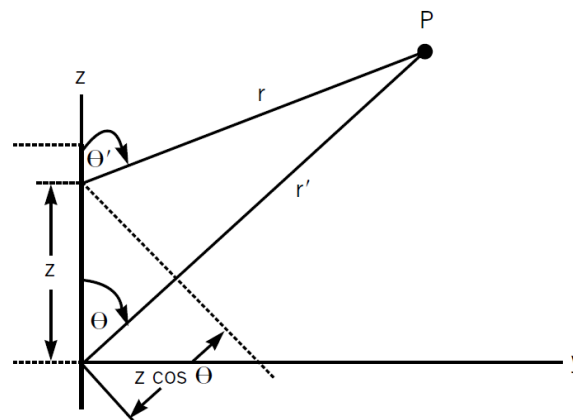


Figure 3.4 - Geometric approach for determination of E or H on point P (extracted from [ChCa01]).

As stated before, small antennas have very low directivity, but the peak gain of an antenna can also be arbitrarily low because of losses, *i.e.*, low efficiency. Due to these facts, electrically small antennas can

be very inefficient, with antenna gains lower than -10 dBi (even without accounting for impedance mismatch loss).

Regarding polarisation, for two linearly polarised antennas that are rotated from each other by an angle ϕ , the power loss due to this polarisation mismatch is described by the Polarisation Loss Factor (PLF), here denoted as δ :

$$\delta = \cos^2 \phi \quad (3.8)$$

Hence, if both antennas have the same polarisation there is no power loss due to polarisation mismatch. For a $\lambda/4$ monopole antenna on a finite rectangular ground plane, the radiation intensity for the electric and magnetic field can accordingly be given by:

$$E_{\theta[V/m]} = \frac{jZ'I_0 e^{j\beta r} \cos(\beta l \cos(\theta)) - \cos(\beta l)}{2\pi r \sin(\theta)} \quad (3.9)$$

$$H_{\phi[A/m]} = \frac{E_{\theta}}{Z'} = \frac{jI_0 e^{j\beta r} \cos(\beta l \cos(\theta)) - \cos(\beta l)}{2\pi r \sin(\theta)} \quad (3.10)$$

where:

- Z' : intrinsic impedance of the medium
- r : distance to antenna
- I_0 : Maximum possible current
- l : length of the monopole antenna
- β : electrical length per meter of wavelength

The average radiated power of a monopole antenna above ground ($0 \leq \theta \leq \frac{\pi}{2}$) can be given by:

$$\langle \vec{S} \rangle = \frac{Z'I_0^2}{8\pi^2 r^2} \sin^3(\theta) \quad (3.11)$$

and thus the total radiated power by the monopole is:

$$P_{rad} = \frac{3Z'I_0^2}{64} \quad (3.12)$$

Also, antennas can be classified as either resonant or non-resonant, depending on their design, which depends mainly on their impedance at the input of the antenna. An antenna with a real input impedance (zero imaginary part) is said to be resonant. In general, the feeding transmission line needs to be matched to the impedance of an antenna.

The dimensions required to design the physical aspects of the antenna are its length, the radius of the antenna's radiator (in our case the wire itself) and the dimensions for the rectangular ground plane. For the radiator, the length is a value close to:

$$l_a = \lambda/4 \quad (3.13)$$

and the radius is 0.5 mm, since the antenna under analysis is an electrically small one, and this is the

usual radius for this type of radiator.

Although these values are never completely precise, since they depend on frequency, impedance, height of the antenna, power feeding, among others, according to [Ba05] the quality factor, Q , of a thin wire antenna is considered to be higher than that of a thick wire, and since a low Q antenna is considered to be broadband, hence thick wire antennas have a wider bandwidth. Although these values depend on one another at a theoretical level, in practice the variation of the radius (on these types of antennas) is so small it can be negligible.

3.3 Modelling of Antenna

This chapter describes the steps made and the points taken into consideration while modelling the antenna on *CST MWS*. As stated before, the prototype chosen to simulate and to analyse is the *Google Glass*. In this prototype, according to [FCC14c] and as seen in Figure 3.5, the antenna is a monopole whip antenna, fed by a coaxial cable and working in the 2400 MHz band, using Wi-Fi and Bluetooth. Although this prototype does not use GSM, UMTS, LTE or any other cellular technologies, by changing its frequency to the ones used by these systems, one can still achieve the results regarding radiation exposure.

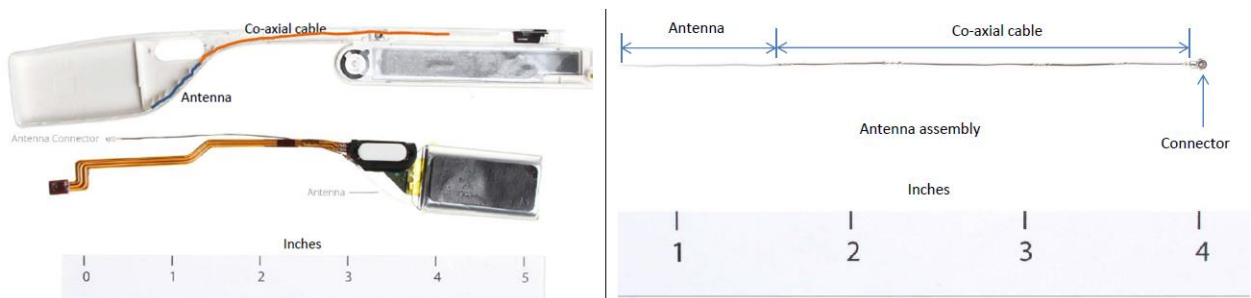


Figure 3.5 - *Google Glass* antenna, with reference ruler in inches (extracted from [FCC14]).

To recreate the real $\lambda/4$ monopole whip antenna in the simulator, it was decided to use the whip antenna connected to a ground plane, which is the most common $\lambda/4$ antenna format, even on mobile phones where the boards are used as a ground plane. The initial dimensions were the real ones taken from the datasheets provided by FCC [FCC14a].

The initial model was composed by a cylindrical shaped antenna with the dimensions of 22.9 mm in length and 0.5 mm in diameter, where it was decided to use a ground plane with similar dimensions to the board existing on the *Google Glass*, i.e., 40 mm long by 15 mm high by 0.3 mm wide. These dimensions were only a starting point, since the feeding system and the entire format of the real antenna is different from the one used in the simulator. While in this work a ground plane is used for the simulation, in the real prototype the antenna is fed by a coaxial cable, which is then connected to a microprocessor that regulates the power, frequency and other data being fed to the antenna. In this work, between the rod used as the antenna and the ground plane, a port had to be inserted for the

feeding of the antenna. The choice was a discrete port inserted in a gap 0.3 mm wide from one element to the other. The materials defined in the software were vacuum for the gap, whereas the other two elements are considered entirely as Perfect Electrical Conductor (PEC).

For a ground plane to properly work, even though [Ba05] states that it has to have at least 1 wavelength side and preferably be in a square shape, this is only true for planes that are used to reflect the wave transmitted by the antenna, and thus increasing its directivity. In this work, one only wants the plane to act as ground, so it was created with dimensions large enough to dissipate the energy, but small enough to fit the model of the *Glass*, as shown in Table 3.1, 29 mm in length, 10 mm in height and 0.3 mm wide, giving it a similar shape and dimensions as the board that exists on the real prototype.

Table 3.1 - Dimensions of the elements composing the model of the antenna in *CST*

	Ground plane	Port gap	Antenna rod
Length [mm]	29	0.3	22.9
Diameter [mm]	-	0.3	0.5
Height [mm]	10	-	-
Width [mm]	0.3	-	-

With the information gathered so far, one is already able to outline the limits between near and far field. This is visible in Table 3.2 with the aid of the equations found in last sub-chapter. Since the voxel model is at the distance of ~7 mm from the antenna, one can neglect the effects suffered from the near field, and only account for the far field henceforth.

Table 3.2 – Boundary between near field and far field for modelled antenna, at different frequencies.

Frequency band [GHz]	0.8	0.9	1.8	2.1	2.4	2.6
Limit between near/far field [mm]	2.9	3.1	6.3	7.3	8.4	8.9

As stated before, one would expected that this model would not be naturally resonant at 2.4 GHz (the working frequency band of the systems existing in the prototype) since its dimensions are not similar to the theoretical ones and also due to the different feeding type and the lack of other electronic elements that control the antenna. For the theoretical values, the length of the antenna is $\lambda/4$, so for an antenna working at 2400 MHz the corresponding wavelength is 12.49 cm, hence the length is 3.12 cm. Figure 3.6 shows the final result of the antenna design on *CTS*.

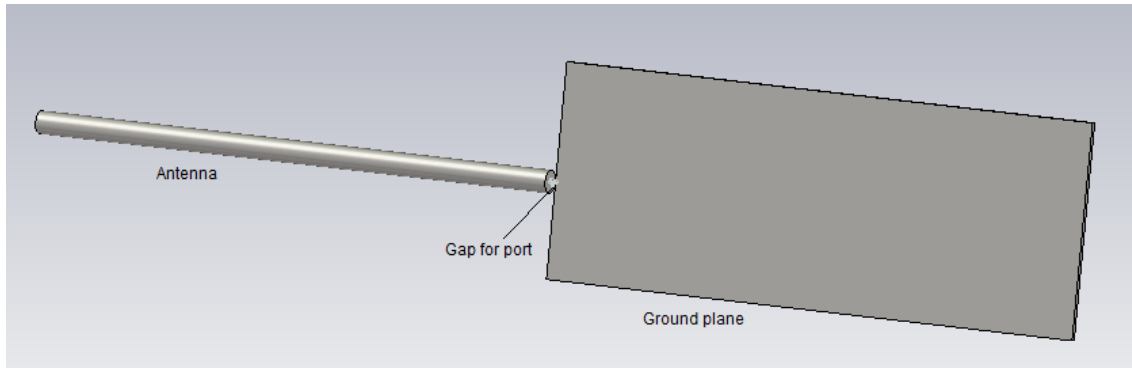


Figure 3.6 - Antenna model created on *CST MWS*

After the modelling phase was complete, simulations were made to assess the antenna's proprieties in vacuum, such as its reflection coefficient represented in Figure 3.7 and the evolution of the electrical field over the distance in Figure 3.8. Like stated before, one notices on Figure 3.7 the fact that the antenna is not naturally resonant at 2.4 GHz, and also on Figure 3.8 the difference in the behaviour of the electric field before entering the far-field zone.

Simulations were made for the entire range of the various frequency bands, i.e., GSM at 900 MHz and 1800 MHz, UMTS at 900 MHz and 2100 MHz, LTE at 800 MHz, 1800 MHz and 2600 MHz and finally Wi-Fi at 2400 MHz. The radiation patterns were also obtained in two 2D cut planes, Figure 3.9 and Figure 3.10, the former for a frontal view of the antenna and the latter for a side one.

In Annex D, different views of the 3D radiation pattern are also shown, in order to better grasp the matter, along with the tables registering the corresponding maximum for each electrical field in linear units, i.e., V/m, since the charts are presented in dB.

All the magnitudes are registered at a 10 cm distance, this being the distance from the antenna to the centre of the prototype, and later in this work, also the distance to the centre of the voxel model from the antenna.

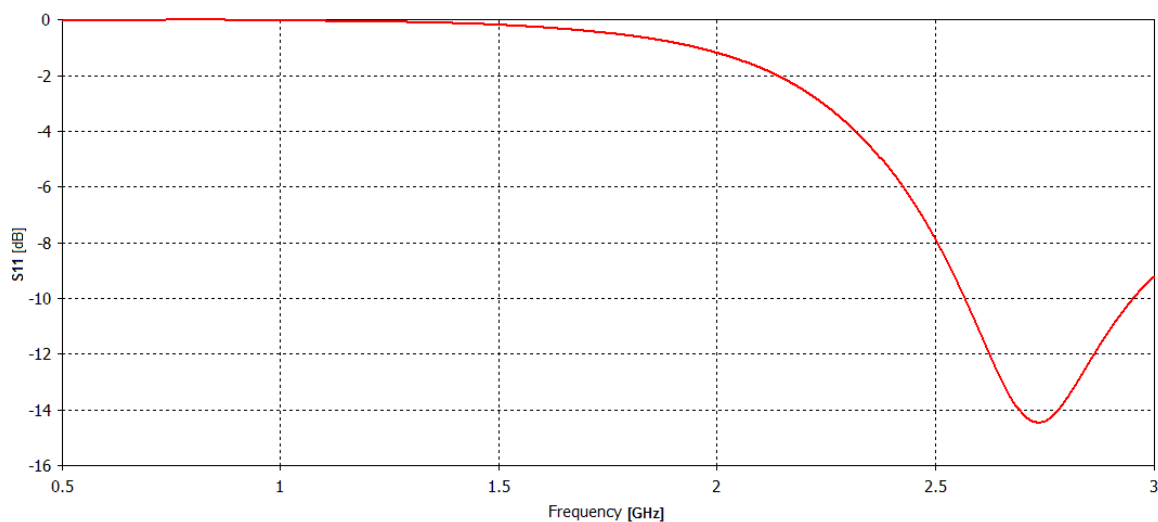


Figure 3.7 – S_{11} parameter for the antenna in vacuum.

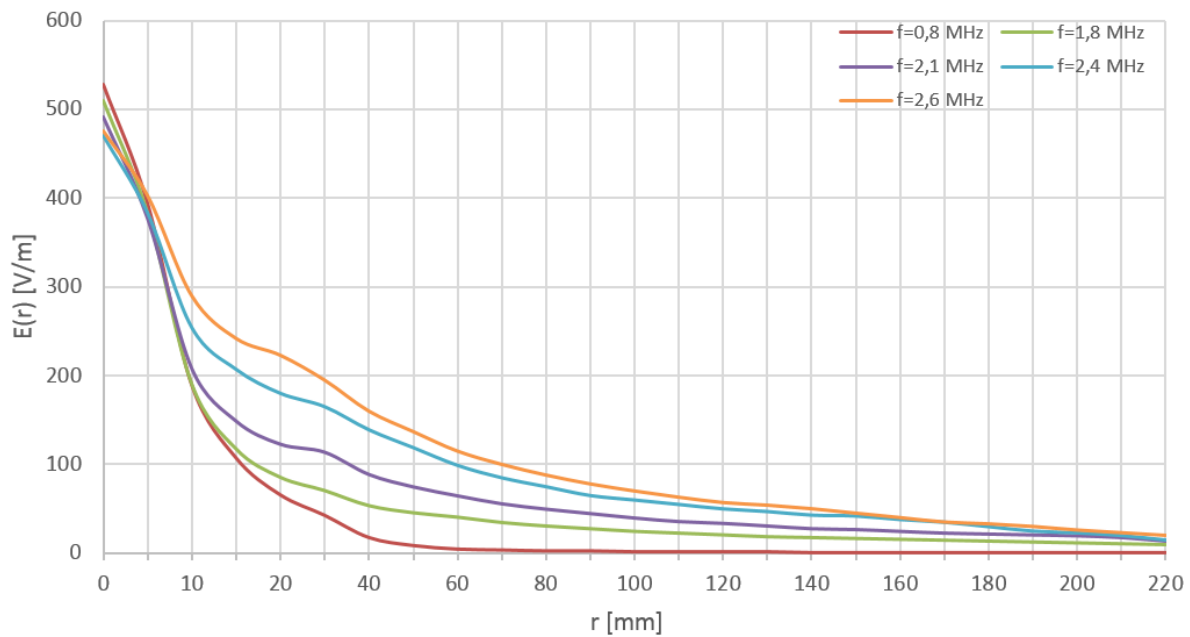


Figure 3.8 – Electric field over the distance of the antenna in vacuum.

As one would expect from a monopole in vacuum, the radiation pattern is completely symmetrical, creating a doughnut-shape like pattern, with each minimum located on the tips of the antenna (front and rear). Regarding the reflection coefficient, as stated before, the antenna is not naturally resonant at the projected 2.4 GHz frequency band for Wi-Fi and Bluetooth. Finally and already stated, but of great importance, is the difference between the regularity of the far field and the instability of the near field which can be perceived in Figure 3.8.

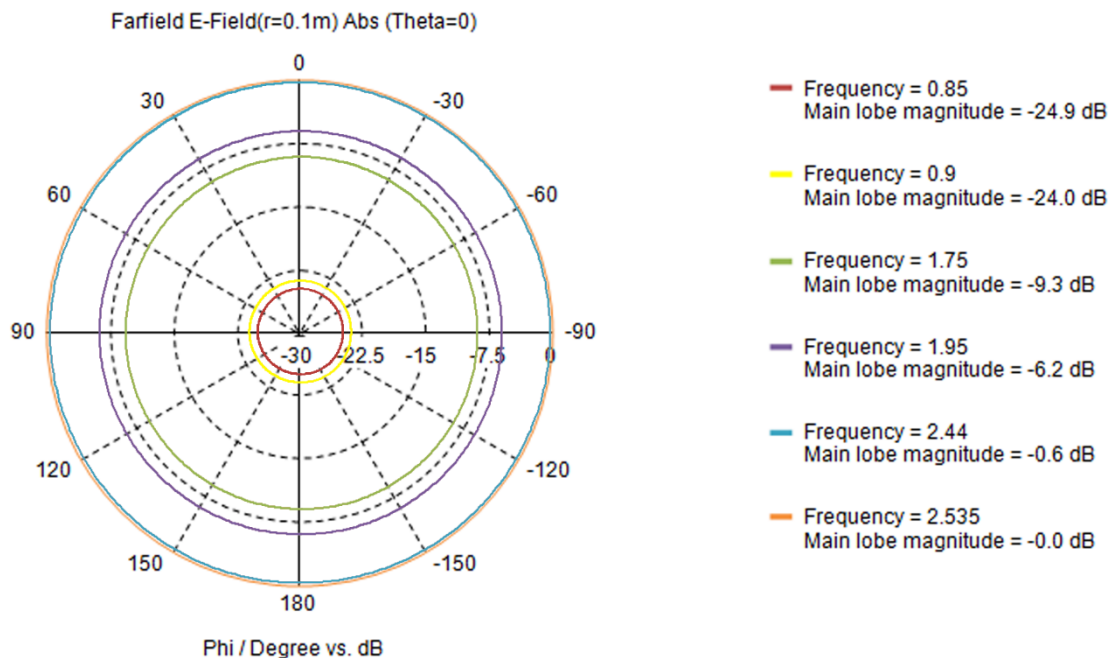


Figure 3.9 – Front cut plane of antenna's radiation pattern in vacuum, for different frequency bands.

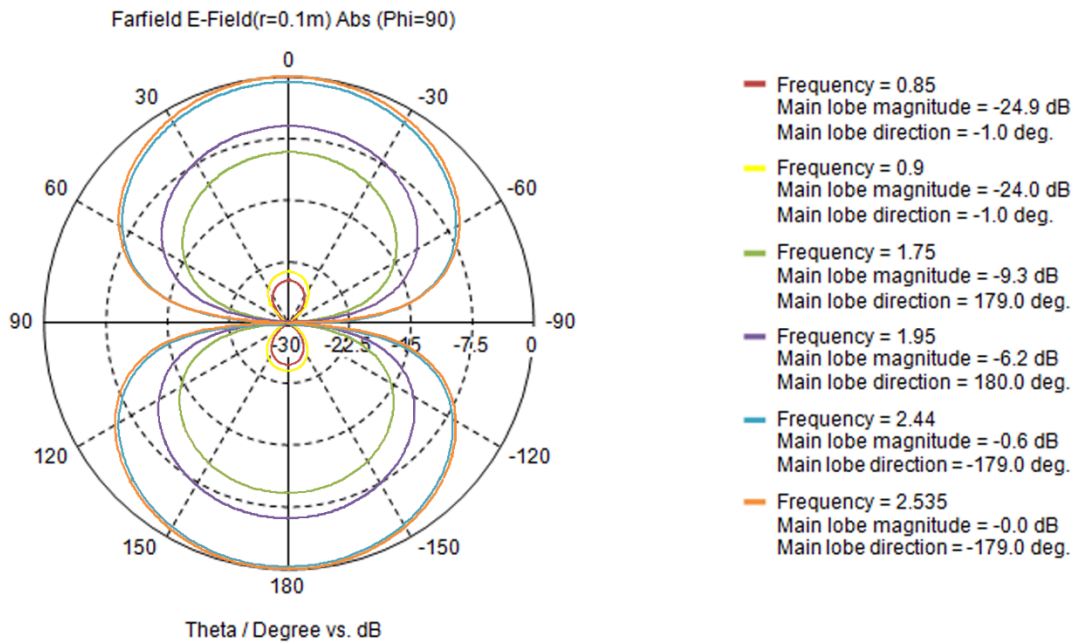


Figure 3.10 – Lateral cut plane of antenna's radiation pattern in vacuum, for different frequency bands.

3.4 Modelling of *Glass*

Regarding the *Google Glass* model, the one used in the simulations is slightly different from the real one when it comes to dimensions. This model was obtained in [CAD14], where it was available for public download and use, initially designed in a 1:1 scale and with its entire exoskeleton correctly built, providing an easy assignment of materials in *CST* for each part. Although all these features were correct, this model wouldn't fit the voxel model, so a rescale had to be done. The *Google Glass* model used in simulations can be described as 1.2 times wider than the original one, although the materials remained the same. With the exception of the metal frame surrounding the forehead, the entire model is built in plastic, so in the simulator the material assigned was Teflon. For the metallic frame, the material used in the simulation is titanium, the same metal present on the real prototype.

Figure 3.11 shows the *Glass* and how the model was before being changed, where it is visible in grey the titanium frame, while the material in white is simply plastic. Again, details on the physical properties of these materials can be seen in Annex C. In Figures 3.12 and 3.13, the *Glass* modelled in *CST* can be seen in different perspectives.



Figure 3.11 - Original *Glass* before being moulded to fit the voxel model, with reference ruler in inches (extracted from [FCC14a]).

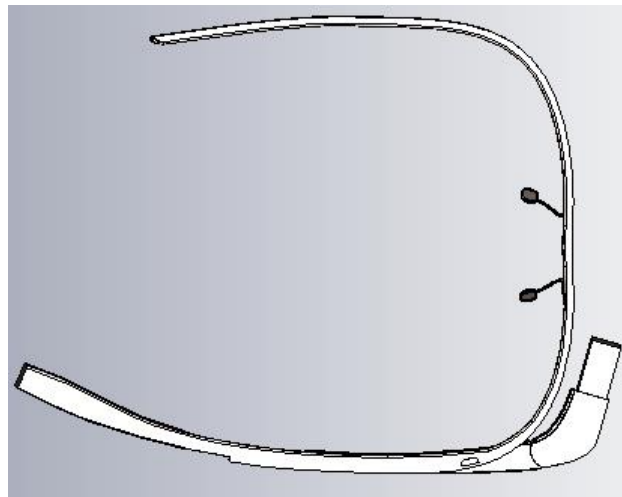


Figure 3.12 – Top view of *Glass* model used in CST.

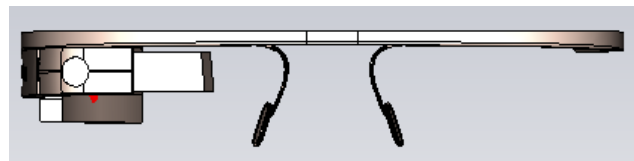


Figure 3.13 – Front view of *Glass* model used in CST.

An assessment of the *Glass*'s influence on the antenna's radiated wave was also made. One would expect that no significant losses or any type of distortion occur, since the materials used in the prototype (and also in the simulations) are only Teflon and the titanium alloy, with the second being a paramagnetic material and a poor electrical conductor, i.e., assuming that copper has 100% conductivity, titanium has only 3.1%, 1.8476×10^6 S/m.

In both Figure 3.14 and Figure 3.16 the location of the antenna on the *Glass* prototype is visible, while Figure 3.15 shows the cut plane with the location of the antenna placed inside the model to be used in CST. As seen in Figure 3.14, the boundary between the *Glass* and the voxel model is around [6.5, 7] mm, since the distance from the antenna to the prototype's edge is 6.2 mm, and one has to

account also with the *Glass*'s material thickness.

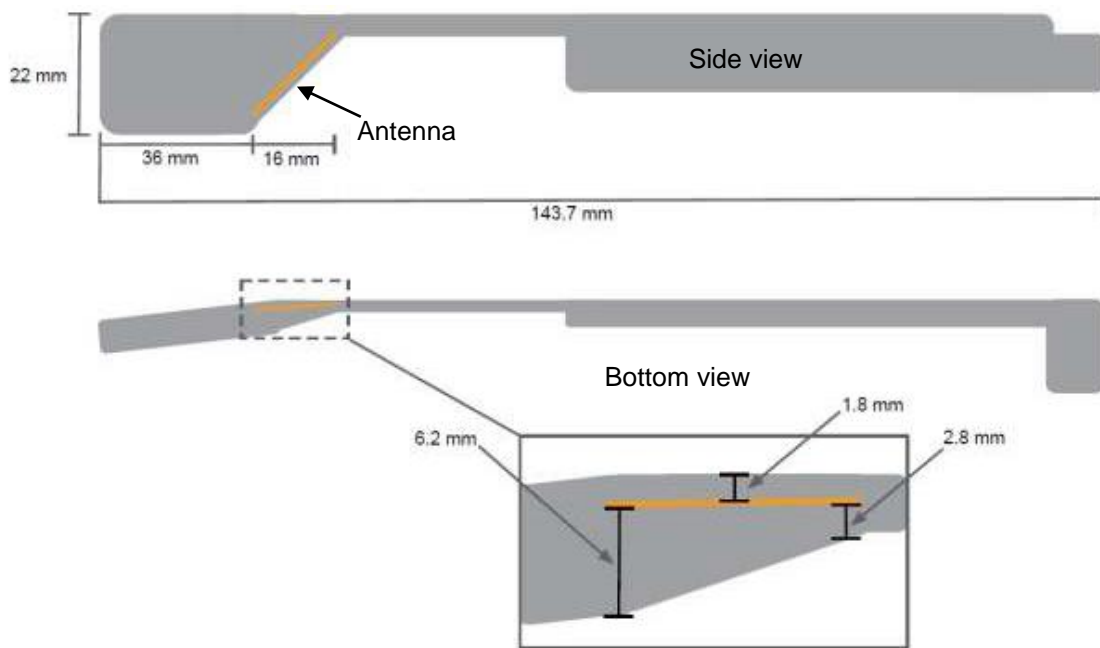


Figure 3.14 – Schematic for side and bottom view of the *Glass*, with the antenna's location and dimensions (extracted from FCC14a).

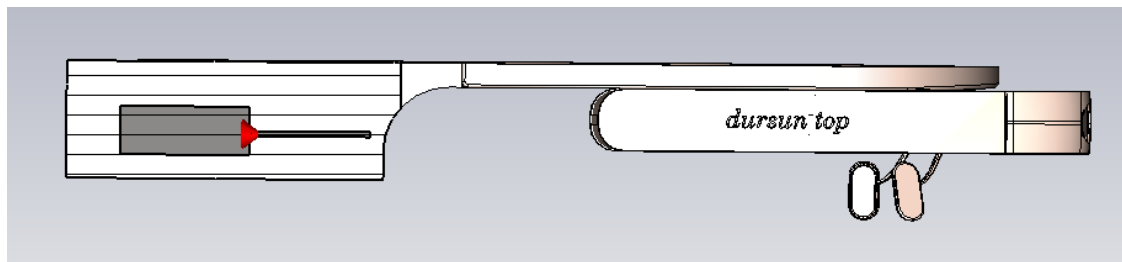


Figure 3.15 – Cut plane of side view of *Glass*, showing the location of the antenna on CST.

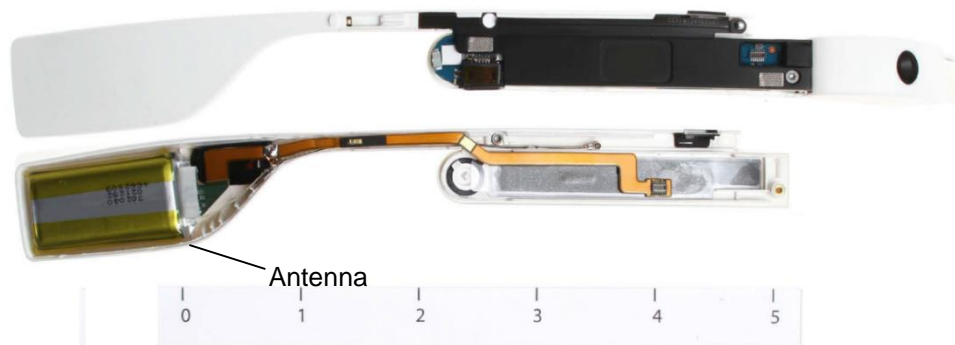


Figure 3.16 – Side view of *Glass* prototype showing the location of the antenna, with reference ruler in inches (extracted from [FCC14b]).

In Figure 3.17, the evolution of the E-field over the distance is presented, now for the antenna placed in the *Glass* model, and finally in Figure 3.19 and Figure 3.20, the main lobes of the E-field are presented. In order to get a better perception on the location of both the antenna and the *Glass*, Figure 3.18 shows

the axis and coordinates used for the charts of the E-field's assessment.

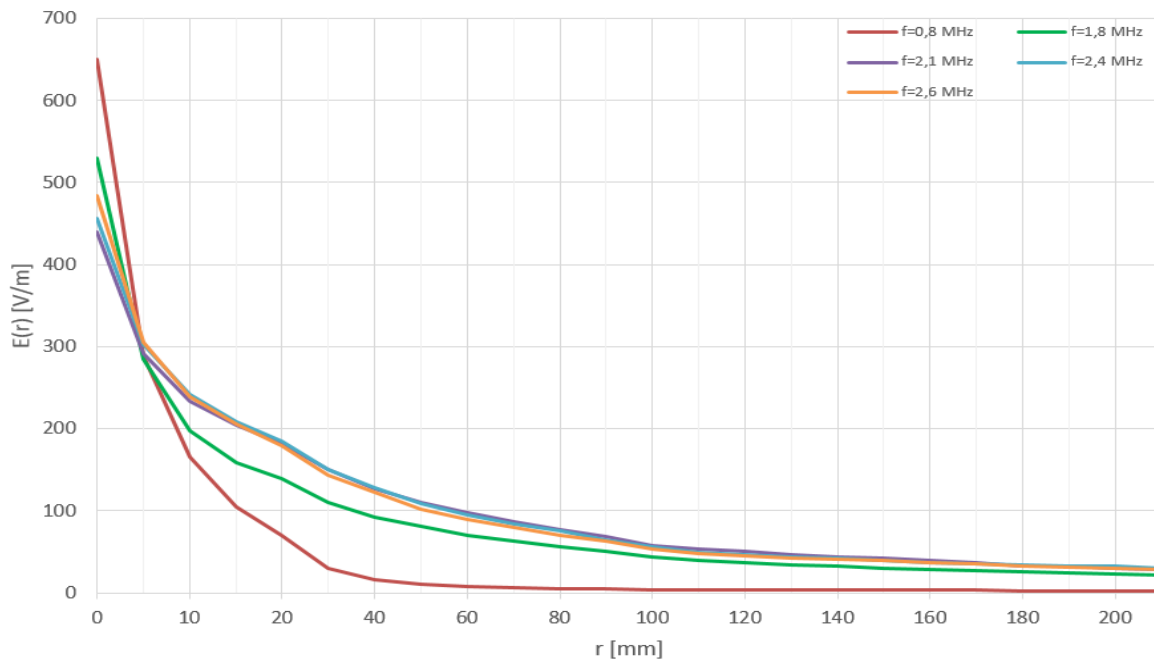


Figure 3.17 – Electric field over the distance of the antenna equipped within the *Glass*.

Again, in Annex D, one can obtain further information on the electric field behaviour, such as its maximum value in linear units and the 3D view of the radiation pattern.

As one would expect, only for low frequencies does the *Glass* causes any disruption on the radiation pattern, and only in the direction to the interior of the model. Regarding the magnitude of the electric field over distance, the *Glass* shows little effect comparing to the antenna in vacuum.

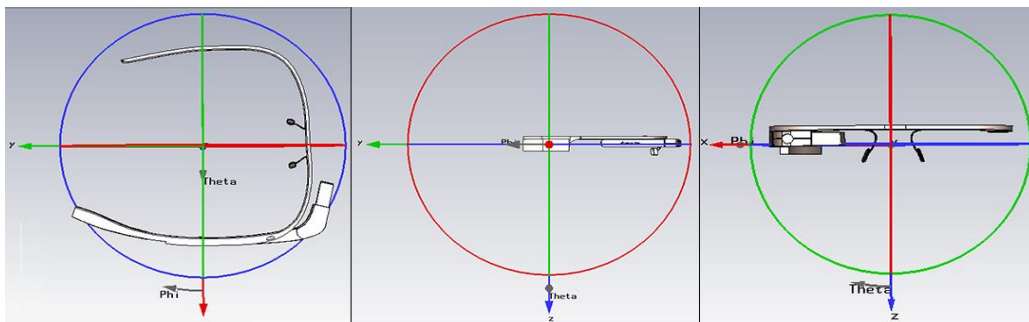


Figure 3.18 – Different perspectives of the *Glass* with axis and coordinates represented.

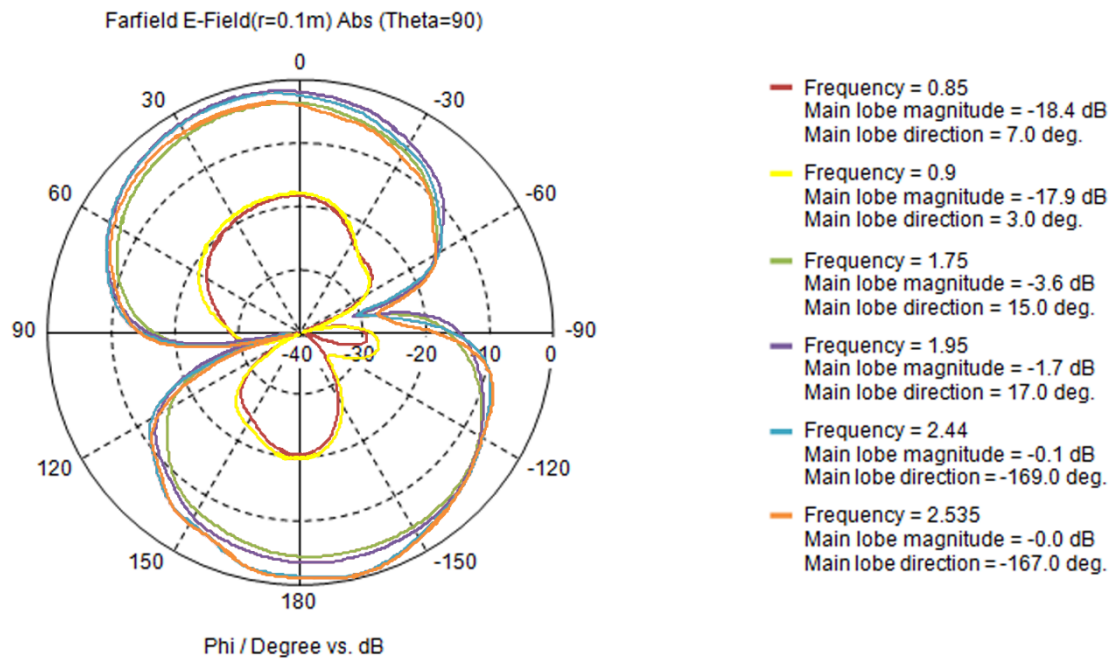


Figure 3.19 – Top cut plane of radiation pattern from antenna inside the *Glass* model.

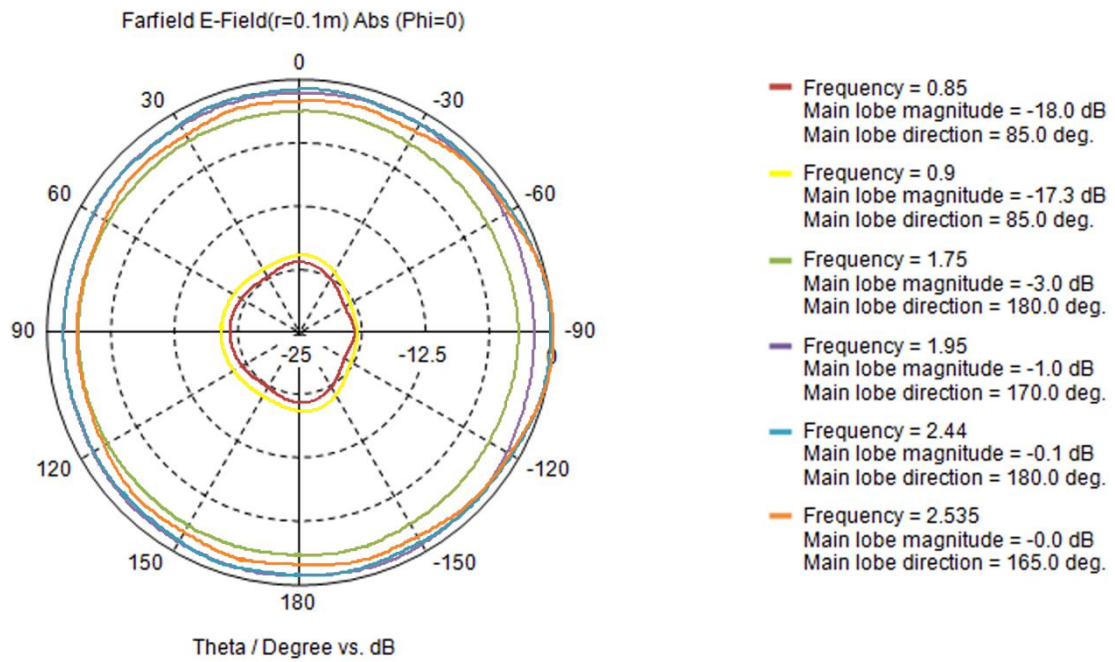


Figure 3.20 – Front cut plane of radiation pattern from antenna inside the *Glass* model.

3.5 Modelling of Voxel Head

The voxel model was designed in a 1:1 scale and it can be split into several layers, each one corresponding to a certain material such as brain, muscle, bone (skull), skin, etc. A full list with the

materials belonging to this model can be found in Annex C, each one with its specific properties. For SAR reading purposes, the most important properties are the permittivity of the tissue, its electrical and thermal conductivity and obviously the amount of volume absorbing the radiation. The voxel in use has a total volume of 4.789 dm^3 , with a total weight of 5.238 kg , composed of materials of different densities as stated before, and which can be seen in Figure 3.21. In Figure 3.22, two different perspectives of this model can be seen in order to better assess its dimensions. The height, width and length, respectively denoted in the image as H , W_i and L , are 22.4 cm , 23 cm and 19 cm , also respectively. In Table 3.3 these dimensions are detailed.

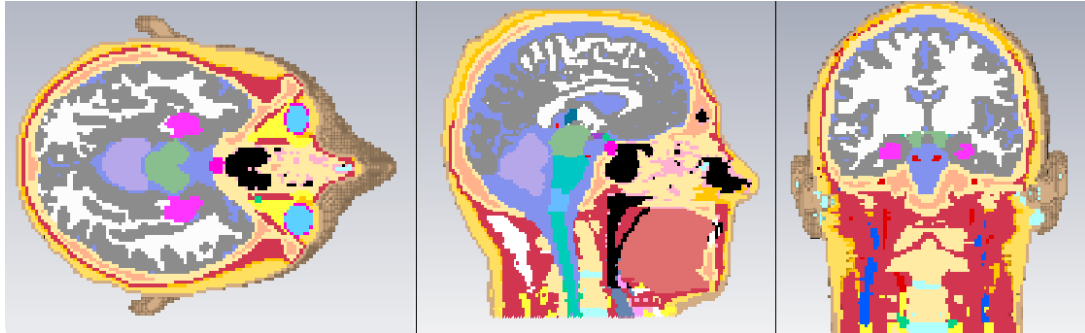


Figure 3.21 – In order, top, side and front perspectives of the voxel model used in *CST*.

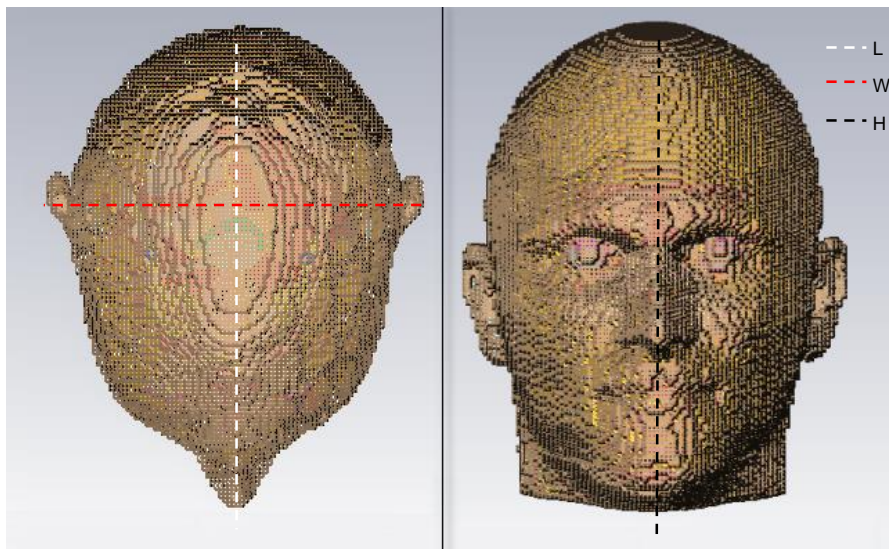


Figure 3.22 - Different perspectives of the Voxel model used in simulations.

A final assessment of the voxel model's properties regarding its influence on the electric field had to be made. In order to achieve this analysis, a plane wave was set to pass through the head model in the same direction and from the same origin point where the antenna would be placed, i.e., from the voxel model's right to left side. The collected parameters were the same as the ones taken before when assessing the antenna and the *Glass* model.

In order to have a better perception of the results, Figure 3.23 represents the coordinates being used and the direction the voxel model is facing. This is also the reference to be taken into account when it comes to the final results presented henceforth in this work.

Table 3.3 - Dimensions of the voxel model in CST

Height [cm]	Width [cm]	Length [cm]	Volume [dm ³]	Weight [kg]
22	15	23	4.789	5.238

In both Figure 3.24 and Figure 3.25, one can see the low influence and disruption the voxel head causes in the incident plane wave, on the various frequencies. Since the analysis made for the voxel head was through an incident plane wave and not the designed antenna, in order to assess the interference on the wave form by the voxel, it has no interest to show the values in linear units in an annex.

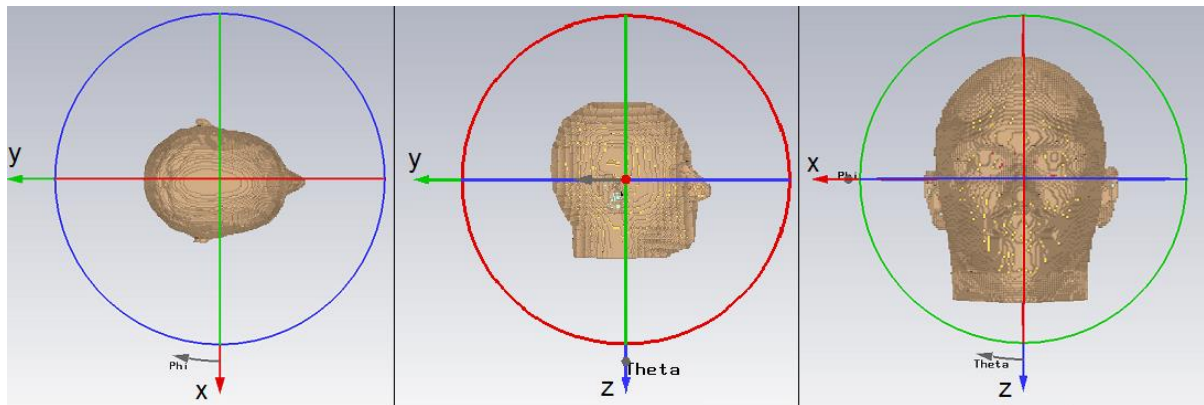


Figure 3.23 - Top, side and front perspectives of the model with its coordinates' axis.

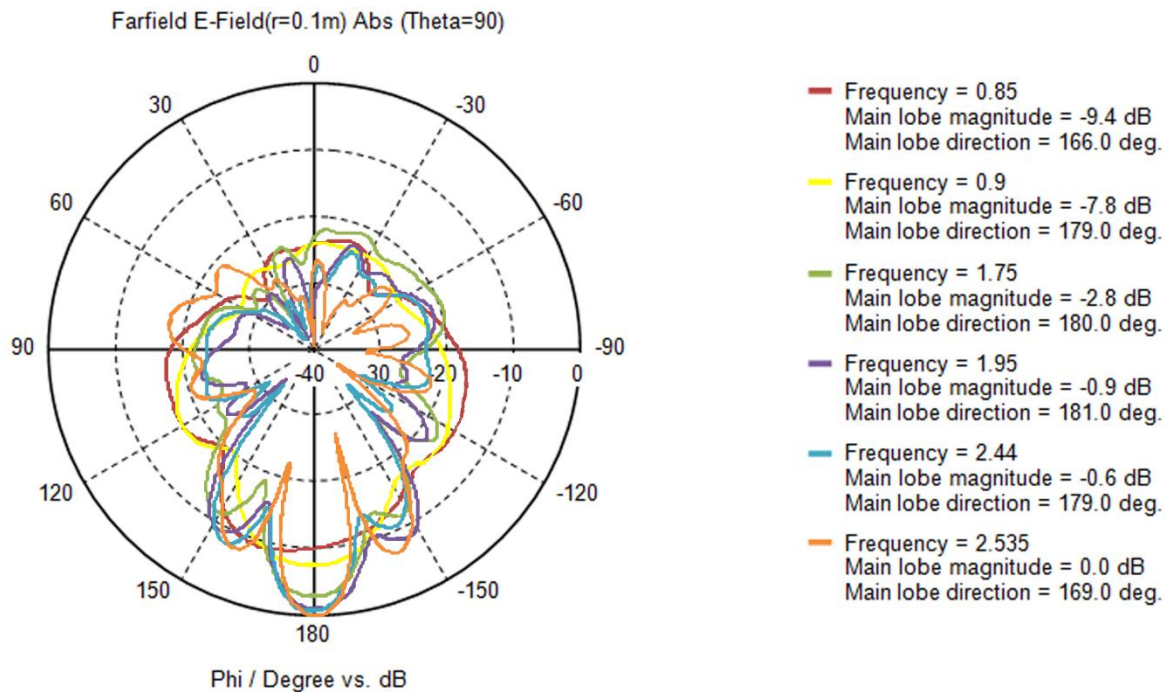


Figure 3.24 – Front cut plane of the radiation pattern from incident plane wave on the voxel model.

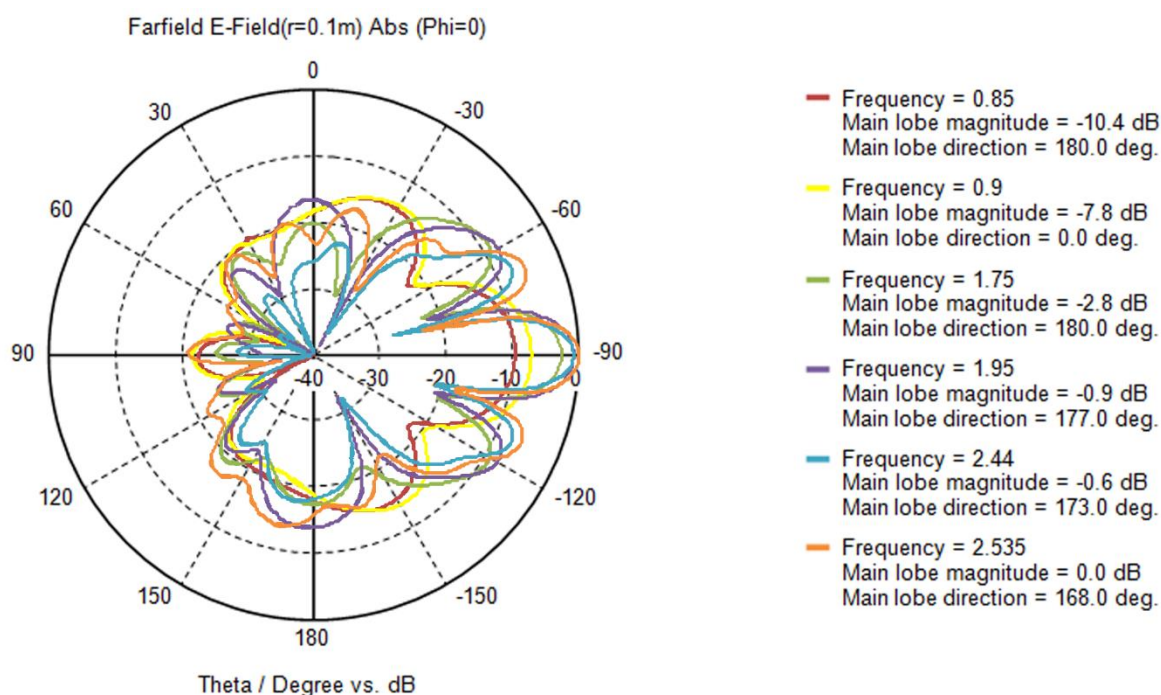


Figure 3.25 – Top cut plane of the radiation pattern from incident plane wave on the voxel model.

3.6 Mesh Cell and Simulation Load

The mesh cell to be used is the hexahedral adaptive mesh cell. As stated before, after the setup of the model is done and the appropriate power sources and boundary conditions have been made, the model has to be translated into a computer accessible format. The calculation domain has to be subdivided into small cells on which Maxwell's Grid Equations are solved. This mesh influences the accuracy and speed of the simulation as well as the load it puts on the computer and the resources it needs to run. In other terms, the denser the mesh is, the more accurate it gets but it also takes longer to calculate. Also, a bigger number of cells is needed for a more complex structure or element.

In Figures 3.26 and 3.27, that difference can be better perceived, where in the first, for the antenna alone, the mesh is much less denser than for the second, where the voxel model is present. The fewer number of cells is also visible where no element is present and where less calculations are needed. While in the antenna alone the mesh cell contains around 700,000 cells, in the voxel model, that number surpasses 8,000,000. For the final step of the simulation, with all the elements together (voxel, *Glass* and antenna model), the simulator required a mesh with over 42,000,000 cells to achieve the results and ran for 2.5 hours, excluding auxiliary simulations (such as the calculation of SAR, that derives from the calculation of the power loss density). In terms of required computing resources, the software allocated up to 6.5 Gbit of memory for itself, ran with 2 simultaneous threads and used the entire processor power to execute simulations. It was also noted that the program was always trying to allocate more memory, although that was not possible as no more RAM was available in the used hardware.

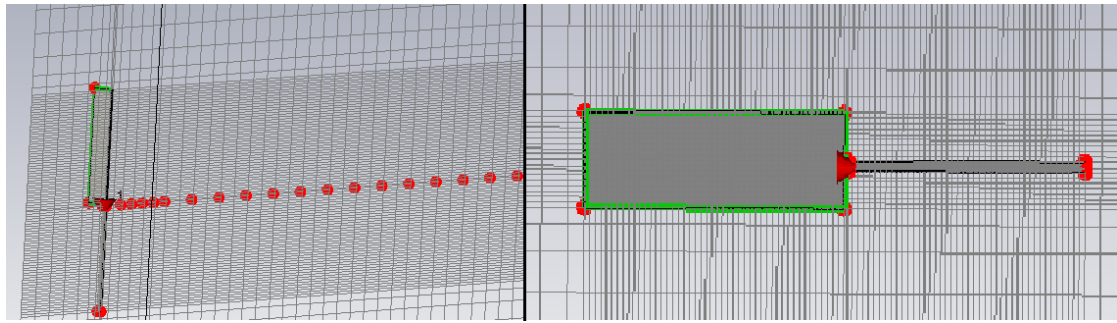


Figure 3.26 – Perspective with probes (red dots) and side view of the antenna with mesh cell visible.

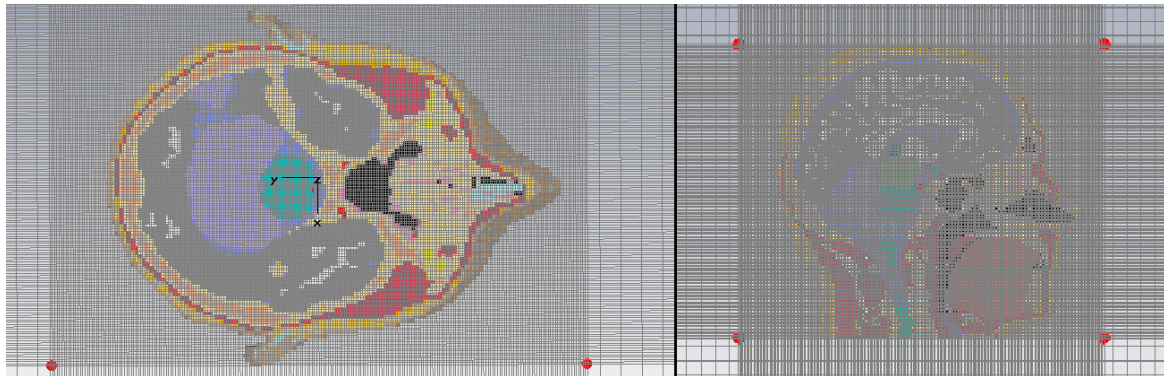


Figure 3.27 – Top and side view of the voxel model with respective mesh cell visible

It has to be taken into account the fact that the hardware used was a laptop equipped with 8 Gbit of RAM and an *Intel Core i5-3210M CPU* with 2.50 GHz of clock speed. Also, no kind of hardware acceleration was used to aid in the simulations speed (such as the use of a GPU).

Since the software chosen is a commercial one and also calibrated, while at the same time very well known in the scientific community for its accurate results, there was no need to make an assessment on the output values given by it.

Chapter 4

Result Analysis

In this chapter, the considered scenarios are defined, followed by the description of the calculation procedure, as well as the results obtained.

4.1 Scenario description

The analysis is done by considering one reference scenario and then varying the parameters of interest regarding this scenario, in order to assess their influence. In order to test the exposure of a human being to a source of high frequency non-ionising radiation, the prototype chosen was the model created by *Google*, known as *Glass*, as seen in Figure 4.1. This equipment is originally built without cellular capacity, only carrying Wi-Fi and Bluetooth modules, although for this work, the antenna in use will also be working in the frequency bands of GSM, UMTS and LTE, in order to get the results desired.

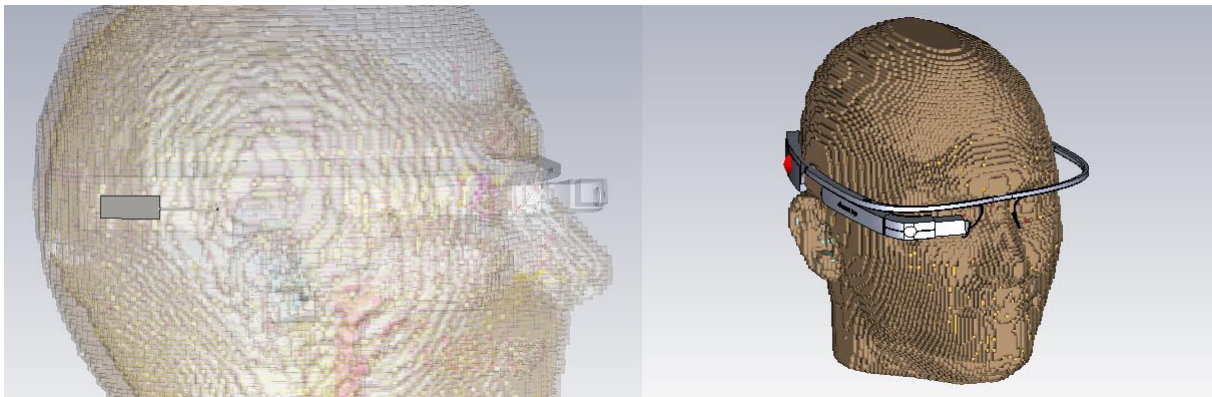


Figure 4.1 - Voxel model, together with the model of *Glass* and the antenna.

The considered scenario is a controlled environment, where the equipment to be analysed is an antenna for mobile purposes, most specifically a quarter wavelength whip antenna, attached to a rectangular ground plane. The antenna is fed by a discrete port located between the ground plane and the antenna itself, transferring 1 W of power to the radiator, represented in Figure 4.2 as a red arrow.

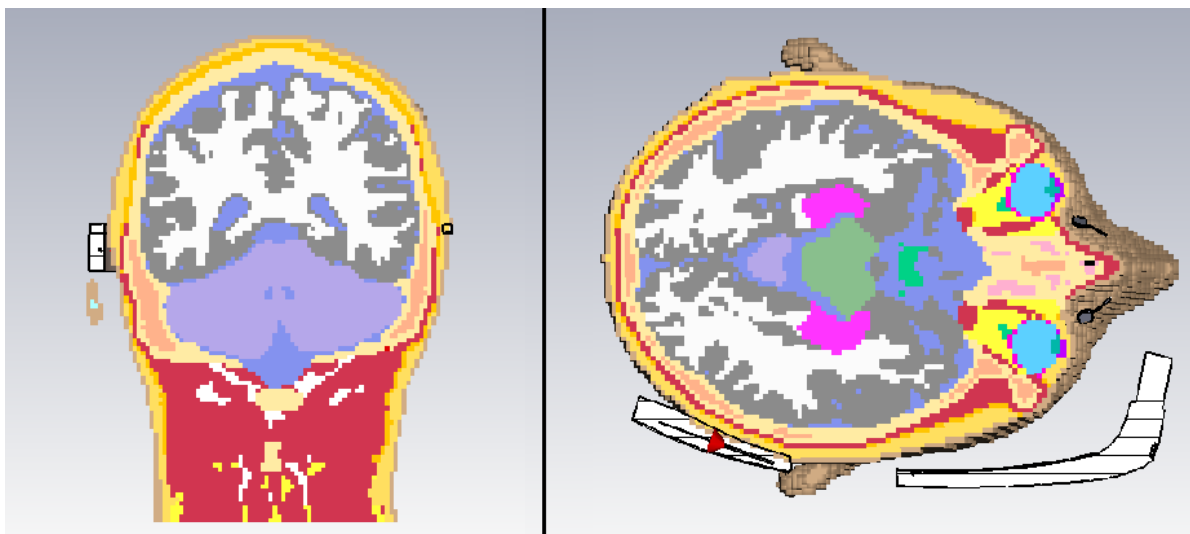


Figure 4.2 - Cut planes used for the simulations, with port visible as a red arrow.

The surrounding environment is characterised as free space. Although no thermal analysis is made, the initial background temperature is 273 K and the initial body temperature is 310 K.

The antenna is located on the right temple tip of the *Glass* prototype, which relative to the head makes it near the right tempura, slightly above and behind the right ear, as seen in Figures 4.1 and 4.2. Figure 4.2 also shows the cut planes to be used whenever an analysis in 2D is made, since the analysis in 3D only gives results for the outer layer of the voxel model. This cut plane is where the CST's mesh grid is located for it cuts the antenna in half, and also is where the feeding port is located. Furthermore, since the work is oriented to the worst case scenario regarding exposure to radiation, the cut plane location is where this criteria is met inside the voxel model volume.

Table 4.1 shows the systems to be tested and their main frequency bands, thus defining the range of frequencies in analysis for this work. The frequencies to be simulated and analysed are the central ones of the UL band of each system. At this stage, the assessment of the antenna and the influence it suffers from the *Glass* prototype has already been tested in the last chapter, along with the effects of the voxel model on a radio wave, only remaining the global analysis of all the elements together (antenna, *Glass* and voxel) and a final comparison of the results.

Table 4.1 - The different technologies and their main frequencies bands for the desired scenario.

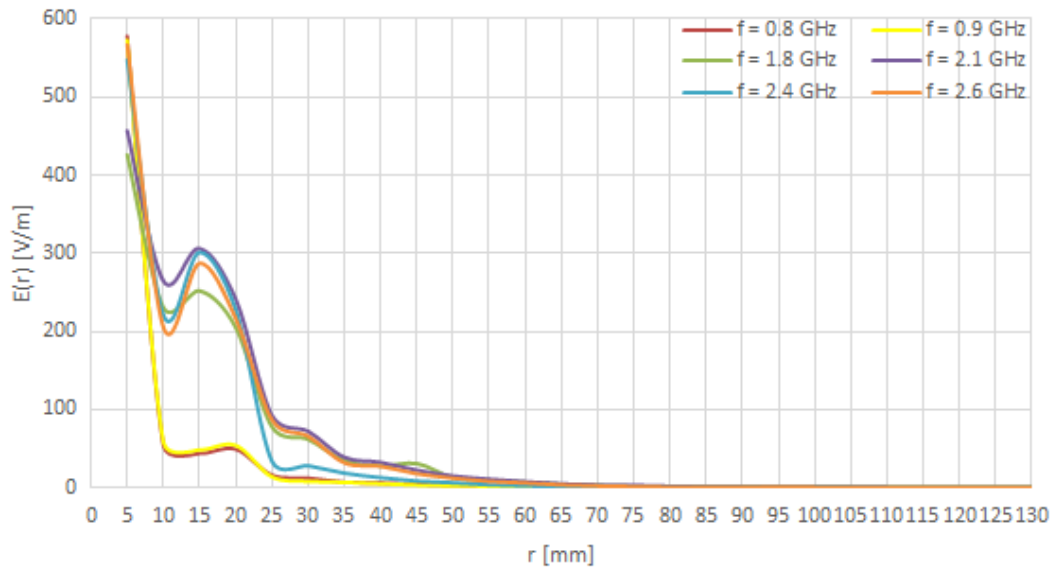
Technology	Reference Frequency [MHz]	UL Frequency Range [MHz]	DL Frequency Range [MHz]	Simulated Frequency (central UL freq.) [MHz]
GSM	900	880.0 – 915.0	925.0 – 960.0	900
	1800	1710.2 – 1784.8	1805.2 – 1879.8	1750
UMTS	900	880.0 – 915.0	925.0 – 960.0	900
	2100	1920.0 – 1980.0	2110.0 – 2170.0	1950
LTE	800	832 – 862	791 - 821	850
	1800	1710 - 1785	1805 -1880	1750
	2600	2500 - 2570	2620 - 2690	2535
Wi-Fi	2400	2412 - 2472		2440

4.2 Radiation Pattern and Electric Field

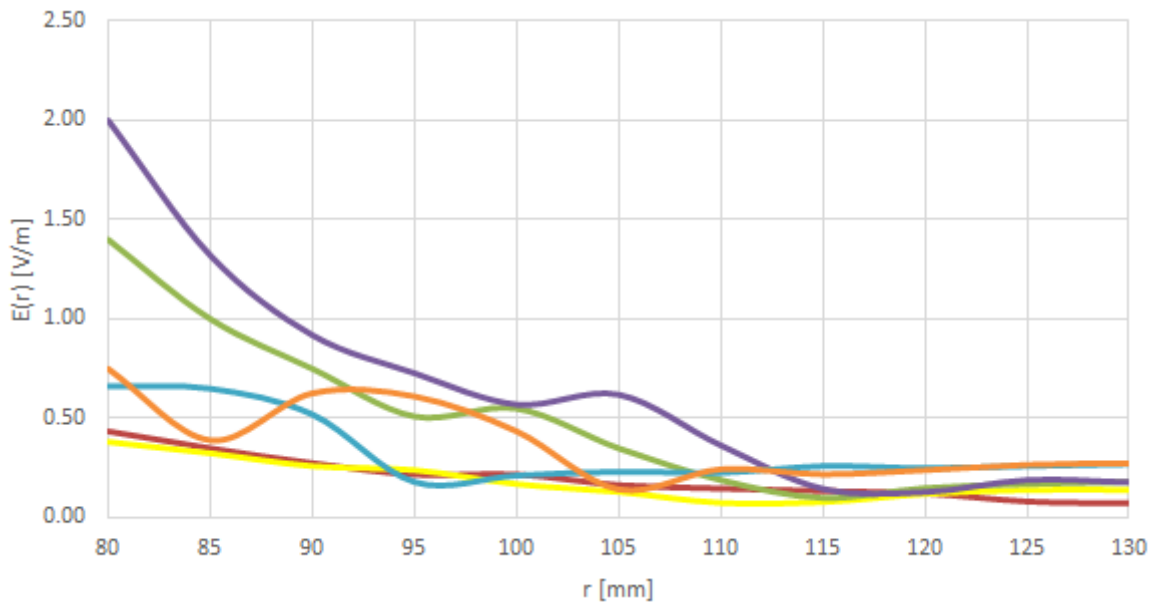
The calculations were performed for the scenarios presented above, maintaining the same input parameters each scenario. The readings were obtained with the far field monitor in broadband mode to get a faster reading on the entire frequency range desired. When comparing these results with the ones in Chapter 3 (the assessment of the different components individually), one manages to have a clear view on the influence imposed by the voxel model on the radiated wave, and vice-versa.

This part of the work starts with the evaluation of the electric's field strength over the distance, represented in Figure 4.3, with the antenna as the origin of the chart. Reminding that the voxel model

outer layer is located at ~ 7 mm from the antenna, one can see, by comparing with Figure 3.17, the difference between the human tissue and the plastic from the *Glass*, regarding its influence on the wave, with high deterioration of the signal's strength. Also, and taking into account that the layer simulating the human skull is around 6.5 mm thick, the different tissues composing the human head are visible, each with its own permittivity and electrical conductivity.



(a) – Entire distance.



(b) – Further distance amplified.

Figure 4.3 – Evolution of electric field over distance towards the centre of the head, amplified for farther distances.

In terms of the different frequencies under analysis, one can see that the higher ones are most affected, in Figure 3.7, the reflection coefficient (in dB) is almost null for the frequency bands of 0.8 GHz and 0.9 GHz. These two bands are the bands with lowest magnitude and with best linear behaviour, although at very close range, they are the ones presenting the highest magnitudes. For this antenna, for lower

frequencies, the maximum penetration achieved by the E-field can be considered in the range [60, 70] mm, since at this depth the magnitude is lower than 2 V/m, negligible in terms of exposure. For higher frequencies, the penetration can be higher. For farther distances, one can still note the different behaviour each frequency has when it reaches different materials or layers, and the irregularity it has on the propagated wave.

In Figure 4.4 and Figure 4.5, following the reference shown in Figure 3.23 for a better perception, the effect and the absorption suffered by the voxel model in the wave emitting from the antenna are visible.

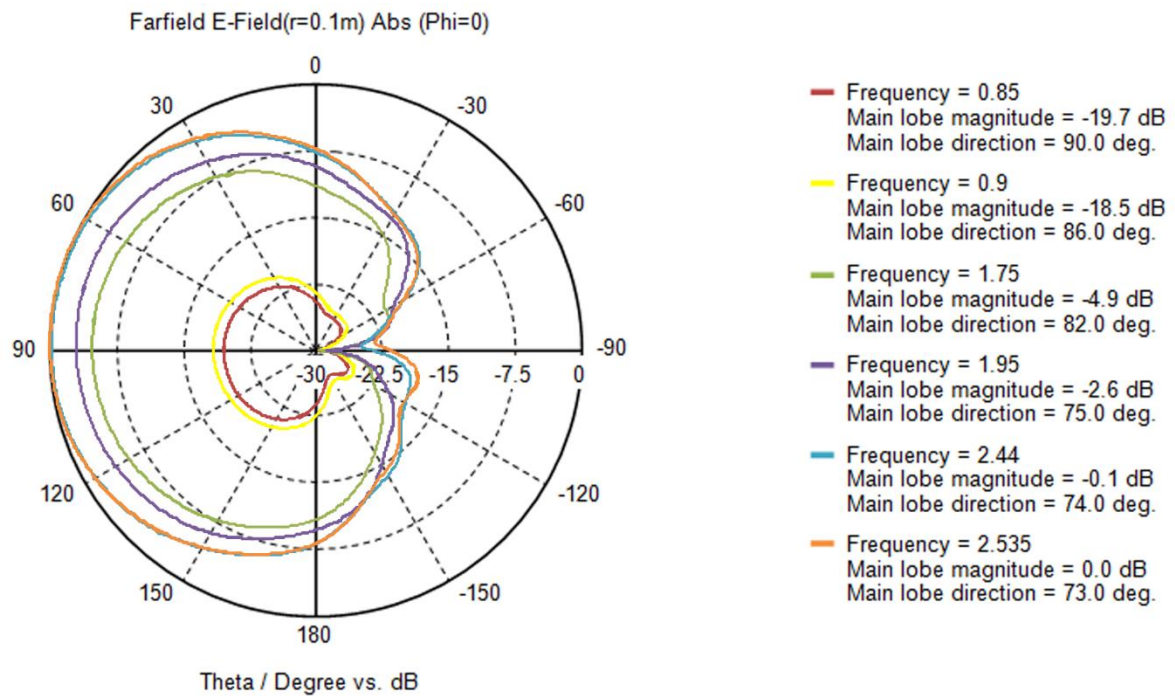


Figure 4.4 – Top cut plane of the radiated pattern while in the *Glass* and on the voxel

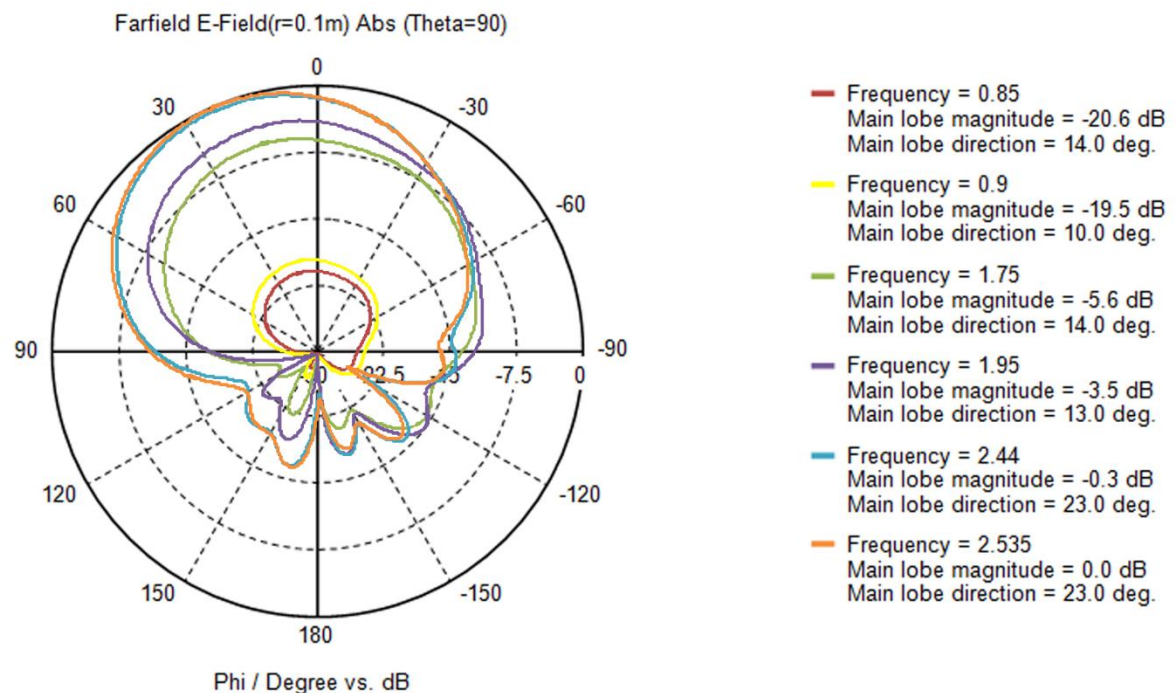


Figure 4.5 – Front cut plane of the radiated pattern while in the *Glass* and on the voxel

While away from the voxel model the wave has a pattern similar to the one when the antenna is only present in vacuum, i.e., almost a perfect pattern with no noticeable obstacles, on the opposite side, in the direction of the voxel head, the interference suffered due to the presence of the model almost nullifies the magnitude of the wave.

As in the previous analyses, more details regarding results, including the top magnitudes in linear units and 3D perspectives of the radiation pattern, are available in annex E.

4.3 SAR evaluation

The core evaluation of this work, SAR, is analysed and evaluated in this section. When feeding the antenna with 1 W of power, the peak power a mobile phone or a smart phone can use, all results are far beyond the allowed by European or American regulations.

In order to have some comparison terms on the real antenna used in *Glass*, it was decided to initially simulate it in the same conditions as those used when the prototype was under evaluation by the FCC. In the evaluation report, [FCC14c], it is stated that the maximum SAR value achieved by the *Glass* prototype was 1.42 W/kg averaged over 1g of tissue, which puts it under the limit of 1.6 W/kg in the USA. Along with these results, the reports also show that the maximum power fed to the antenna on these evaluations were 15 dBm (32 mW) while working in Wi-Fi technology and 9.7 dBm (9.33 mW) while working in Low Energy Bluetooth (LEBT). The results given by the simulator for the same parameters are shown in Table 4.2, along with the values observed with the analysis made over an average of 10 g of tissue. In annex, further information is provided about the output power over different channels on Wi-Fi and LEBT, extracted from [FCC14c].

In Table 4.3, the results are show numerically, while in Figures 4.6 to Figure 4.8 one presents the 3D and 2D perspectives with the range and degree of absorption of radiation on the voxel model. Although the simulations were made with all the components together, for these figures the antenna and the *Glass* model were hidden so to have a better perception and for an easier reading of the values obtained.

Table 4.2 – SAR results from CST, simulating *Glass*'s evaluation by the FCC.

Freq. Band [GHz]	0.8	0.9	1.8	2.1	2.4	2.6	Recommendation
ICNIRP standard (10 g) [W/Kg]	0.89	0.84	0.59	0.64	0.68	0.66	2.00
FCC standard (1 g) [W/Kg]	4.61	4.22	1.57	1.44	1.46	1.41	1.60
Official <i>Glass</i> SAR report (1 g) [W/Kg]	-	-	-	-	1.42	-	-

As stated before, the standard values of SAR are measured for 1 g of tissue or 10 g of tissue, the 10 g being the most common choice, and also the one used on Europe regulations. Thus, since ICNIRP's regulation states that the maximum SAR allowed for a mobile device is 2.00 W/Kg over 10 g of tissue, this work is based on this standard for further analysis on the topic.

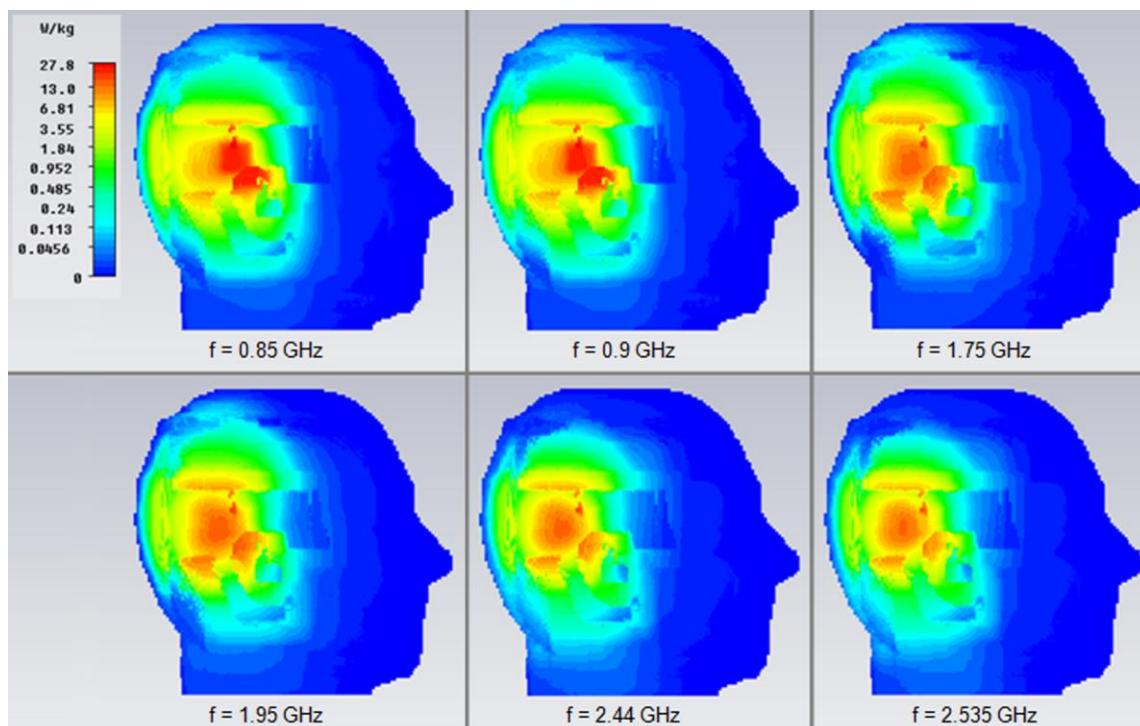


Figure 4.6 – 3D side view of the SAR range and amplitude on the voxel model.

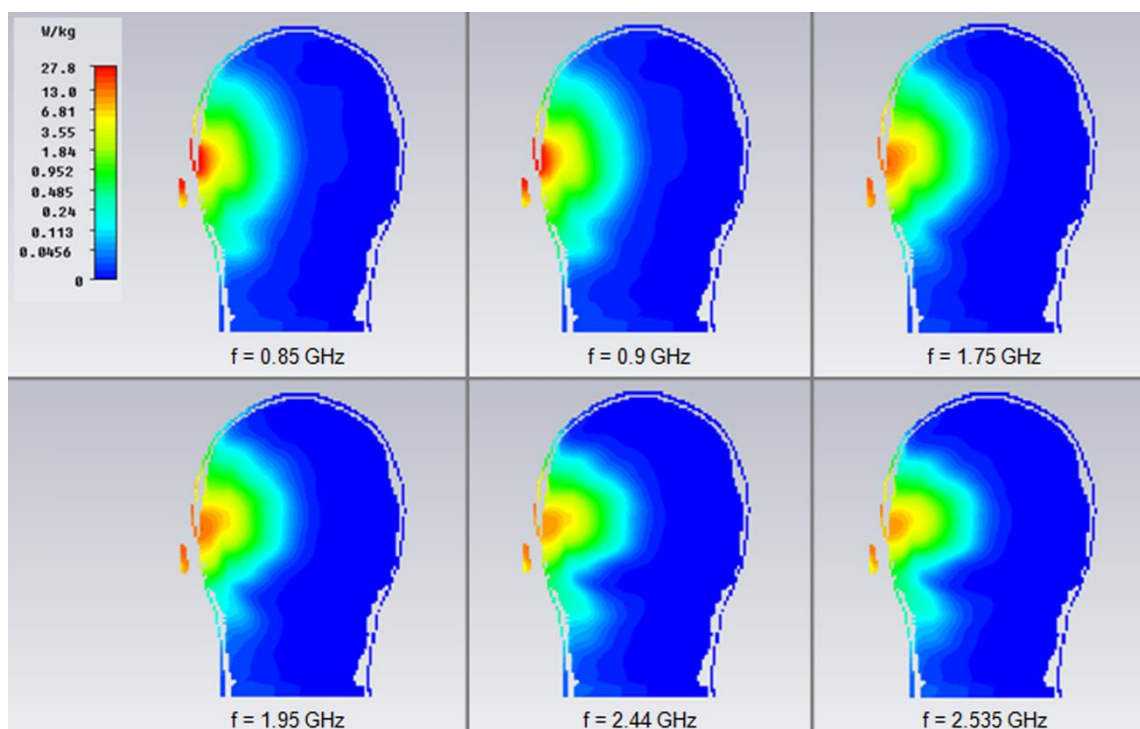


Figure 4.7 – 2D front cut plane view of the SAR range and amplitude on the voxel model.

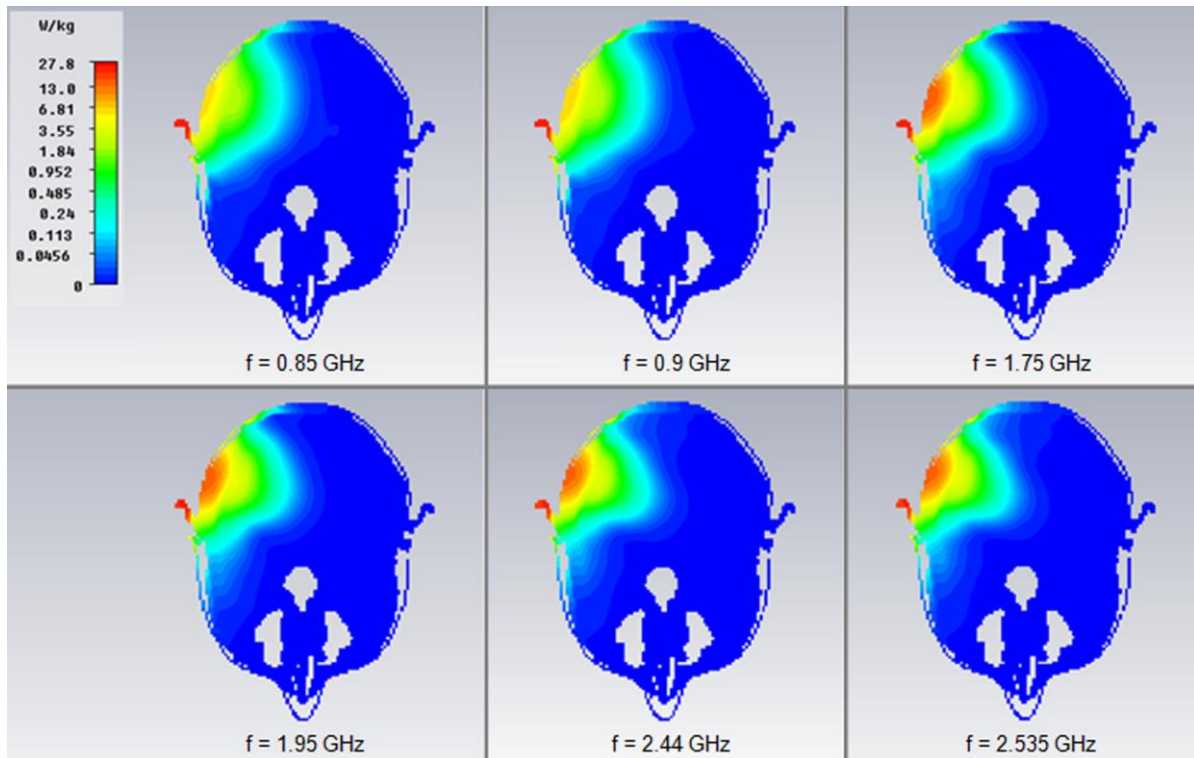


Figure 4.8 - 2D top cut plane view of the SAR range and amplitude on the voxel model.

Furthermore, one can see the resemblance between the actual value registered in the official *Glass's* evaluation by the FCC, and the value obtained by the simulator.

Table 4.3 – Peak SAR readings on the voxel model at different frequencies for 1 W of power.

Freq. band [GHz]	0.8	0.9	1.8	2.1	2.4	2.6
SAR (10 g) [W/Kg]	27.73	26.19	18.47	20.05	21.09	20.59

For these results, and by comparing them to the previous ones and the information in annex regarding the behaviour and physical properties of each tissue by frequency, one can conclude that the lower frequencies tend to be more absorbed and therefore more likely to cause more tissue damage than the higher frequencies. It has also to be taken into account the fact that, for the same input power, the lower frequencies have a higher amplitude at shortest distances, reaching the voxel model with a wave more intense than the other frequency bands. This obviously leads to a higher SAR due to lower frequencies. It is also visible the penetration depth achieved by the wave, which correlates correctly to the Figure 4.3.

It is also curious to note that, although the lowest frequencies (0.8 and 0.9 GHz) have, by a large margin, the highest registered SAR values, those are also the same frequency bands that register the least penetration depth of the entire group. In other words, although registering the lowest penetration depth, the initial E-field's strength was high enough to achieve the highest SAR values.

4.4 Power evaluation

At this stage of the work, the objective is to adjust the power of the antenna to a maximum, so that SAR is equal to 2 W/kg, i.e., the maximum value allowed by ICNIRP. This means that the results for all different frequencies are the same, i.e., 2 W/kg. For the entire procedure, the simulation scale was left untouched, being the same as the scale for the maximum SAR value recorded among all previous readings. In Figure 4.9 to Figure 4.11 one shows the SAR readings for 2 W/kg on the voxel model, again in 3D and the different cut planes in 2D. Table 4.4 gives the maximum power level the antenna can work at for each frequency band.

Table 4.4 – Maximum power permitted at different frequencies to achieve the limit of 2 W/kg.

Freq. band [GHz]	0.8	0.9	1.8	2.1	2.4	2.6
Max. Power [W]	0.0723	0.0765	0.1063	0.1002	0.0950	0.0971

The process to calculate the theoretical maximum power was quite simple and only a few iterations needed to be made, due to the fact that the power feeding the antenna is directly proportional to the square of the electric field, which in turn is also directly proportional to the SAR value. This obviously makes the power directly proportional to recommended SAR, and since the SAR values for 1 W have already been simulated in the previous simulations, the calculations to get an approximate maximum power level was fairly easy and direct.

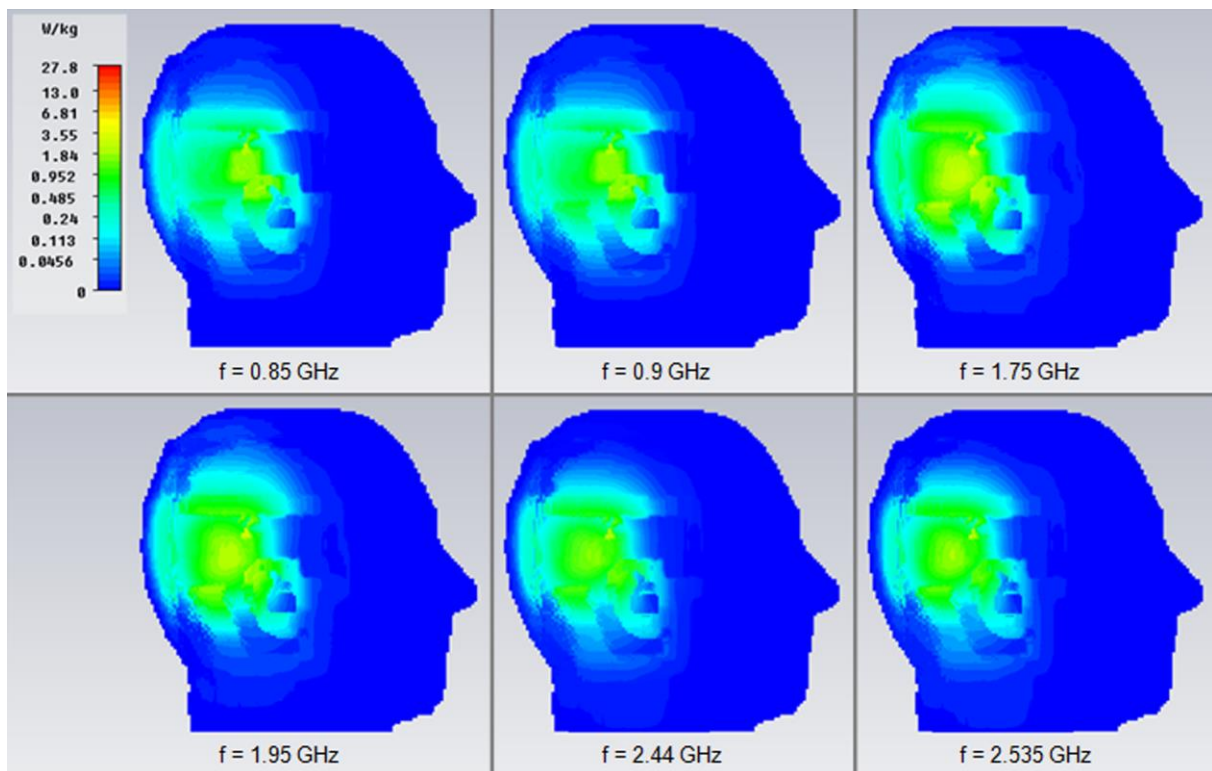


Figure 4.9 – 3D side view of the SAR range and amplitude on the voxel model.

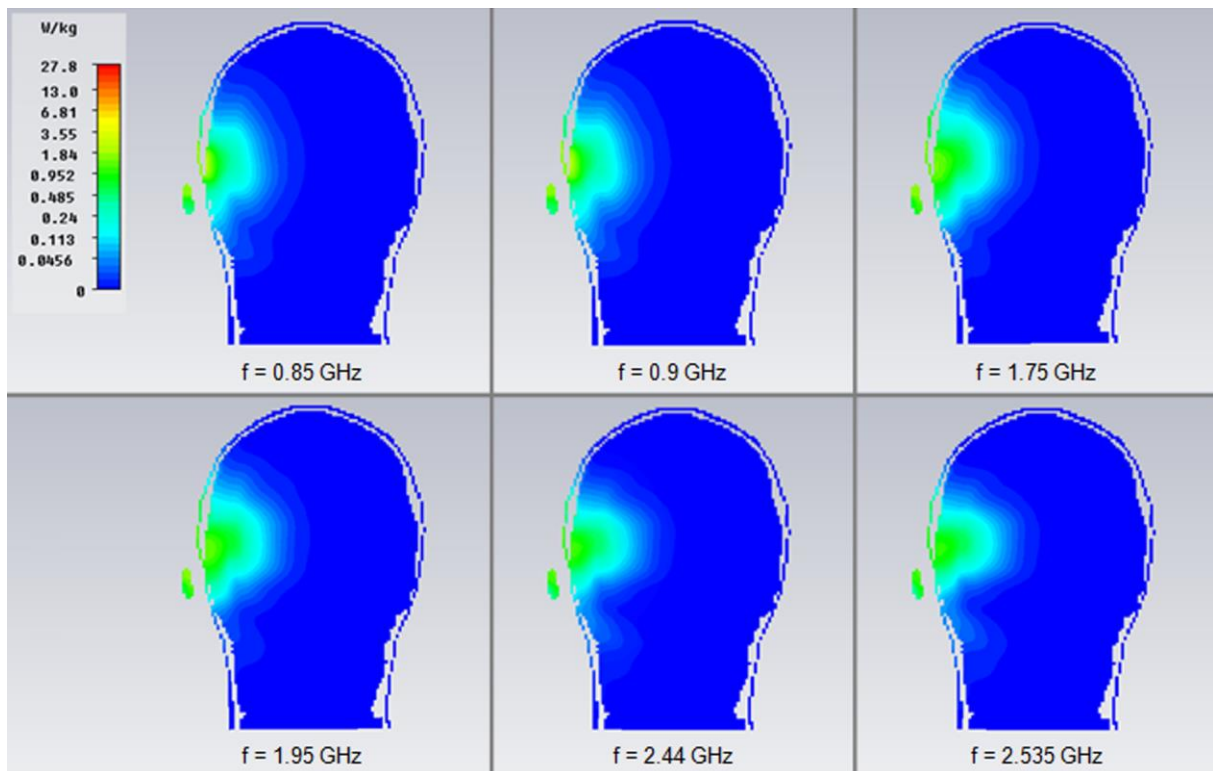


Figure 4.10 – 2D front cut plane view of the SAR range and amplitude on the voxel model.

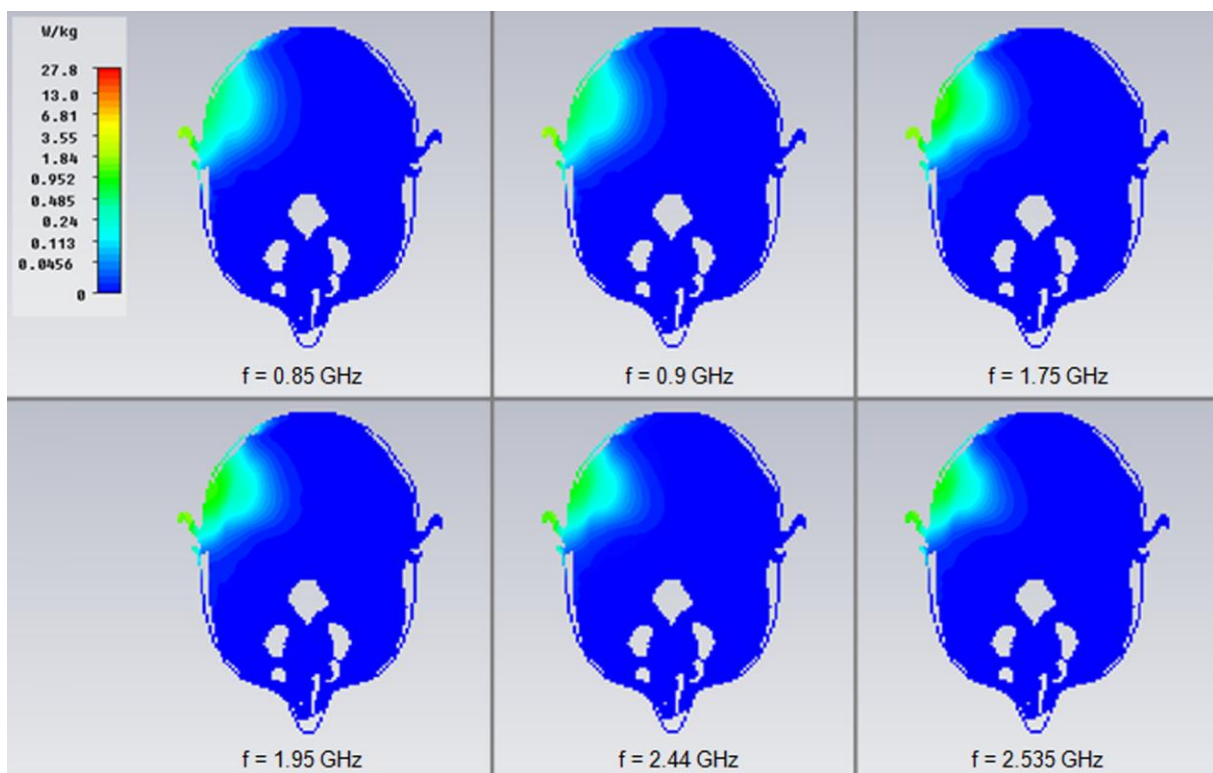


Figure 4.11 - 2D top cut plane view of the SAR range and amplitude on the voxel model.

As stated before, one of the main reasons for an MT to increase its output power is due to the increasing distance to the BS it is connected to, and thus the need to transmit more power to maintain the

connection. In other terms, and putting the latest results into context, one can say that it is possible to use this antenna with LTE at the higher frequency bands (1.8 and 2.6 GHz), while in an urban area with a dense cluster of pico-cells. Since the maximum value for an MT using LTE is 200 mW, which is close to double the values registered for both frequency bands limits, and the minimum being 0.1 mW, in a dense BS area, one could use the antenna with no risk of surpassing the recommended limit.

4.5 Antenna Length

For the final analysis of the antenna, the parameter to be changed is its length, and at which point it would benefit or harm the propagated signal. The objective is to model an antenna designed to communicate at the LTE frequency band, namely the 2.6 GHz one. In order to get a proper design, one started by using the theoretical value for this scenario, that is, a quarter of the wavelength corresponding to the desired frequency. This would mean an antenna length of 28.846 mm, since the wavelength corresponding to a signal at 2.6 GHz is 115.385 mm.

Although this would be correct, the dimension used in the simulations should be the one proportional to the real dimension of the antenna, i.e., directly proportional to the dimension used in the previous simulations. This is due to the fact that the real antenna's dimension is different from its theoretical values. In other terms, the antenna belonging to *Glass*, which works in the 2.4 GHz band, has a dimension of 22.9 mm, when the theoretical value of the length for an antenna at this frequency is 31.227 mm. All this can be seen in Table 4.5.

With this, making the calculations for the new antenna working in the 2.6 GHz band, through a direct correlation of the previous antenna's size, the result for this length shall be of 22.04 mm. The same was made for the 1.8 GHz frequency band.

The analysis starts by comparing both reflection coefficients in Figure 4.12 and Figure 4.13.

Table 4.5 – Comparison of different antenna's lengths among different frequencies, between theoretical and real/simulated values.

Freq. band [GHz]	1.8 (theor.)	1.8 (<i>Glass</i> / simul.)	2.4 (theor.)	2.4 (<i>Glass</i> / simul.)	2.6 (theor.)	2.6 (<i>Glass</i> / simul.)
Length [mm]	41.637	31.929	31.25	22.9	28.825	22.04

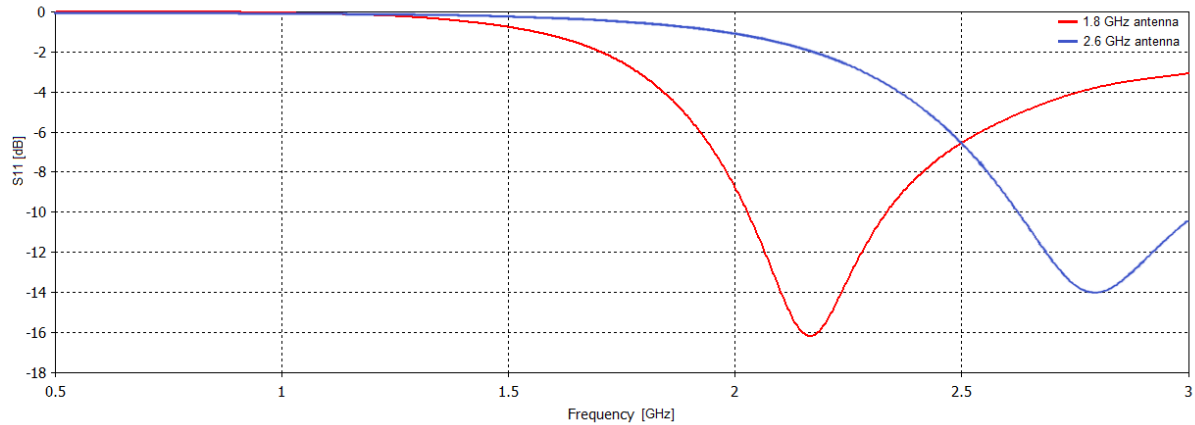


Figure 4.12 – Reflection coefficient for 1.8 GHz and 2.6 GHz designed antennas in vacuum.

As one would expect, as before, the reflection coefficients do not make the antenna naturally resonant to the frequency bands desired, in this case, the 1.8 and 2.6 GHz bands. Due to their smaller size, in comparison to what would be expected, the antennas tend to resonate in a slightly higher frequency.

The analysis follows the same approach as before, by establishing a relation between the electric field strength and the distance from the antenna, and then comparing the radiation pattern of each antenna, demonstrated throughout from Figure 4.15 to Figure 4.18, first in a top perspective, followed by a front perspective. Due to its size, both figures representing the evolution of the electric field over the distance are in Annex E.

And finally, the last analysis is on SAR, each represented on Figure 4.19 and Figure 4.20, with the maximum values for the SAR and the maximum power allowed for each antenna presented on Table 4.6 and Table 4.7.

Table 4.6 – Peak SAR readings on the voxel model at different frequencies for 1 W of power.

Freq. band [GHz]		0.8	0.9	1.8	2.1	2.4	2.6
SAR (10 g) [W/Kg]	1.8 GHz Antenna	16.28	15.43	18.87	20.56	21.37	20.86
	2.6 GHz Antenna	29.61	27.83	20.00	21.88	23.78	23.66

Table 4.7 – Maximum power permitted at different frequencies to achieve the limit of 2 W/kg.

Freq. band [GHz]		0.8	0.9	1.8	2.1	2.4	2.6
Max. Power [W]	1.8 GHz Antenna	0.1228	0.1296	0.1060	0.0972	0.0935	0.0958
	2.6 GHz Antenna	0.0675	0.0719	0.0999	0.9138	0.0841	0.0845

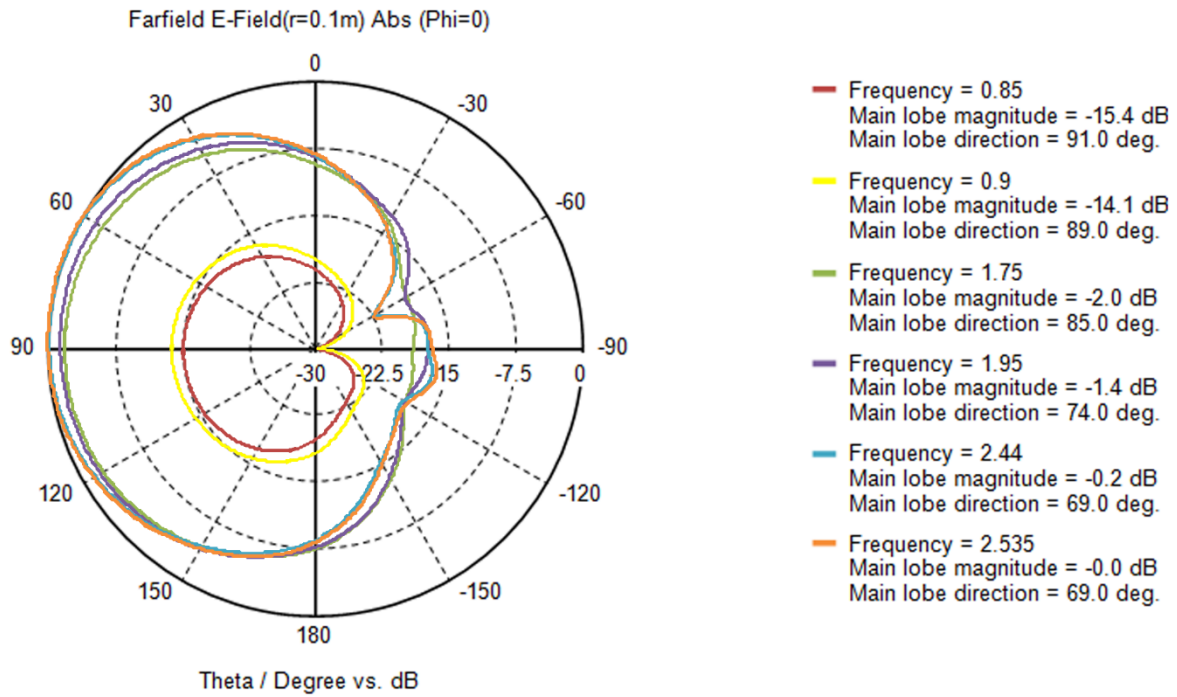


Figure 4.13 – Top cut plane on radiation pattern of 1.8 GHz designed antenna.

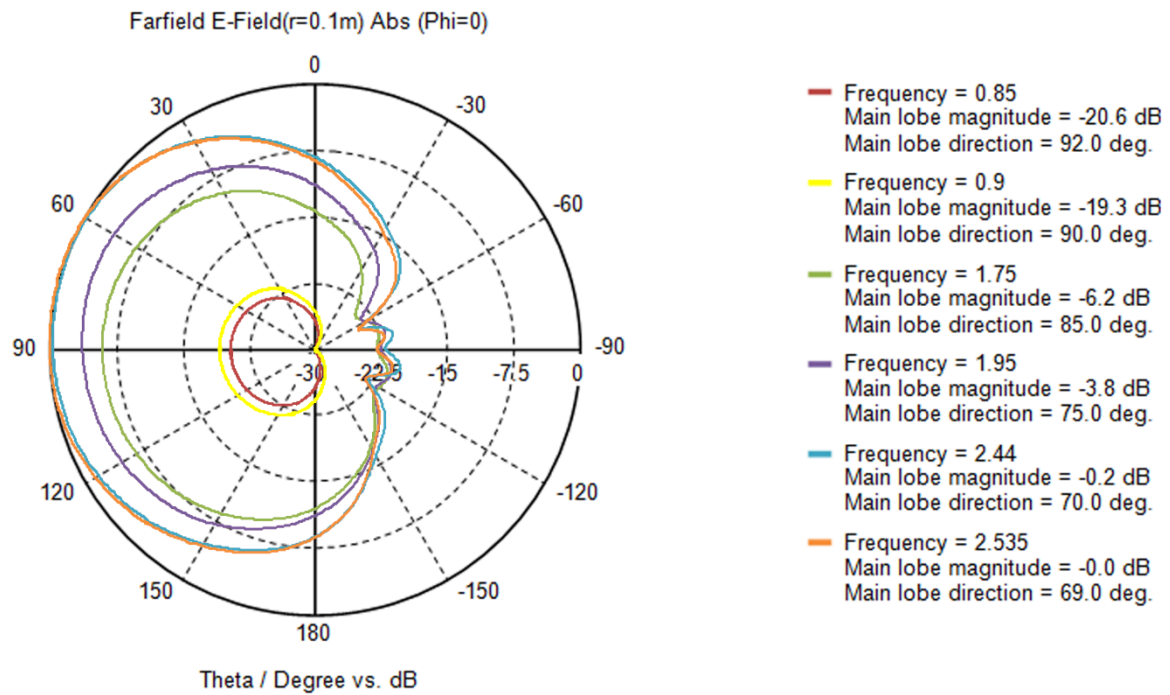


Figure 4.14 – Top cut plane on radiation pattern of 2.6 GHz designed antenna.

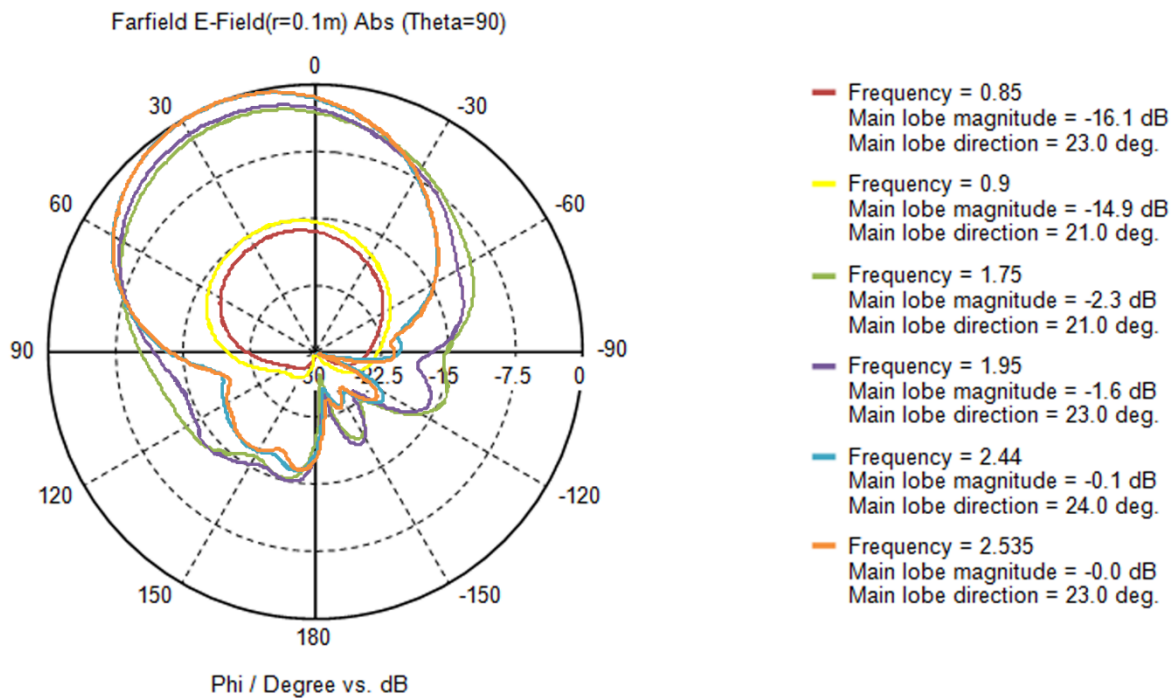


Figure 4.15 – Front cut plane on radiation pattern of 1.8 GHz designed antenna.

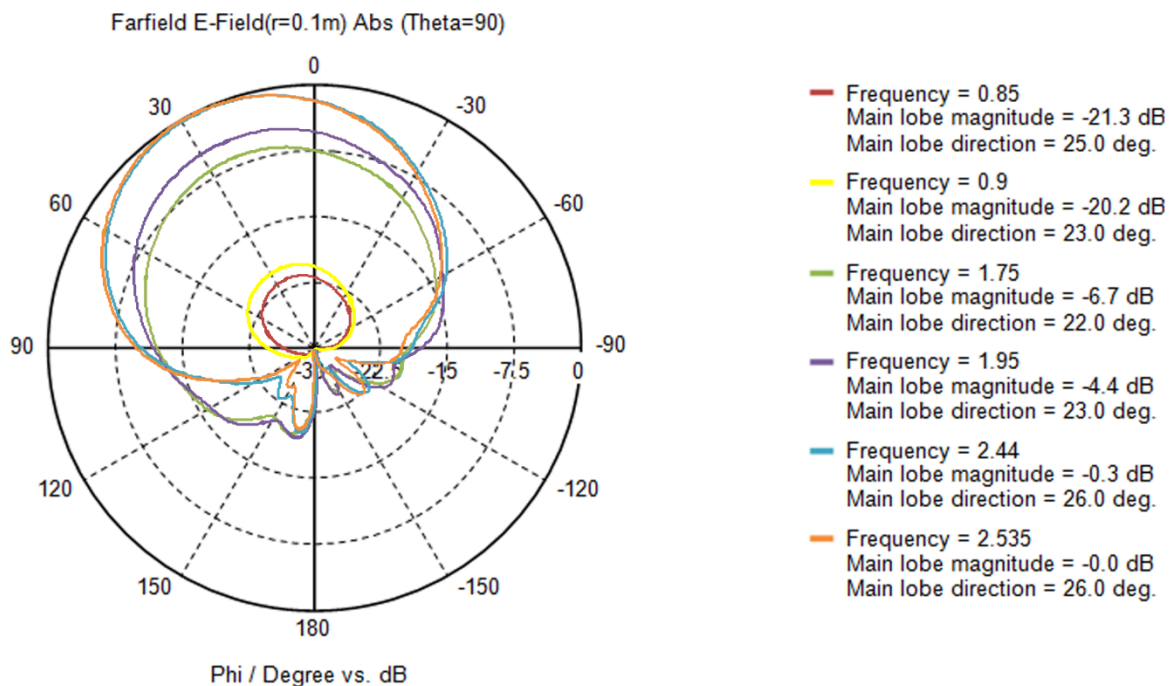


Figure 4.16 – Front cut plane on radiation pattern of 2.6 GHz designed antenna.

One can notice the less distortion and less interference for the antenna designed for 1.8 GHz in both planes. The radiation pattern is both wider and with less minimums in that antenna. Besides, while looking at the respective tables with the E-field's linear values, one can also notice that the first antenna has a higher intensity, except for the frequencies of 2.4 and 2.6 GHz, in which the second antenna has a higher value. As before, all additional information regarding the radiation pattern is found in annex E.

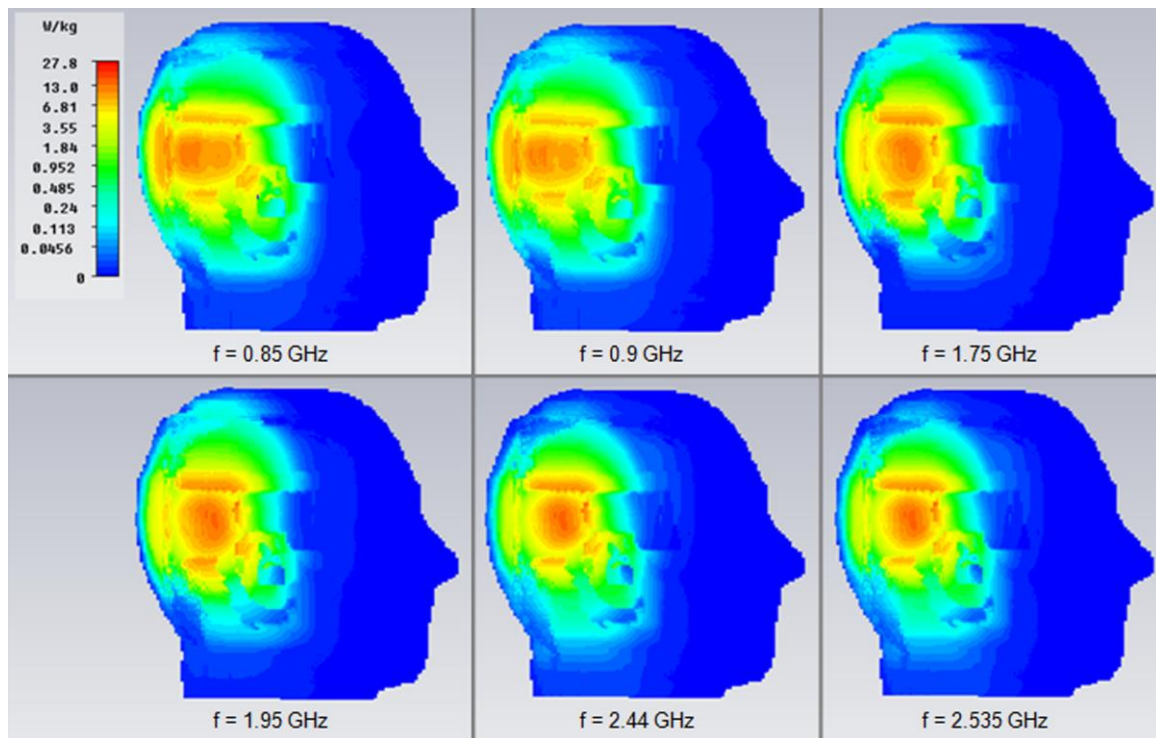


Figure 4.17 – 3D side view of the SAR range and amplitude on the voxel model for 1.8 GHz antenna.

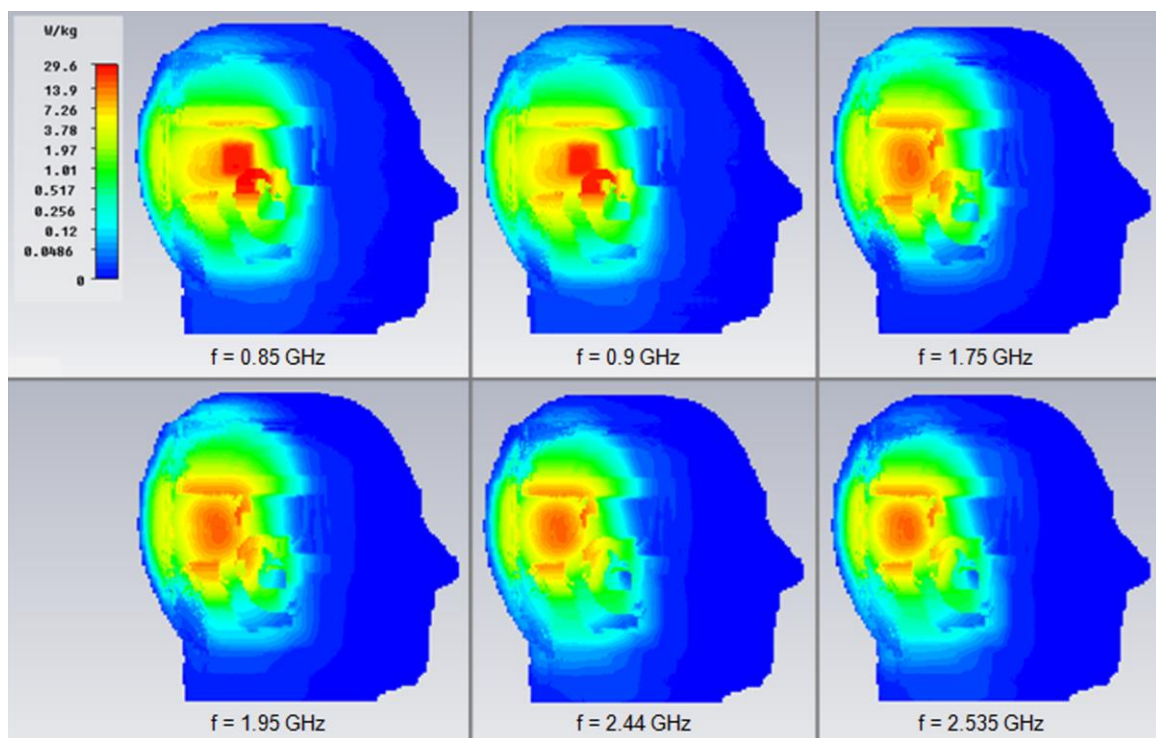


Figure 4.18 – 3D side view of the SAR range and amplitude on the voxel model for 2.6 GHz antenna

The first antenna, the one designed for the 1.8 GHz band, manages to have a much lower SAR readings when it comes to lower frequencies (0.8 and 0.9 GHz bands) than its counterpart designed for the 2.6 GHz band.

Chapter 5

Conclusions

This chapter finalises the thesis, summarising the main conclusions as well as some suggestions for future work.

With the technological advance also comes the variety and development of new devices. In 2012, *Google* unveiled a new project called *Glass*. The prototype, like its name announces clearly, consists on a pair of augmented reality glasses composed by two types of incorporated wireless systems: Wi-Fi 802.11b/g at [2412, 2462] MHz and Bluetooth low energy at [2402, 2480] MHz [FCC13]. This specific device brought a big concern among the general public regarding the exposure to radiation one would be submitted to, due to the proximity and prolonged time of use it is intended to.

The present work has the objective to analyse if cellular technologies (specifically LTE) can be implemented into this new device, and if so, if it can be feasible due to the output power, SAR limits, interference from the *Glass* module and interference from the user and its influence on the radiated wave. By putting together the model of the antenna designed and both the *Glass* and voxel model acquired, it is possible to get a full analysis of the interaction of all components together.

The reference scenario is a static heterogeneous male human voxel, with the background being defined as vacuum. The antenna in use is a whip electrically small antenna, a quarter wavelength monopole with 22.9 mm of length connected to a plane working as ground for the circuit. With the exception for the SAR analysis, the antenna is always being fed by a discrete port which feeds the antenna 1 W of power. Although the antenna is designed to work in the 2.4 GHz band, simulations were made for the entire frequency bands corresponding to GSM, UMTS and LTE, i.e., simulations were made for 0.85 GHz, 0.9 GHz, 1.75 GHz, 1.95 GHz, 2.44 GHz and 2.535 GHz, the central UL frequencies belonging to the bands of 0.8 GHz, 0.9 GHz, 1.8 GHz, 2.1 GHz, 2.4 GHz and 2.6 GHz respectively.

In Chapter 2, the main systems' backgrounds are described. GSM, UMTS and LTE architectures, respective radio interfaces, power control and transmitting power aspects are addressed, with special emphasis on these last two, due to the direct influence these fields have on the transmitted radiation. The multiple access techniques of these systems are also analysed, in order to understand how they work, thus making the simulations as realistic as possible. The chapter proceeds with an analysis and description on the human body and its dielectric properties, as well as overview of the influence radiation has on living tissue. Following up, the chapter includes a brief overview on radiation exposure, covering the basic definitions, standards and regulations imposed by national or international entities, mathematical definitions, among others. A description of the models used on this type of simulations and studies is also made, covering the existing types, their evolution over the years and different situations on where each is used. The different field regions and finally the state of the art, which covers the main work and analysis of exposure to radiation to date.

Chapter 3 presents the models proposed to evaluate the performance and radiation exposure of the systems. Starting with the mathematical models and calculations, the chapter passes on to the model of the antenna created within the simulator, along with the voxel and *Glass* model used in order to assess the main topic of the work, which are also described and explained to detail, from the dimensions of each component, to their physical properties. The used simulator was *CST Microwave Studio* and the first step in using the simulator was to decide which resolution would be the best for the data that one wants to measure, this assessment being performed only with the voxel's model head with an incident plane wave. Taking into account that the data required were the radiation pattern's shape, electric field's

strength, interference and penetration, there was no need for a very thin meshing, because all the values obtained for all meshing, with the exception to the one with LW 11 and MLRL 7, were all very similar, that the resolution chosen being LW 16 MLRL 7. Later though, due to the complexity and location of the antenna, in conjunction with the complexity of the voxel model, and also to minimise the processing load and time, the resolution used on the final simulations was LW 8 MLRL 45.

The assessment of the created antenna resulted in expected results due to its simple characteristics. The antenna, a quarter wavelength monopole, has the usual pattern of an omnidirectional antenna, a doughnut shaped radiation pattern, with both minimums at each tip of the antenna. Followed by the assessment of the antenna in conjunction with the *Glass* prototype, it was expected that the radiation pattern would not change much from the previous results, due to the paramagnetic nature of the materials composing the device. However, and although this is only true for the lower frequency bands, the influence *Glass* has is notorious considering no change was expected. The inner lobe (the one facing the centre of the device) of the radiation pattern suffers huge inference in both its pattern and amplitude. For higher frequencies however, the intensity of the wave and pattern remain unchanged. Finally for the assessment of the voxel head model, when induced with a plane wave perpendicular to its position, one can notice the low interference caused by the voxel model, given the pattern resulting is the corresponding incident plane wave, with its multiple lobes, the main one being located in the middle. Again, the interference is more noticeable on lower frequency bands.

In Chapter 4, with all the elements put together, the scenarios in which the simulations were performed are described, followed by the main results that were obtained for the different frequency bands of each technology under analysis. The initial simulations are oriented towards the original antenna present in the *Glass* prototype, initially with an analysis on its electric field's radiation pattern and amplitude, along with its penetration in the voxel head. For the last one, one can say that the electric's field effects are only noticeable until 7~8 cm towards the centre of the voxel head, until it dissipates completely or its intensity is negligible. Regarding its radiation pattern and interference, and although for the previous plane wave there is no notorious influence by the head, in this case there is a loss of ~15 dB of the antenna's signal towards the location of the voxel model, while on the opposite direction the signal is undamaged.

After this initial evaluation, the main aspect was studied: SAR. Since the worst case scenario is a device working at maximum output power, it was decided to get values for this scenario, that is, 1 W of feeding power to the antenna. But in order to have a term of comparison, and it would also be a good way to assess the entire work, a simulation was made reproducing the evaluation done by the FCC on the *Glass*; results are as expected, or at least, the one regarding the FCC's values, with only a difference of 0.02 W/kg from the reports obtained by FCC. Regarding the SAR values for 1 W, although for the entire frequency range the values are all too high to be accepted (according to the recommended limits), one must take into account that this power is the peak power a handheld device can use, and very rarely it reaches this value. Also, on the 3D and 2D diagrams, it is easy to once again see the conclusion taken before regarding the penetration of the wave on the voxel model, knowing the model's dimensions and that the centre of the head is around 10 cm from the antenna.

Then the opposite situation was studied, i.e., the parameter to be found was the maximum power allowed, knowing the SAR recorded would be 2 W/kg averaged on 10 g of tissue, which is the limit when it comes to European regulations. For these results, the diagrams are obviously the same or at least very similar to every frequency, since they depict the SAR values. Regarding the main frequency bands of LTE, the maximum power is 106.3 mW for 1.8 GHz and 97.1 mW for 2.6 GHz. This is an acceptable power usage from a mobile device, since the peak power for an LTE device is 200 mW and while in idle, the minimum to guarantee continuous connection to a BS is 0.1 mW. An average consumption for a mobile phone in LTE, although it depends mainly on the manufacturer, brand and model, and if other systems are activated, is 40 mW for a voice call.

Regarding the last simulations and analysis, the variation of the antenna's length, all the same parameters and values were collected as before, on a denser scale and with less details for each aspect. The S_{11} parameter, as the original antenna, does not match exactly the frequency it is designed for, since the actual length of the antenna does not match exactly the theoretical dimensions, although the S_{11} parameter for the 1.8 GHz antenna presents a better value than its 2.6 GHz counterpart. In an overall analysis, comparing every result obtained as a total, one can see the antenna for 1.8 GHz has a better performance. It has a better S_{11} parameter as stated, its electric field's evolution over the distance is much more uniform and resembles more the antenna in vacuum, suggesting less interference from the voxel head. This can also be concluded from the radiation pattern, where one notices, beside its less modified shape, it has a bigger loss in amplitude when it comes to the 2.6 GHz antenna. While it registers a loss of ~15 dB for the 1.8 GHz antenna, for the 2.6 GHz antenna, a loss of almost 22.5 dB is registered. Finally regarding SAR, the antenna for 1.8 GHz again has a better performance, although still not able to overtake the original antenna. So while regarding interference, the new designed antenna manages to get the better than the original one, it still lacks the performance when it comes to SAR and output power limit.

The final conclusion, concerning if the *Glass* prototype could have a cellular module incorporated besides the Wi-Fi, one could say yes, although a power limit has to be imposed, so not to pass the regulated SAR limits. This would also mean a change in the type of battery used on the device, since additional modules, especially cellular ones, would consume more power, degrading the life time the battery would be running. Also, limiting the power the device can use would force the user to only be able to have the desired connection quality on a urban area, or similar zone, where the cluster of BS are denser, and the number of pico-cells is higher, since one of the main reasons for an MT to need more power for the antenna is the larger distance to the BS. The bigger the distance, more output power it needs to maintain the connection quality. So the limitations would come down to 3 main aspects: imposed power limit, better battery (or one with more capacity) and conditional areas of use to maintain quality of service.

These last aspects could be something to investigate in a near future. Also, the continuous and prolonged exposure due to the type of usage of *Glass* should be investigated further. From this work one can assume and derive the potential harm done by this device, and I also agree with the many who tested and objected about the perils of using *Glass*.

Annex A

LTE Frequency Bands

This annex consists of a more thorough overview of the frequency bands available for LTE, as well as the bands' usage by each world's region. It also specifies the respective frequency assignment in Portugal, by each telecommunications operator, with the results of the auction held by ANACOM.

The assigned frequency bands for E-UTRA are detailed in Table A.1, according to 3GPP Release 11.

Table A.1 - E-UTRA frequency bands [3GPP13b] and [HoTo11].

E-UTRA operating band	UL Band BS receive, UE transmit [MHz]	DL Band BS transmit, UE receive [MHz]	Duplex mode	Common name	Frequency band (MHz)
1	[1920, 1980]	[2110, 2170]	FDD	IMT	2100
2	[1850, 1910]	[1930, 1990]	FDD	PCS	1900
3	[1710, 1785]	[1805, 1880]	FDD	DCS	1800
4	[1710, 1755]	[2110, 2155]	FDD	AWS (AWS-1)	1700
5	[824, 849]	[869, 894]	FDD	CLR	850
6	[830, 840]	[875, 885]	FDD	UMTS 800	850
7	[2500, 2570]	[2620, 2690]	FDD	IMT-E	2600
8	[880, 915]	[925, 960]	FDD	E-GSM	900
9	[1749.9, 1784.9]	[1844.9, 1879.9]	FDD	UMTS 1700 / Japan DCS	1800
10	[1710, 1770]	[2110, 2170]	FDD	Extended AWS	1700
11	[1427.9, 1447.9]	[1475.9, 1495.9]	FDD	Lower PDC	1500
12	[699, 716]	[729, 746]	FDD	Lower SMH blocks A/B/C	700
13	[777, 787]	[746, 756]	FDD	Upper SMH block C	700
14	[788, 798]	[758, 768]	FDD	Upper SMH block D	700
15	[1900, 1920]	[2600, 2620]	FDD	Reserved	
16	[2010, 2025]	[2585, 2600]	FDD	Reserved	
17	[704, 716]	[734, 746]	FDD	Lower SMH blocks B/C	700
18	[815, 830]	[860, 875]	FDD	Japan lower 800	850
19	[830, 845]	[875, 890]	FDD	Japan upper 800	850
20	[832, 862]	[791, 821]	FDD	EU Digital Dividend	800
21	[1447.9, 1462.9]	[1495.9, 1510.9]	FDD	Upper PDC	1500
22	[3410, 3490]	[3510, 3590]	FDD		3500
23	[2000, 2020]	[2180, 2200]	FDD	S-Band (AWS-4)	2000
24	[1626.5, 1660.5]	[1525, 1559]	FDD	L-Band	1600
25	[1850, 1915]	[1930, 1995]	FDD	Extended PCS	1900
26	[814, 849]	[859, 894]	FDD	Extended CLR	850
27	[807, 824]	[852, 869]	FDD	SMR	850
28	[703, 748]	[758, 803]	FDD	APAC	700
29	n/a	[716, 728]	FDD	Lower SMH blocks D/E	700
30	[2305, 2315]	[2350, 2360]	FDD	WCS blocks A/B	2300
Bands not assigned					
33	[1900, 1920]		TDD	IMT	2100
34	[2010, 2025]		TDD	IMT	2100
35	[1850, 1910]		TDD	PCS (UL)	1900
36	[1930, 1990]		TDD	PCS (DL)	1900
37	[1910, 1930]		TDD	PCS (Duplex spacing)	1900
38	[2570, 2620]		TDD	IMT-E	2600
39	[1880, 1920]		TDD		1900
40	[2300, 2400]		TDD		2300
41	[2496, 2690]		TDD	BRS / EBS	2500
42	[3400, 3600]		TDD		3500
43	[3600, 3800]		TDD		3700
44	[703, 803]		TDD	APAC	700

To notice that in grey are presented the bands that are not available, were not assigned or not applicable.

The FDD frequency bands available for each of the world's regions are illustrated Table A.2, namely for Europe, Asia, Japan, Americas and Oceania. The main bands are represented in bold.

Table A.2 - FDD Frequency bands' usage by world's region (adapted from [HoTo11]).

Operating band	Frequency band	North America	Latin America	Europe	Asia	Oceania
1	2100	N/A	N/A	(no deployments)	Japan, Philippines, South Korea, Tajikistan, Thailand	(no deployments)
2	1900	USA	Dominican Republic, Paraguay	N/A	N/A	N/A
3	1800	N/A	Aruba, Cayman Islands, Dominican Republic, Venezuela	Yes	Yes	Yes
4	1700	Yes	Yes	N/A	N/A	N/A
5	850	USA	N/A	N/A	South Korea	(no deployments)
7	2600	Canada	Yes	Yes	Yes	Australia, New Zealand (<i>in Trial</i>)
8	900	N/A	N/A	Czech Republic	South Korea, Japan, Taiwan	Australia
9	1700	N/A	N/A	N/A	Japan	N/A
10	1700	(no deployments)	(no deployments)	N/A	N/A	N/A
11	1500	N/A	N/A	N/A	Japan	N/A
12	700	USA	N/A	N/A	N/A	Kiribati
13	700	Canada (<i>planned</i>), USA	Bolivia	N/A	N/A	N/A
17	700	USA	Antigua & Barbuda, Bahamas, Cayman Islands	N/A	N/A	N/A
18	800	N/A	N/A	N/A	Japan	N/A
17	700	USA	Antigua & Barbuda, Bahamas, Cayman Islands	N/A	(<i>to be replaced by band 26</i>)	N/A
19	800	N/A	N/A	N/A	Japan	N/A
20	800	N/A	N/A	Yes	Qatar	Fiji
22	3500	N/A	N/A	(no deployments)	N/A	N/A
23	2000	USA	N/A	N/A	N/A	N/A
28	700	N/A	(no deployments)	(no deployments)	Taiwan, Japan	Australia, New Zealand (<i>in Trial</i>)

The results of the auction held by ANACOM for the 450, 800, 900, 1800, 2100 and 2600 MHz are shown in Table A.3, with the assigned frequency bands and corresponding bandwidth for each Portuguese operator.

Table A.3 - Results from ANACOM auction for frequency bands (adapted from [ANAC14]).

Frequency Band [MHz]	Bandwidth [MHz]	Assigned Operator
450	2 × 1.25	-
800	2 × 5	TMN
800	2 × 5	TMN
800	2 × 5	Vodafone
800	2 × 5	Vodafone
800	2 × 5	Optimus
800	2 × 5	Optimus
900	2 × 5	-
900	2 × 5	Vodafone
1800	2 × 5	TMN
1800	2 × 5	TMN
1800	2 × 5	Vodafone
1800	2 × 5	Vodafone
1800	2 × 5	Optimus
1800	2 × 5	Optimus
1800	2 × 5	-
1800	2 × 5	-
1800	2 × 4	TMN
1800	2 × 4	Vodafone
1800	2 × 4	Optimus
2100	5	-
2100	5	-
2600	2 × 5	TMN
2600	2 × 5	TMN
2600	2 × 5	TMN
2600	2 × 5	TMN
2600	2 × 5	Vodafone
2600	2 × 5	Vodafone
2600	2 × 5	Vodafone
2600	2 × 5	Vodafone
2600	2 × 5	Optimus
2600	2 × 5	Optimus
2600	2 × 5	Optimus
2600	2 × 5	Optimus
2600	2 × 5	-
2600	2 × 5	-
2600	25	Vodafone
2600	25	-

Annex B

Dielectric Properties of Main Body Tissues

Since the dielectric properties of body tissues vary with frequency, it is helpful to see and understand this variation.

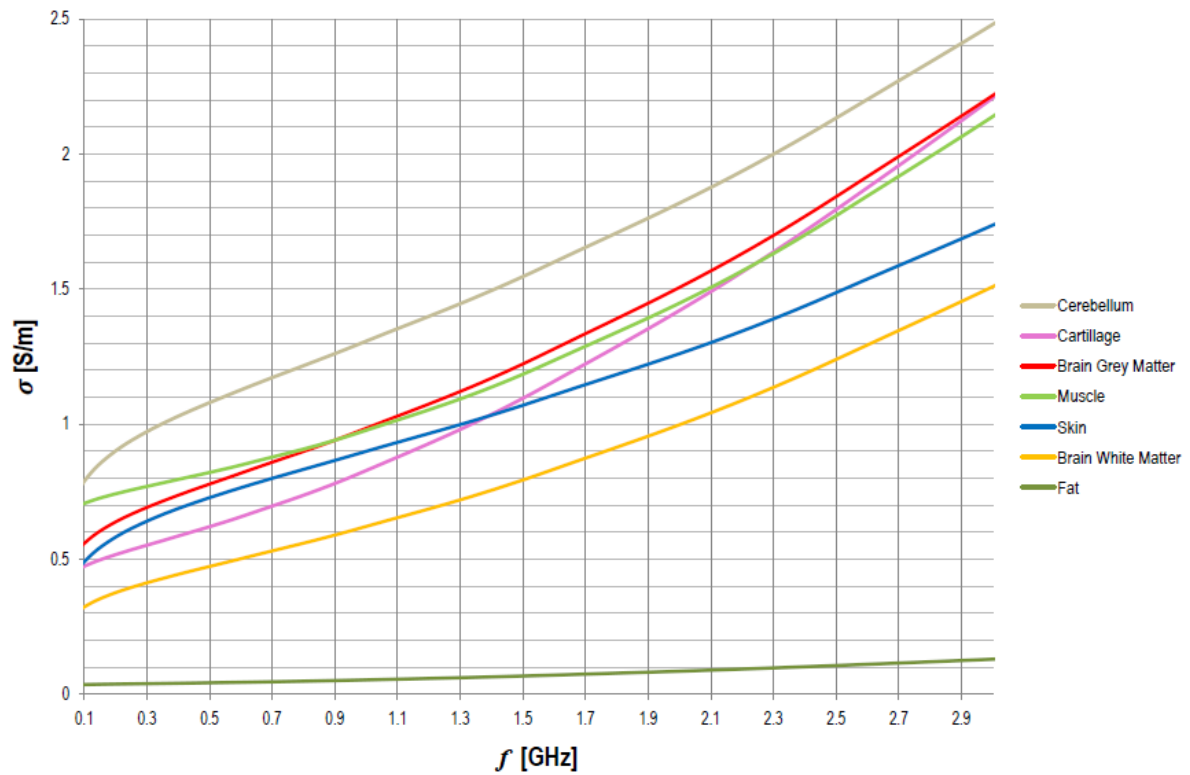


Figure B.1 - Conductivity of the most important body tissues (extracted from [Lo10]).

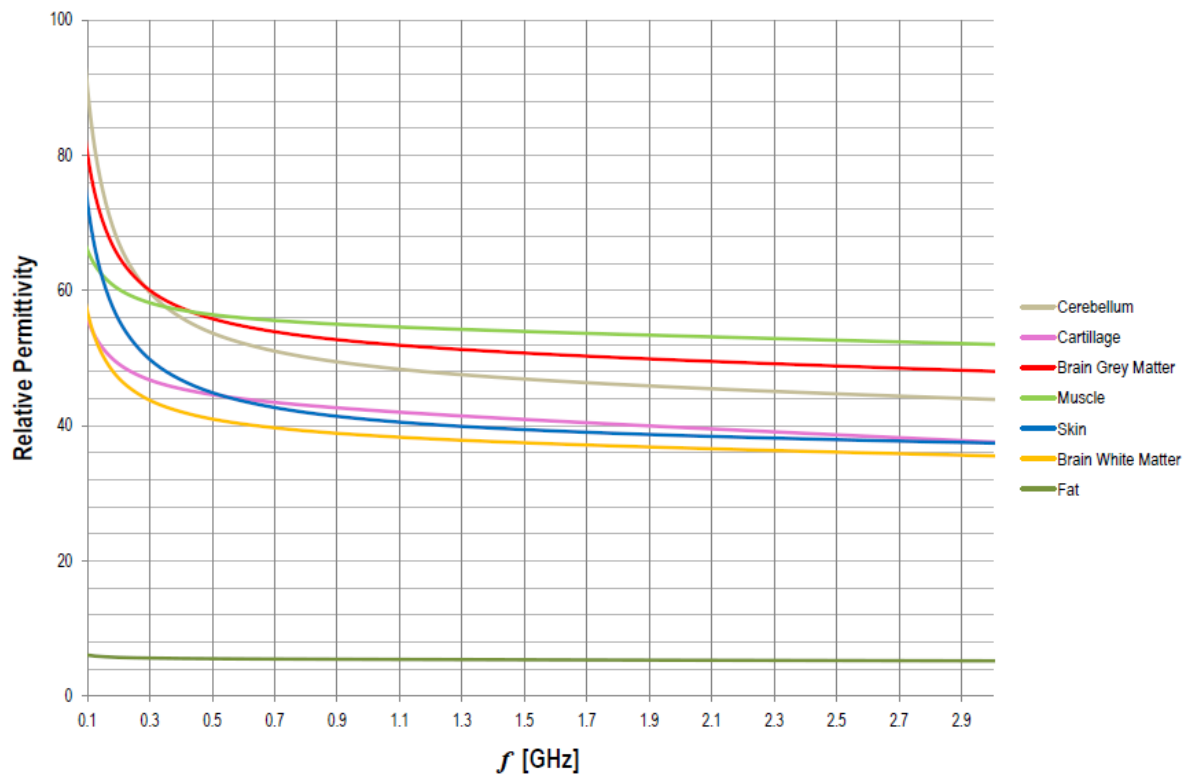


Figure B.2 - Relative permittivity of the most important body tissues (extracted from [Lo10]).

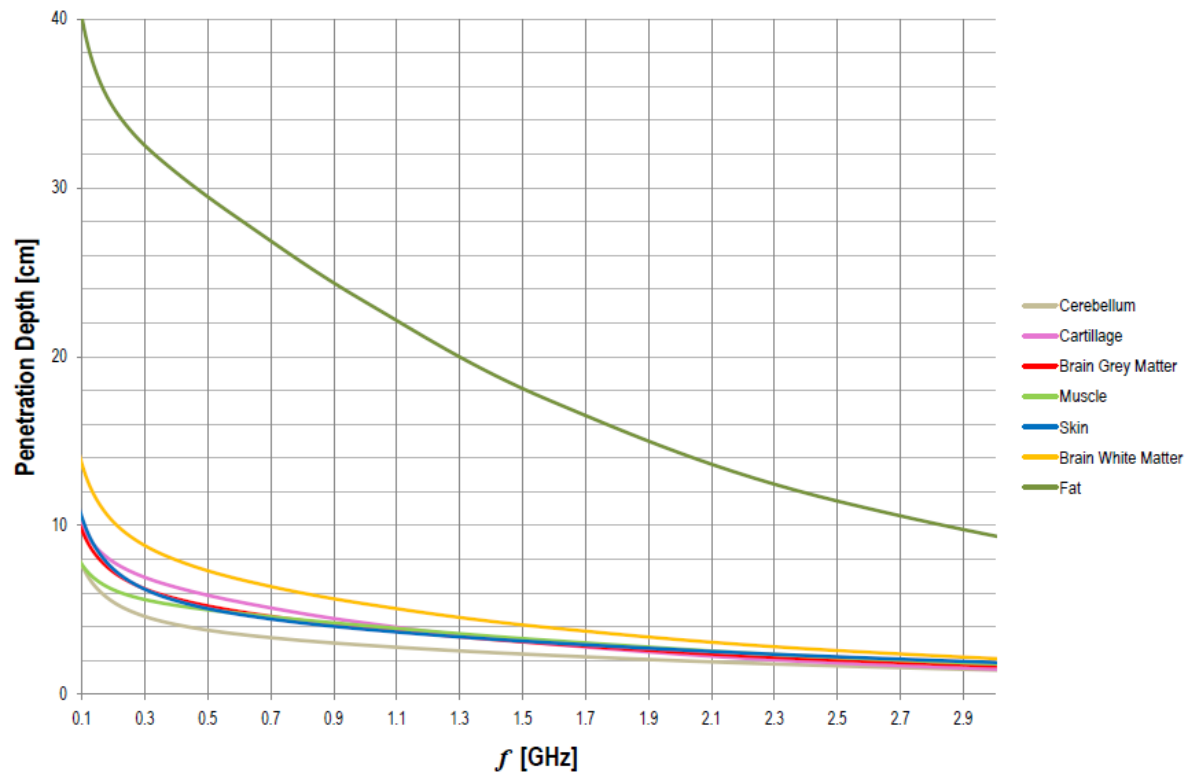


Figure B.3 - Penetration depths of the most important body tissues (extracted from [Lo10]).

Annex C

Materials Used in Simulations

A list of all the materials used in the simulations and their most important physical properties at 2.6 GHz.

Table C.1 - Physical properties of the used materials

Material type	Relative permittivity	Electrical conductivity [S/m]	Volumetric mass density [kg/m ³]
Internal air	1.000	0.000	0.0
Artery	58.015	2.676	1060.0
Blood vessel	58.015	2.676	1060.0
Bone	11.293	0.424	1990.0
Grey matter (brain)	48.669	1.915	1039.0
White matter (brain)	35.991	1.292	1043.0
Cartilage	38.449	1.874	1100.0
Cerebellum	44.544	2.201	1040.0
Cerebrospinal fluid	66.015	3.599	1007.0
Commissura anterior	35.991	1.292	1043.0
Connective tissue	10.775	0.288	1013.0
Cornea	51.371	2.408	1076.0
Ear cartilage	38.449	1.874	1100.0
Ear skin	37.845	1.536	1100.0
Eye lens	44.459	1.598	1090.0
Eye sclera	52.418	2.146	1032.0
Eye vitreous humor	68.109	2.599	1009.0
Fat	5.265	0.111	916.0
Hippocampus	48.669	1.915	1039.0
Hypophysis	56.984	2.090	1066.0
Hypothalamus	56.984	2.090	1050.0
Intervertebral disc	38.449	1.874	1100.0
Larynx	38.449	1.874	1082.0
Mandible	11.293	0.424	1990.0

Table C.2 (cont.) - Physical properties of the used materials

Marrow red	5.281	0.102	1027.0
Medulla oblongata	42.330	1.603	1039.0
Midbrain	42.330	1.603	1039.0
Mucosa	42.645	1.684	1050.0
Muscle	52.546	1.843	1041.0
Nerve	29.997	1.151	1038.0
Pharynx	1.000	0.000	0.0
Pinealbody	56.984	2.090	1050.0
Pons	42.330	1.603	1039.0
Sat	10.775	0.000	916.0
Skin	37.845	1.536	1100.0
Skull	11.293	0.424	1990.0
Spinal cord	29.997	1.151	1038.0
Teeth	11.293	0.424	2160.0
Tendon ligament	42.853	1.810	1110.0
Thalamus	48.669	1.915	1039.0
Tongue	52.418	1.915	1041.0
Vein	58.015	2.676	1060.0
Vertebrae	11.293	0.424	1990.0
Teflon	2.1	1.0×10^{-25}	2200.0
Titanium	120.165	2.380×10^6	4420
Vacuum	1	0.0	0.0

Annex D

Additional information on modelling

Different perspectives of the radiation patterns and tables with the magnitudes of main lobes in linear units, corresponding to the readings in dB.

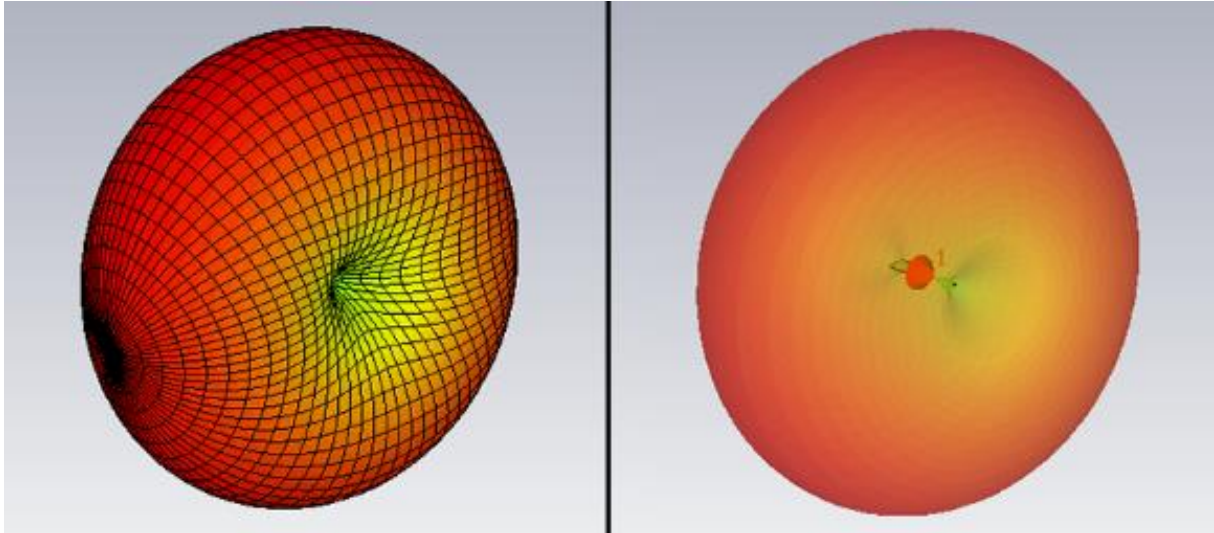


Figure D.1 – 3D perspective of antenna in vacuum.

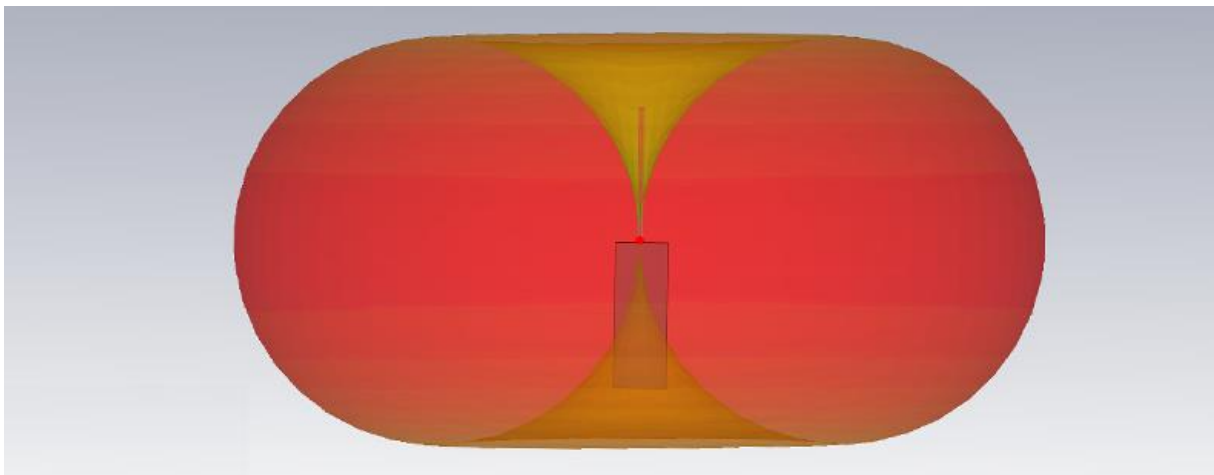


Figure D.2 – Side view of 3D perspective of antenna in vacuum, with main lobes visible.

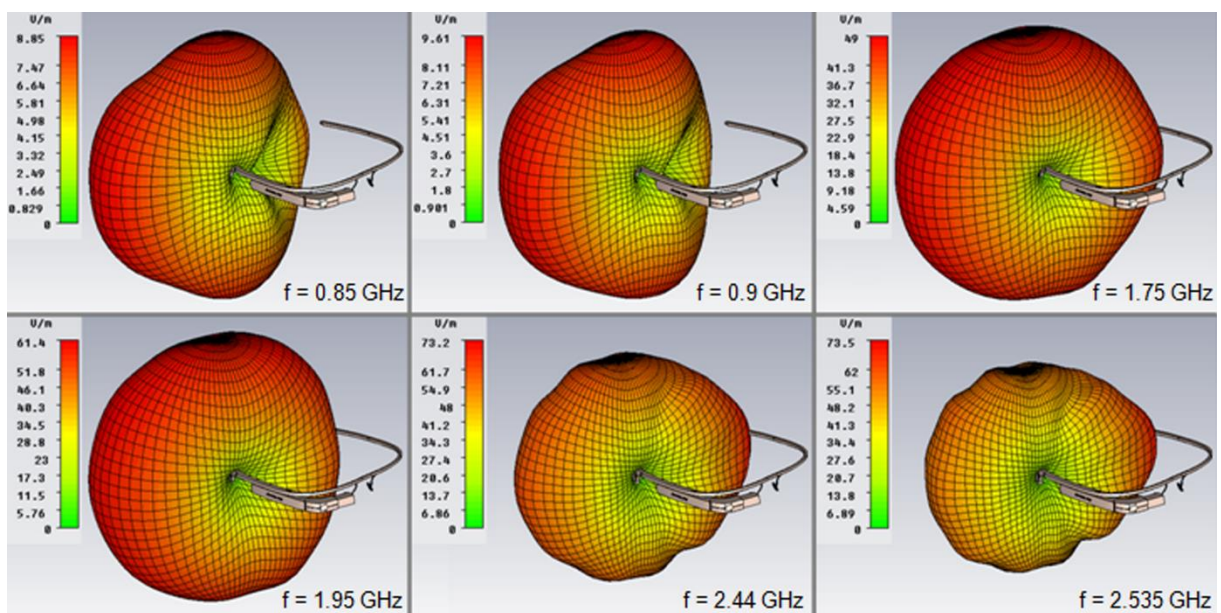


Figure D.3 – 3D perspectives of antenna in *Glass* for each frequency band, with scale in linear units.

Table D.1 – Linear values correspondent to amplitudes of main lobes, on radiation pattern charts from Chapter 3.

Frequency [GHz]		0.8	0.9	1.8	2.1	2.4	2.6
Antenna alone [V/m]	Top	3.55	3.95	21.3	30.4	58.2	62.3
	Front	3.54	3.95	21.3	30.4	58.1	62.1
Antenna + Glass [V/m]	Top	8.8	9.42	48.5	60.4	73.3	73.7
	Front	8.69	9.4	48.7	61	68.4	68.7

Annex E

Additional results

Additional results such as different SAR perspectives that are not shown in Chapter 4 to avoid overflow of figures.

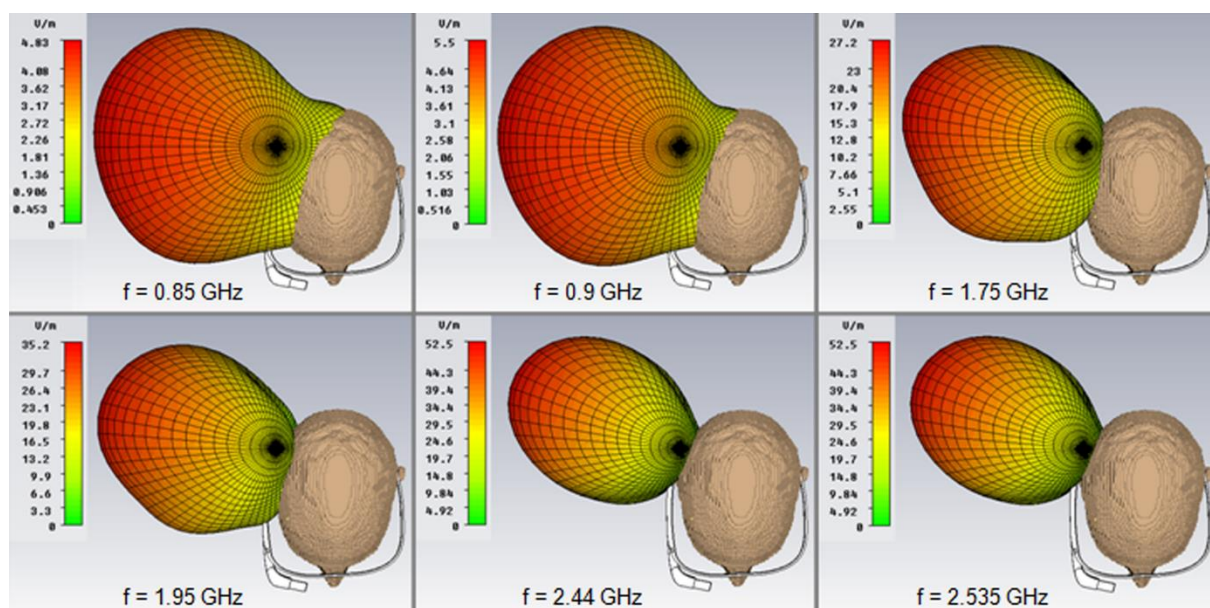


Figure E.1 – Top view of 3D perspective of radiation pattern from original antenna.

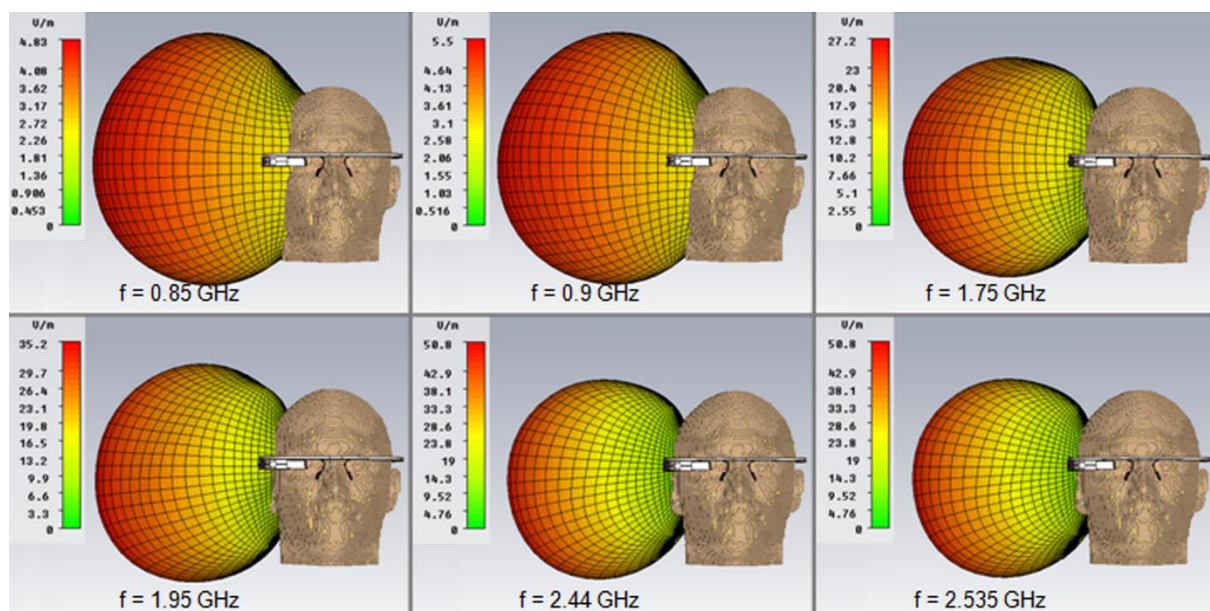
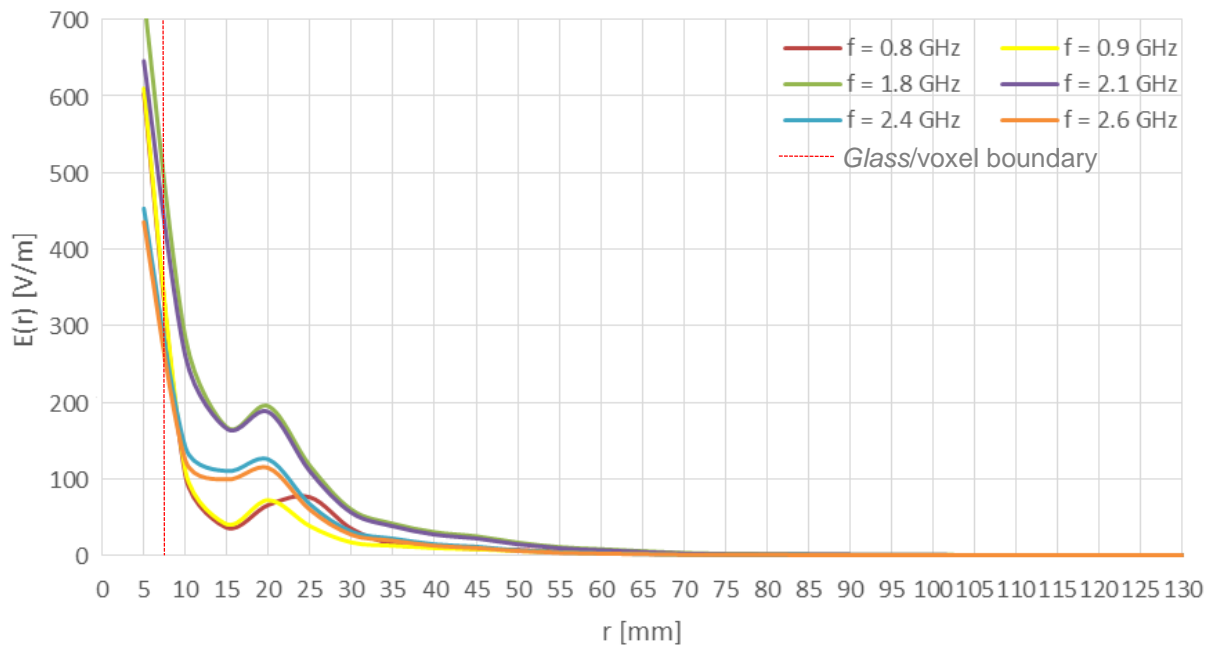
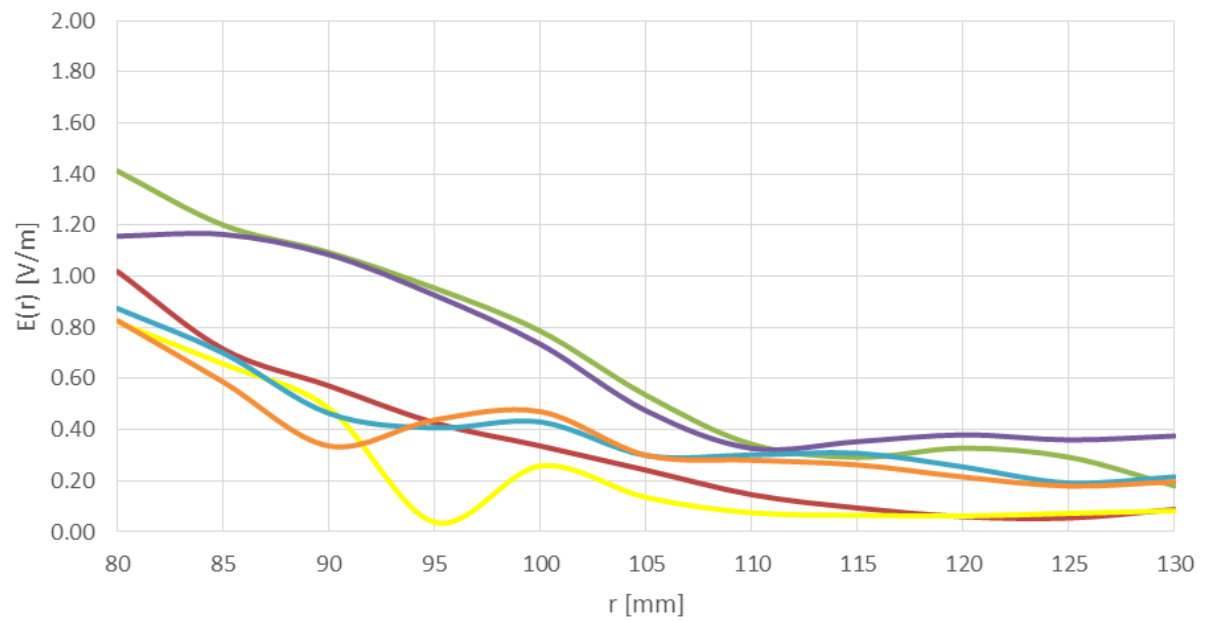


Figure E.2 – Front view of 3D perspective of radiation pattern from original antenna.

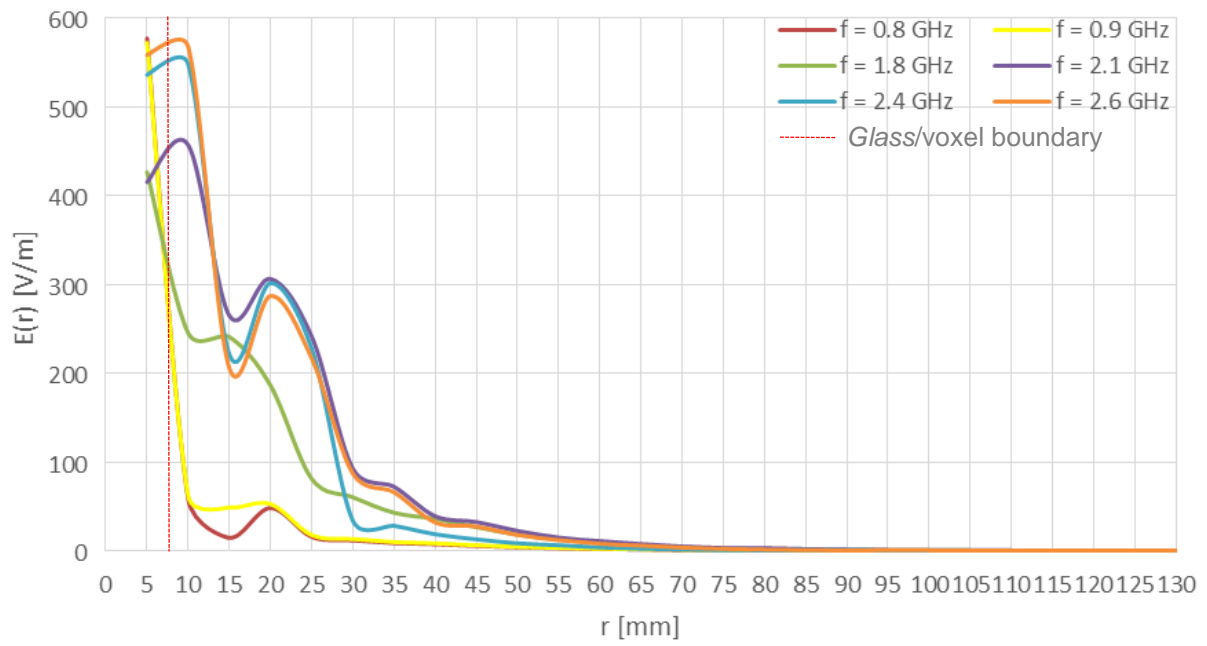


(a) – Entire distance

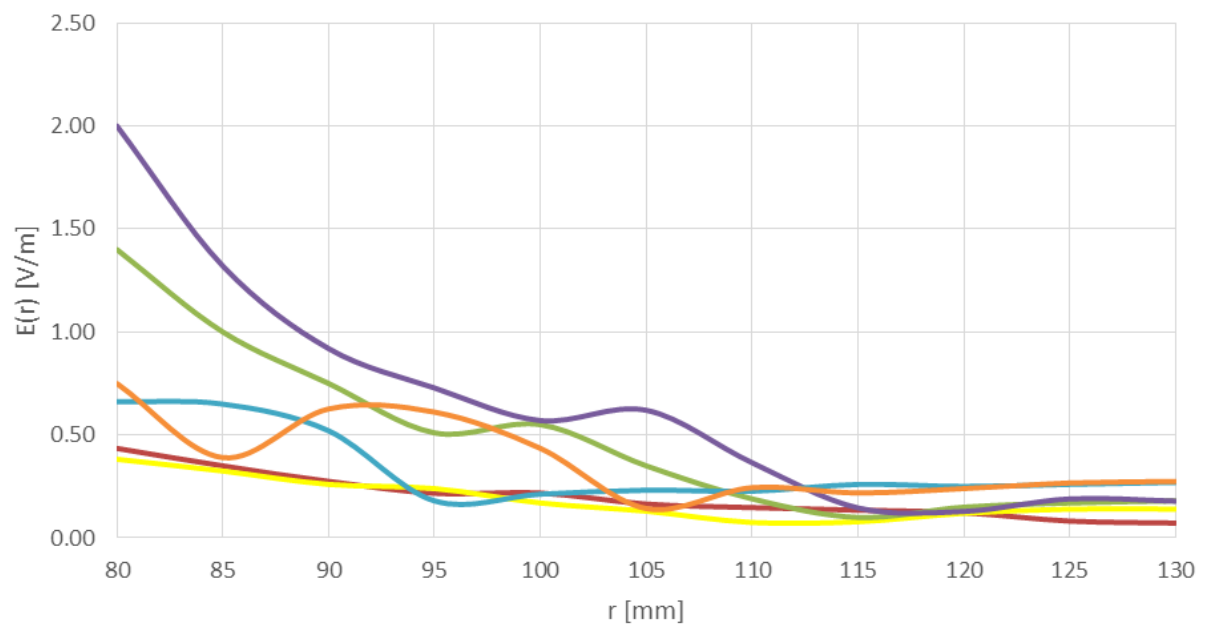


(b) – Further distance amplified.

Figure E.3 – Evolution of E-field over distance of antenna designed for 1.8 GHz, amplified for greater distances.



(a) – Entire distance



(b) – Further distance amplified.

Figure E.4 – Evolution of E-field over distance of antenna designed for 2.6 GHz, amplified for greater distances.

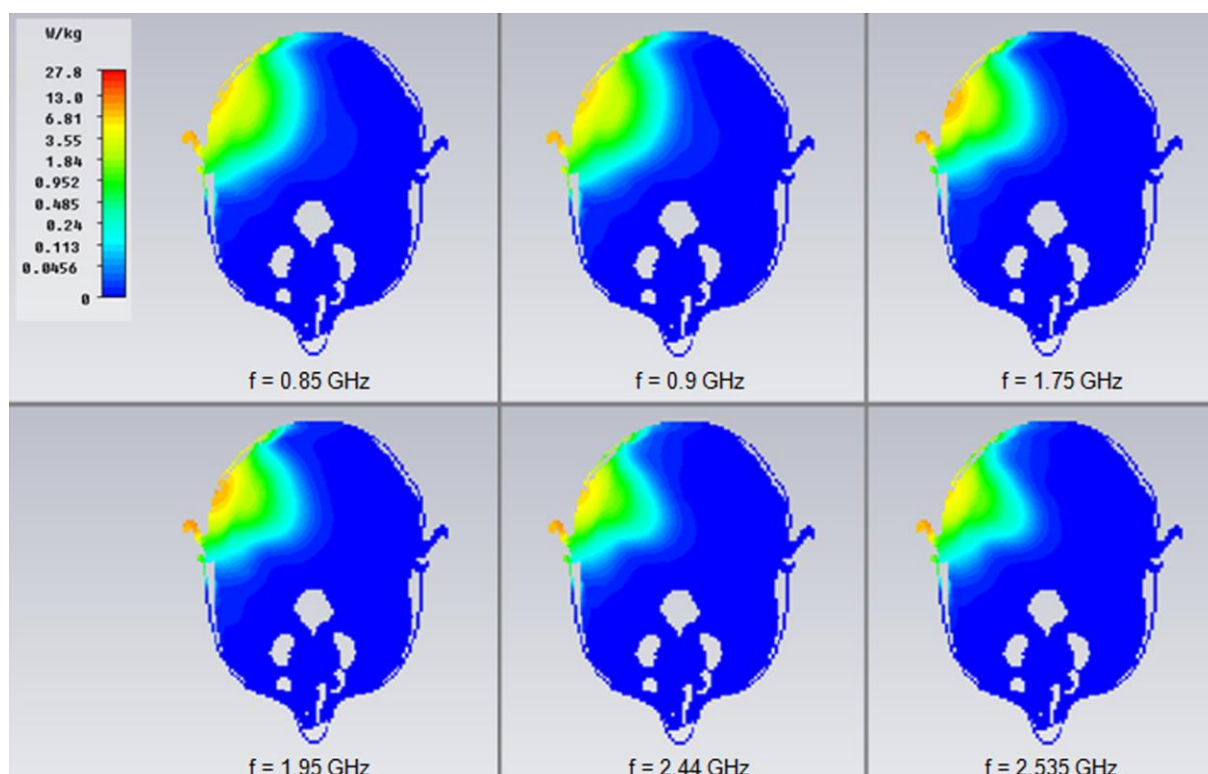


Figure E.5 – Top cut plane for maximum SAR reading on antenna designed for 1.8 GHz

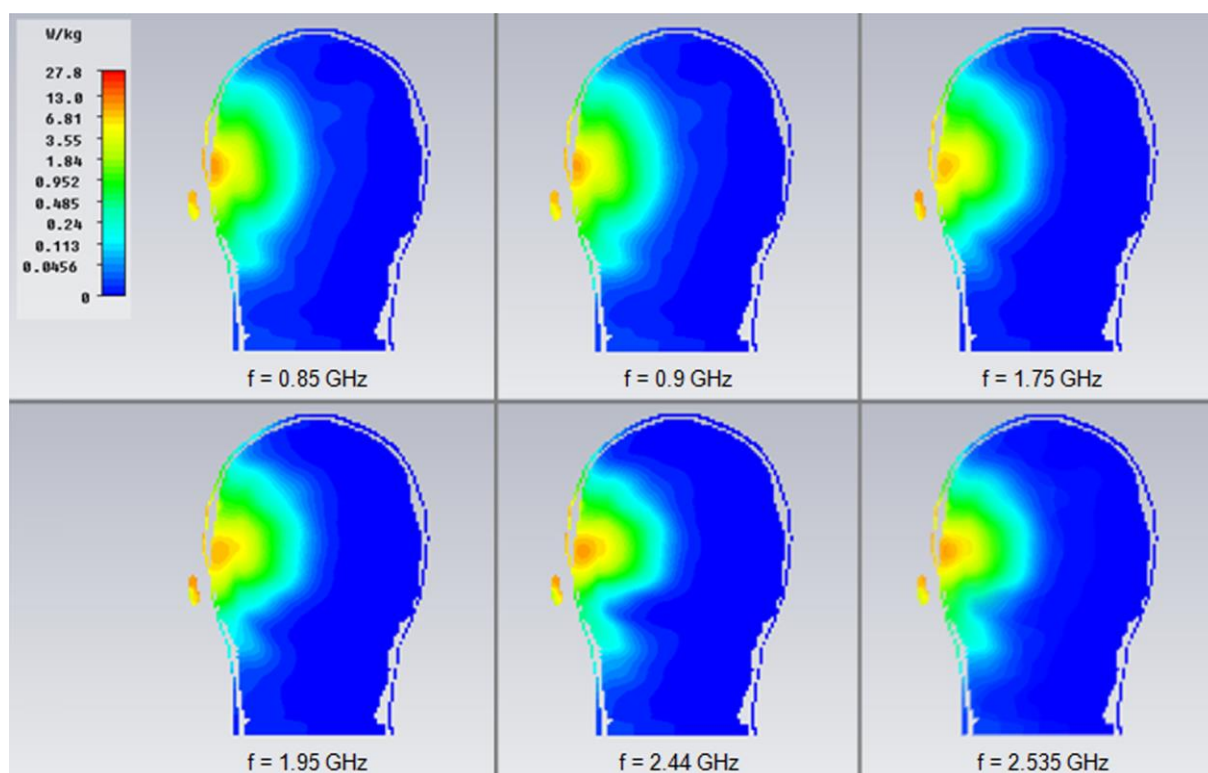


Figure E.6 – Front cut plane for maximum SAR reading on antenna designed for 1.8 GHz

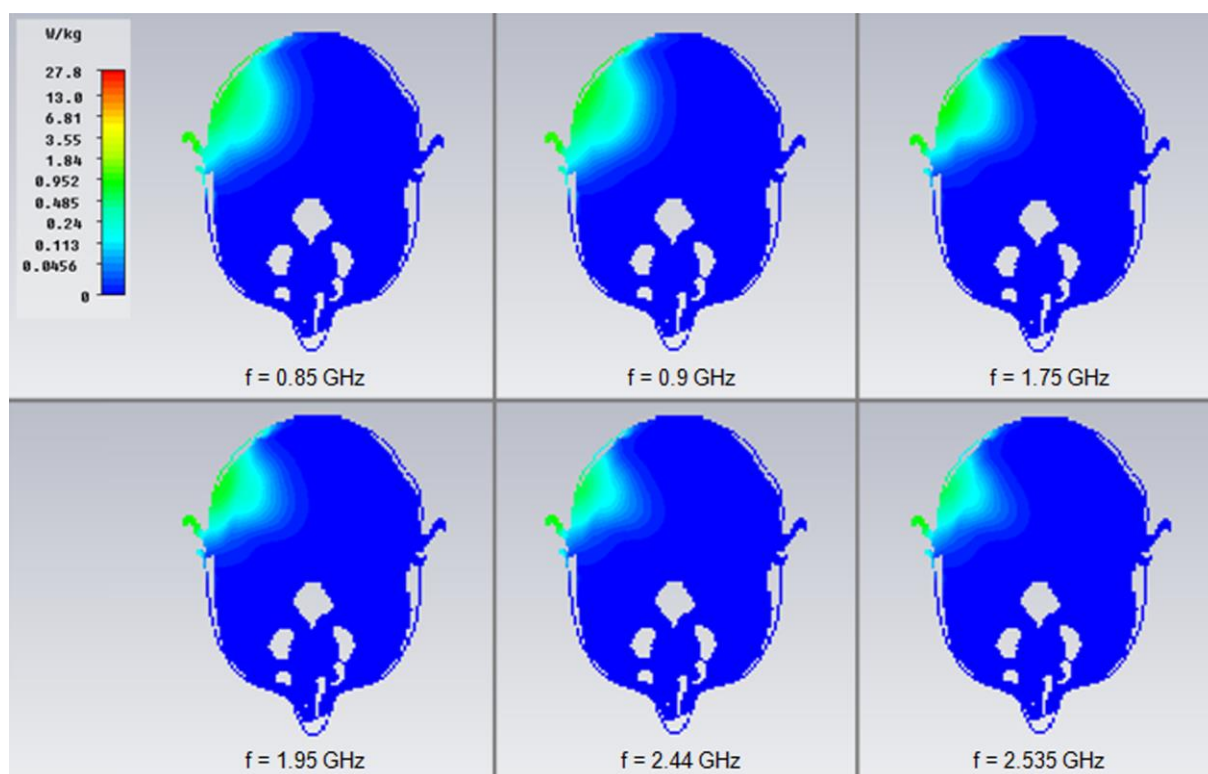


Figure E.7 – Top cut plane for maximum allowed power on antenna designed for 1.8 GHz.

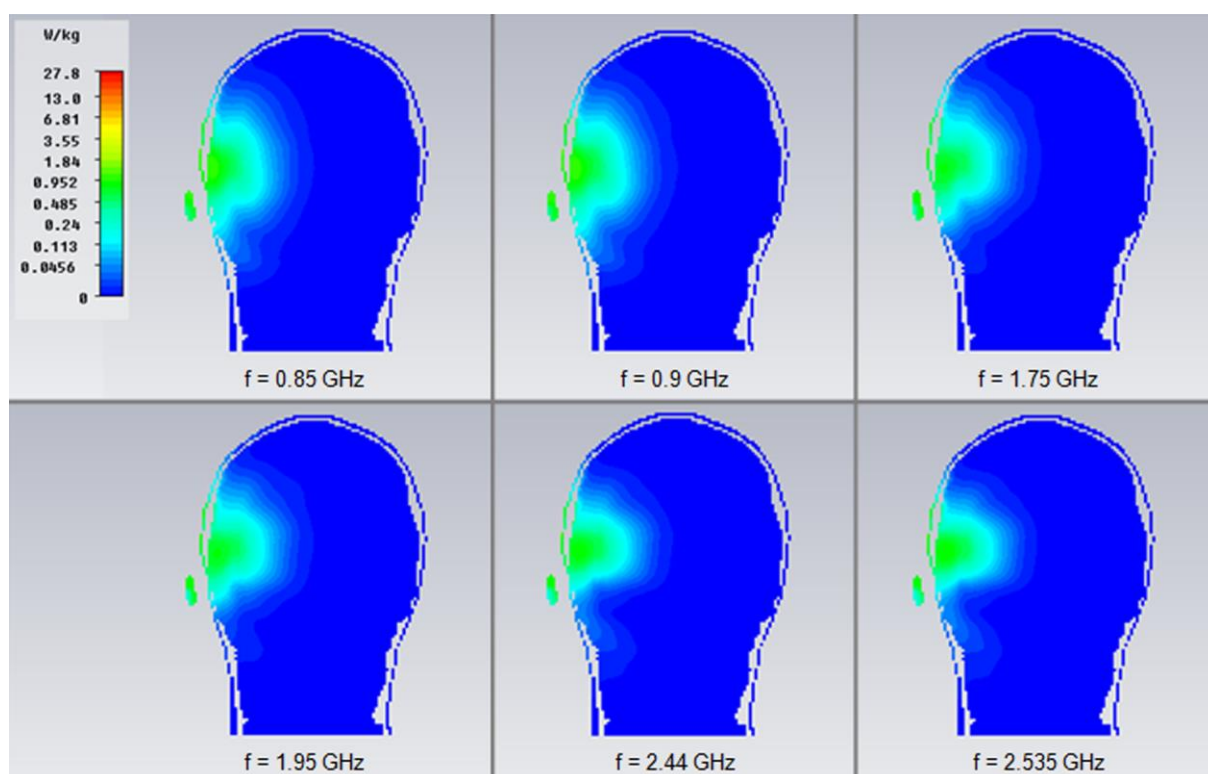


Figure E.8 – Front cut plane for maximum allowed power on antenna designed for 1.8 GHz.

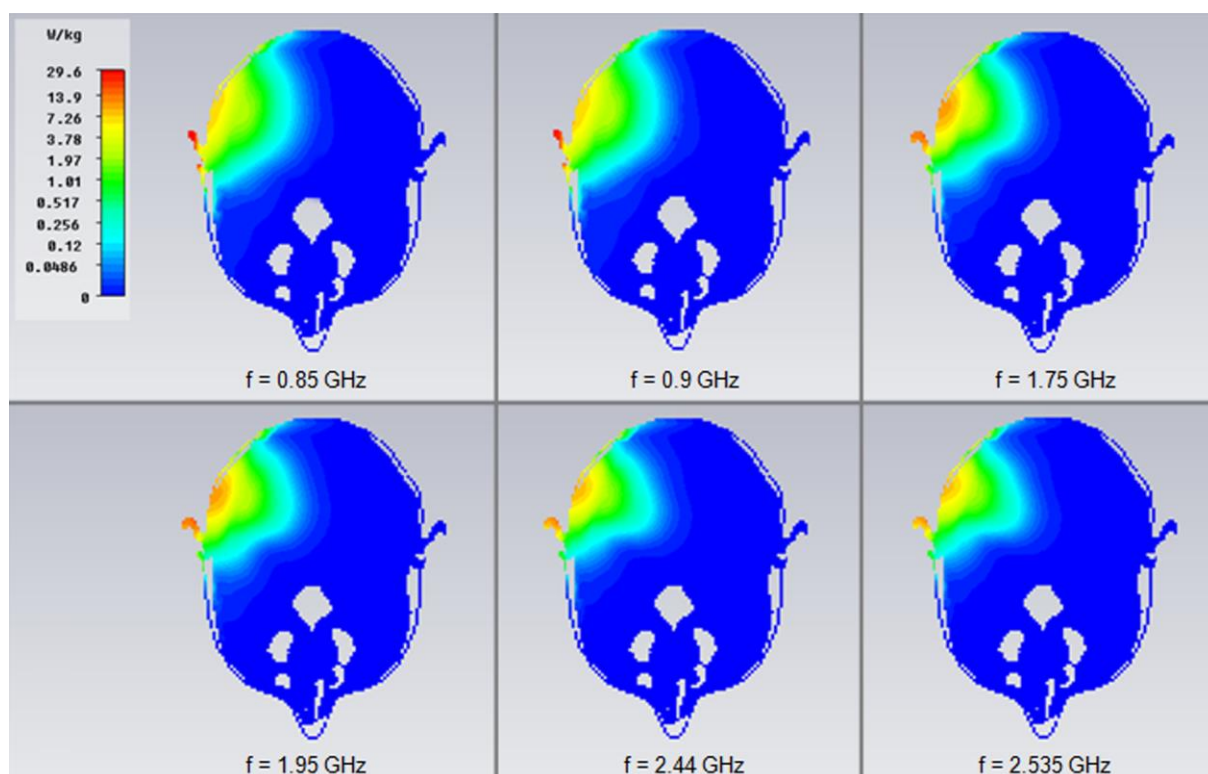


Figure E.9 – Top cut plane for maximum SAR reading on antenna designed for 2.6 GHz

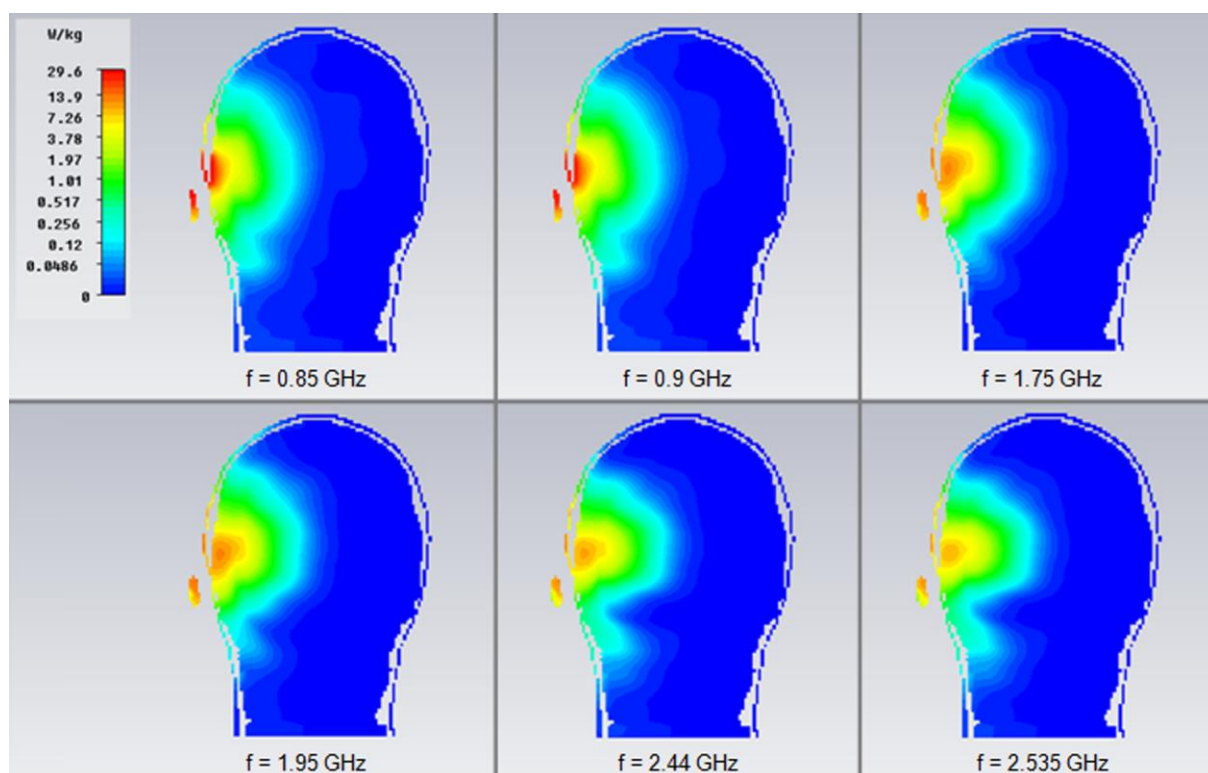


Figure E.10 – Front cut plane for maximum SAR reading on antenna designed for 2.6 GHz

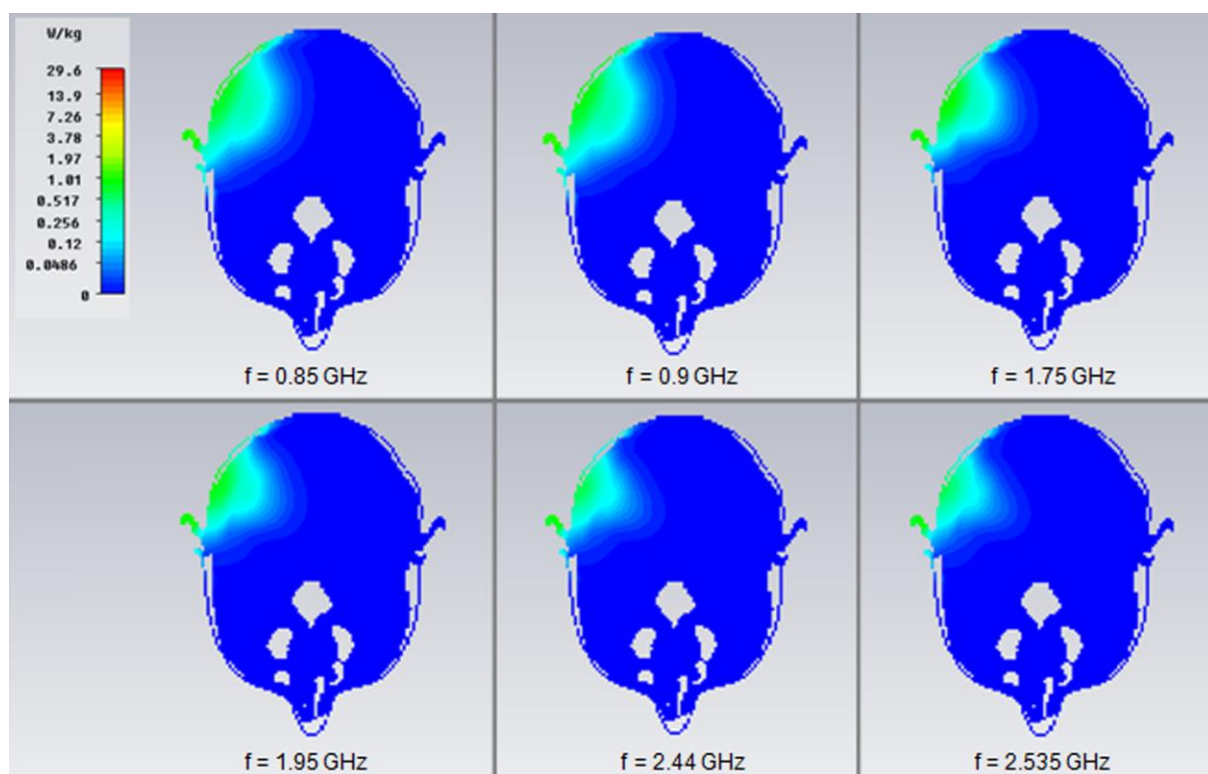


Figure E.11 – Top cut plane for maximum allowed power on antenna designed for 2.6.

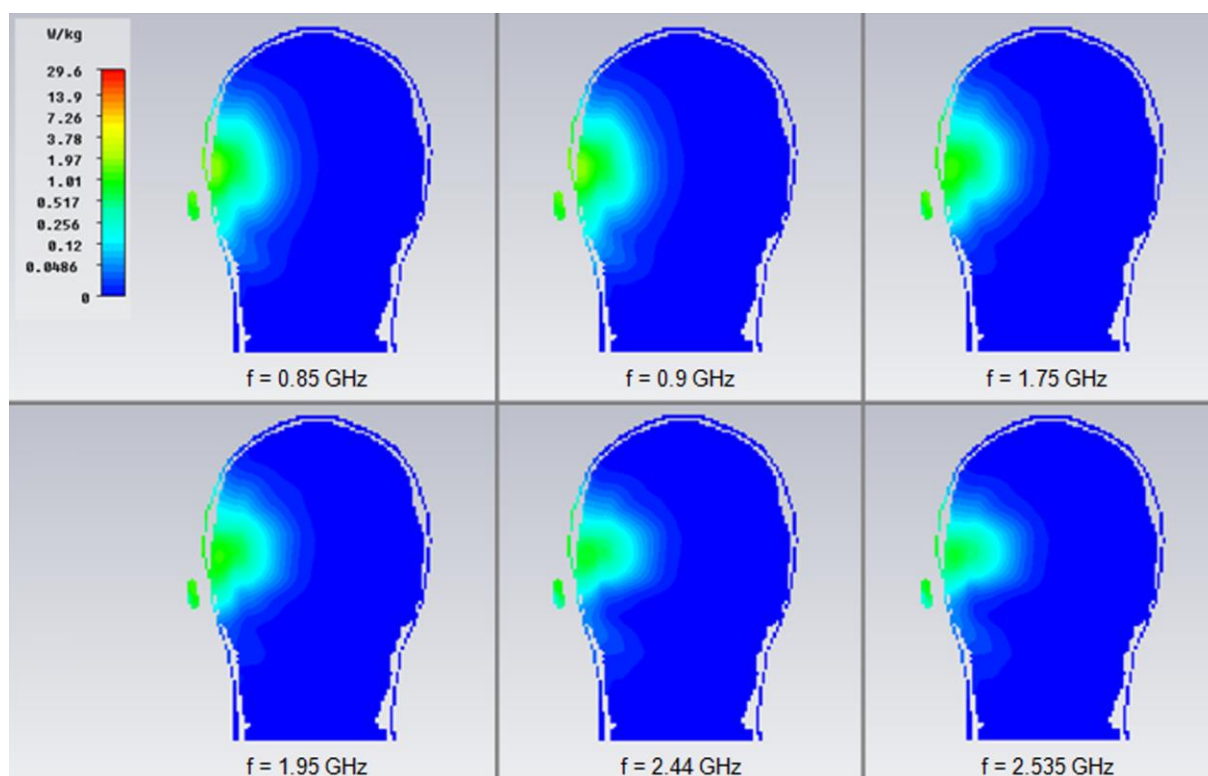


Figure E.12 – Front cut plane for maximum allowed power on antenna designed for 2.6.

Table E.1 – Linear values correspondent to amplitudes of main lobes, on radiation pattern charts from Chapter 4.

Frequency [GHz]		0.8	0.9	1.8	2.1	2.4	2.6
Original antenna [V/m]	Top	4.75	5.44	26.1	33.8	45.3	45.8
	Front	4.83	5.49	27.1	34.5	50.3	52
Antenna for 1.8 GHz [V/m]	Top	6.23	7.27	29.3	31.4	36.1	36.9
	Front	6.63	7.65	32.1	35.1	41.7	42.3
Antenna for 2.6 GHz [V/m]	Top	4.21	4.89	2.1	28.9	44.2	45
	Front	4.58	5.21	24.5	31.9	51.3	53.1

Table E.2 – RF output power measurement in dBm of *Glass's* SAR report (extracted from [FCC14c]).

Technology	Mode	Channel #	Freq. [MHz]	Maximum Power [dBm]	Avg. Power [dBm]
Wi-Fi	82.11b	1	2412	15.0	15.0
		6	2437	15.0	15.0
		11	2462	15.0	15.0
	802.11g	1	2412	15.0	14.7
		6	2437	15.0	15.0
		11	2462	15.0	15.0
LEBT	GFSK	0	2402	7.1	5.1
		39	2441	7.7	5.9
		78	2480	7.6	5.8
	8PSK	0	2402	5.0	3.2
		39	2441	5.7	3.7
		78	2480	5.7	3.7

References

- [3GPP09] 3GPP, *Universal Mobile Telecommunications System (UMTS); User Equipment (UE) radio transmission and reception (FDD) (release 6)*, TS 25.101, Ver. 6.19.0, Mar. 2009.
- [3GPP11] 3GPP, *LTE; Evolved Universal Terrestrial Radio Access (E-UTRA); User Equipment (UE) radio transmission and reception (release 10)*, TS 36.101, Ver. 10.3.0, June 2011.
- [3GPP13a] 3GPP, *LTE; Evolved Universal Terrestrial Radio Access (E-UTRA); Physical layer procedures (Release 11)*, TS 36.213, Ver. 11.3.0, July 2013 (<http://www.3gpp.org>).
- [3GPP13b] 3GPP, Technical Specification Group Radio Access Network; Evolved Universal Terrestrial Radio Access (E-UTRA), *Base Station (BS) radio transmission and reception (Release 11)*, Report TS 36.104, V11.4.0, Mar. 2013 (<http://www.3gpp.org/ftp/Specs/html-info/36104.htm>).
- [3GPP14] 3GPP, *Digital cellular telecommunications system (Phase 2+); Radio transmission and reception (Release 10)*, TS 45.005, Ver. 10.0.0, Apr. 2014
- [Ag11] Johnson Ihieh Agbinya, *Principles of Inductive Near Field Communications for Internet of Things*, River Publishers, Aalborg, Denmark, 2011.
- [Agil09] Agilent Technologies, *Agilent 3GPP Long Term Evolution: System Overview, Product Development, and Test Challenges*, Application Note, USA, 2009 (<http://cp.literature.agilent.com/litweb/pdf/5989-8139EN.pdf>).
- [ANAC14] <http://www.anacom.pt/render.jsp?contentId=1105917>, May 2014.
- [Ba05] Constantine A. Balanis, *Antenna theory analysis and design (3rd edition)*, John Wiley and Sons, Hoboken, New Jersey, United States of America, 2005
- [Ba13] Bobby Bayani, *SAR Evaluation report for Glass*, Report Number: 13U14955-5A, UL CCS, Fremont, California, United States of America, Apr 2013 (<https://apps.fcc.gov/eas/GetApplicationAttachment.html?id=1910648>).
- [Bern] Bernhardsson, B., *Power Control in CDMA Background*, Dept. of Automatic Control, Lund Institute of Technology.
- [Ca10] Elisabeth Cardis, *Brain tumour risk in relation to mobile telephone use: results of the INTERPHONE international case-control study*, International Journal of Epidemiology, Oxford University, Oxford, United Kingdom, May 2010 (<http://ije.oxfordjournals.org/content/early/2010/05/17/ije.dyq079.full.pdf+html>).
- [CAD14] <http://grabcad.com/library/google-glass-2>
- [CENE13] CENELEC, "Basic standard for the calculation and measurement of electromagnetic field strength and SAR related to human exposure from radio base stations and fixed

- terminal stations for wireless telecommunication systems (110 MHz – 40 GHz)”, Ref. No. EN 50383:2010/AC:2013, Central Secretariat, Brussels, Belgium, June 2013.
- [ChCa01] Charles Capps, “Near field or far field?”, *EDN magazine*, Aug. 2001, pp. 95-102.
- [Corr13] Correia, L.M., *Mobile Communications Systems – Lecture Notes*, Instituto Superior Técnico, Lisbon, Portugal, Feb. 2013.
- [COST00] COST 244 bis, *Biomedical Effects of Electromagnetic Fields*, Final report, COST 244 bis, Nov. 2000.
- [CST14] CST – *Computer Simulation Technology*, CST, 2012 (<http://www.cst.com>).
- [Eric11] Ericsson, *LTE: an introduction*, Lite Paper, Stockholm, Sweden, 2011 (http://www.ericsson.com/res/docs/2011/lte_an_introduction.pdf).
- [FCC13] *First report and order further notice of proposed rule making and notice of inquiry*, FCC 13-39, Federal Communications Commission, Washington D.C., United States of America, Mar 2013.
- [FCC14a] Glass’s External photos report
(https://apps.fcc.gov/oetcf/eas/reports/ViewExhibitReport.cfm?mode=Exhibits&RequestTimeout=500&calledFromFrame=N&application_id=287362&fcc_id=A4R-X1).
- [FCC14b] Glass’s Internal photos report
(https://apps.fcc.gov/oetcf/eas/reports/ViewExhibitReport.cfm?mode=Exhibits&RequestTimeout=500&calledFromFrame=N&application_id=287362&fcc_id=A4R-X1).
- [FCC14c] Glass’s SAR report
(https://apps.fcc.gov/oetcf/eas/reports/ViewExhibitReport.cfm?mode=Exhibits&RequestTimeout=500&calledFromFrame=N&application_id=287362&fcc_id=A4R-X1)
- [FI08] Fleisch, D., *A Student’s Guide to Maxwell’s Equations*, Cambridge University Press, Cambridge, United Kingdom.
- [FOPH14] <http://www.bag.admin.ch/themen/strahlung/00053/00673/04265/index.html?lang=en>
- [Ga96] Gabriel, C., *Compilation of Dielectric Properties of Body Tissues at RF and Microwave Frequencies*, Brooks Air Force Technical Report, AL/OE-TR-1996-0037, San Antonio, TX, USA, 1996.
- [GaPH05] Peyman, A., S. Holden, and C. Gabriel, *Measurement of the dielectric properties of biological tissues in vivo at microwave frequencies*, Mobile Telecommunications and Health Research Programme, RUM 3, Final Report, 2005.
- [GePaSo10] Gemio, J., Parrón, J. and Soler, J., “Human Body Effects on Implantable Antennas for ISM Band Applications: Models Comparison and Propagation Losses Study”, *Progress In Electromagnetics Research*, Vol. 110, pp. 437-452, 2010
- [GuGu03] Gunnarsson, F. and Gustafsson, F., *Control theory aspects of power control in UMTS, Control Engineering Practice*, Volume 11, Issue 10, Pages 1113-1125, October 2003.
- [Ha07] Lennart Hardell, *Long-term use of cellular and cordless phones and the risk of brain tumours*, Department of Oncology, University Hospital, Örebro, Sweden, Aug 2007.

- [HaCA09] Lennart Hardell, Michael Carlberg, "Mobile phones, cordless phones and the risk for brain tumours", *International Journal of Oncology*, Volume 35, Issue 1, July 2009, pp. 5-17.
- [HaCaHa11] Hardell, L., Carlberg, M., Hansson Mild, K., *Pooled analysis of case-control studies on malignant brain tumours and the use of mobile and cordless phones including living and deceased subjects.*, *International Journal of Oncology*,
- [HoTo06] Holma, H., Toskala, A., *HSDPA/HSUPA for UMTS*, John Wiley, Chichester, United Kingdom, 2006.
- [HoTo07] Holma, H. and Toskala, A., *WCDMA for UMTS - HSPA Evolution and LTE*, John Wiley, Chichester, United Kingdom, 2007.
- [HoTo11] Holma, H. and Toskala, A., *LTE for UMTS: Evolution to LTE Advanced (2nd Edition)*, John Wiley & Sons, Chichester, UK, Mar. 2011.
- [Hu11] Jean Huss, *The potential dangers of electromagnetic fields and their effect on the environment*, Parliamentary Assembly, Committee on the Environment, Agriculture and Local and Regional Affairs, Doc. 12608, Council of Europe, Brussels, Belgium, 06 May 2011
- [ICNI09] ICNIRP, "Statement on the "Guidelines for Limiting Exposure to Time-Varying Electric, Magnetic, and Electromagnetic Fields (up to 300 GHz)""", *Health Physics*, Vol. 97, Supplement 3, pp. 257-258, 2009 (<http://www.icnirp.de>).
- [ICNI11] ICNIRP, "Review of the Mobile Phones, Brain Tumours and the Interphone Study: Where Are We Now?", *Environmental Health Perspectives*, Vol. 119, Supplement 11, pp. 1534-1538, July 2011 (<http://www.icnirp.de>).
- [ICNI98] ICNIRP, "Guidelines for Limiting Exposure to Time-Varying Electric, Magnetic, and Electromagnetic Fields (up to 300 GHz)", *Health Physics Society*, Vol. 74, No. 4, pp. 494-522, 1998 (<http://www.icnirp.de>).
- [ITIS14] <http://www.itis.ethz.ch/itis-for-health/tissue-properties/database/dielectric-properties/>, May 2014.
- [Ito07] K. Ito., "Numerical and Experimental Human Body In Antennas and Propagation for Body-Centric Wireless Communications", *IET Seminar*, London, United Kingdom, 24-26 April 2007.
- [KhAzIs14] Khan, N.I., Azim, A. and Islam, S., "Radiation Characteristics of a Quarter-Wave Monopole Antenna above Virtual Ground", *Journal of Clean Energy Technologies*, Vol. 2, No. 4, Oct. 2014
- [Kib13] Kibona, L., "Analysis of the Effects Rectangular Ground Plane on Radiation Pattern of the Monopole Antenna", *International Journal of Scientific and Research Publications*, Vol. 3, Issue 11, Nov. 2013
- [KSMVK13] Kavindra Kumar Kesari, Mohd Haris Siddiqui, Ramovatar Meena, Shivendra Kumar, "Cell phone radiation exposure on brain and associated biological systems", *Indian Journal of Experimental Biology*, Vol.51, Mar 2013, pp. 187-200

- [KTKH09] Khurana, V., Teo, C., Kundi, M., Hardell, L., *Cell phones and brain tumors: a review including the long-term epidemiologic data.*, PubMed, Canberra, Australia, Mar 2009
- [LaBuPo98] Lai, E., Burks, C., Posakony, J., *The K box, a conserved 3' UTR sequence motif, negatively regulates accumulation of enhancer of split complex transcripts.*, Department of Biology and Centre for Molecular Genetics, University of California San Diego, La Jolla, United States of America, Sep 1998.
- [Lo10] Lopes, C., *Characterisation of the Radio Channel in On-Body Communications*, M.Sc. Thesis, Instituto Superior Técnico, Lisboa, Portugal, 2010.
- [Ma13] Mackowiak, M., *Modelling MIMO Systems in Body Area Networks in Outdoors*, Ph. D. Thesis, Instituto Superior Técnico, Lisboa, Portugal, 2013
- [Mai11] Maícas, J.P., *Recent Developments in Mobile Communications - A Multidisciplinary Approach*, InTech, Rijeka, Croatia, 2011
- [Mani09] Mario Maniewicz, "Information Society Statistical Profiles 2009", *Regional Preparatory Meeting for the ITU World Telecommunication Development Conference 2010 (WTDC-10)*, Andorra, Dec 2009.
- [Moli11] Molisch, A.F., *Wireless Communications*, John Wiley, Chichester, United Kingdom, 2011.
- [OICa02] Oliveira, C.S., Carpinteiro, G., *Electromagnetic radiation exposure of GSM and UMTS Base Station Antennas* (in Portuguese), Final Graduation Project, Instituto Superior Técnico, Technical University of Lisbon, Lisbon, Portugal, 2002.
- [RE14] http://www.radio-electronics.com/info/cellular telecomms/gsm_technical/power-control-classes-amplifier.php.
- [RWY95] Y. Rahmat-Samii, L. I. Williams, and R. G. Yoccarino, "The UCLA Bi-polar Planar-Near-Field Antenna Measurement and Diagnostics Range", *IEEE Antennas & Propagation Magazine*, Vol. 37, No. 6, December 1995
- [TGSW10] György Thuróczy, Peter Gajsek, Theodoros Samaras, Joe Wiart, *Report on the level of exposure (frequency, patterns and modulation) in the European Union*, Deliverable Report D4 of EHFRAN project, European Health Risk Assessment Network on Electromagnetic Fields Exposure, Milan, Italy, Aug 2010.
- [Twit14] <https://twitter.com/rblank9>
- [Vile12] Vilela, J., "Small Cells and Heterogeneous Networks", *19th of June 2012 – IEEE ComSoc Portugal Chapter and Instituto Superior Técnico Seminar*, Instituto Superior Técnico, Technical University of Lisbon, Lisbon, Portugal, June 2012 (<http://chapters.comsoc.org/Portugal/>).
- [Wei03] Weiner, M.M., *Monopole Antennas*, Marcel Dekker Inc., New York, USA, 2003
- [WHO02] World Health Organisation (WHO), *Establishing a dialogue on risks from electromagnetic fields*, Radiation and Environmental Health, Department of Protection of the Human Environment, WHO, Geneva, Switzerland 2002.

[WHO11] World Health Organisation (WHO), “IARC classifies radiofrequency electromagnetic fields as possibly carcinogenic to humans”, in Press Release n° 208, Lyon, France, May 2011.